Università degli Studi di Ferrara

DOTTORATO DI RICERCA IN
FISICA

CICLO XXI

COORDINATORE Prof. Filippo Frontera

Passive Millimeter Wave Imaging Camera *ViKy* as Technology Transfer of *Planck* – LFI

Settore Scientifico Disciplinare FIS/01

Dottorando
Dott. Juri Zuccarelli

Tutore
Prof. Nazzareno Mandolesi

Co Tutore
Dott. Carlo Burigana

Anni 2006/2008

Contents

Introduction **1**

1 Passive radiometry **5**
- 1.1 Overview of Millimeter-Wave Radiometry 6
  - 1.1.1 Atmospheric Propagation 7
  - 1.1.2 Emissivity and Brightness Temperature 8
  - 1.1.3 Imaging Principles 11
- 1.2 The PMMW Camera 14
  - 1.2.1 PMMW Imaging 14
  - 1.2.2 PMMW Camera 15
  - 1.2.3 Applications 17
  - 1.2.4 Imaging of People and Concealed Weapons Detection . 17
  - 1.2.5 Reconnaissance and Surveillance 18
  - 1.2.6 Low-Visibility Navigation and Situation Awareness . . 20
  - 1.2.7 Perimeter Surveillance 20
  - 1.2.8 Other applications 20
- 1.3 Conclusion 21

2 Ka-Band Imaging Camera **23**
- 2.1 Introduction 23
- 2.2 The *ViKy* project 23
- 2.3 Antenna System 25
  - 2.3.1 Antenna specifications 25
- 2.4 Antenna Design and Technology 25
- 2.5 Radiometer specifications 28

3 Microstrip Antennas **29**
- 3.1 Introduction 29
  - 3.1.1 Basic Characteristics 29
  - 3.1.2 Feeding Methods 30

3.2 Methods of analysis 33
3.2.1 Transmission Line Model for Rectangular Patch 33
3.2.2 Cavity Model 44
3.2.3 Full Wave Model 55

4 Reflectarray Antenna 57
4.1 Review of development history 60
4.2 Analysis and design procedures 62
4.2.1 Element characterization 63
4.2.2 Required Phase Delay 63
4.2.3 Pattern Calculation 64
4.2.4 Reflectarray Geometry Design 65
4.3 Bandwidth 66
4.4 Summary 68

5 The Total Power Radiometer 71
5.1 Electromagnetic radiation 72
5.2 Definition of radiometric quantities 74
5.3 Blackbody radiation and emissivity 75
5.3.1 Lambert's Law and Lambertian Radiators 78
5.3.2 Radiometric Brightness and Antenna Temperatures . . 78
5.3.3 Atmospheric Loss and Scattering 82
5.3.4 Definition of Co- and Cross- polarization 83

6 The *ViKy* Project 85
6.1 The *ViKy's* Horn 85
6.1.1 Requirements 85
6.1.2 Description of the design process 86
6.1.3 Results of *FHAPP* simulations 86
6.1.4 CST Microwave Studio Simulations 90
6.1.5 Conclusions 94
6.2 The *ViKy's* Reflectarray 95
6.2.1 Antenna description 95
6.2.2 Analytical results 106
6.2.3 Reflectarray manufacturing 107
6.3 The *ViKy's* Radiometer 108
6.3.1 Noise Figure 110
6.3.2 Y_{factor} 111

6.3.3 T_{NOISE} . . . 112
6.3.4 The Detector . . . 112
6.4 The *ViKy's* Motion Control . . . 112
6.5 Conclusion . . . 113

7 Measurements **115**
7.1 Electromagnetic horn measurements . . . 115
7.1.1 Analysis and results . . . 116
7.2 Electromagnetic reflectarray measurements . . . 118
7.2.1 Analytical VS measurements results . . . 118
7.3 Low Noise Amplifier measurements . . . 122
7.3.1 Description of the setup measurements . . . 122
7.3.2 Analysis and results . . . 124
7.4 Diode Detector measurements . . . 126
7.4.1 Detection sensitivity . . . 126
7.4.2 Detection linearity . . . 126
7.5 Radiometric temperature measurements . . . 127
7.5.1 Determination of the temperature error . . . 128
7.6 Conclusions . . . 130

8 Conclusions **131**
8.1 The *ViKy* project . . . 132
8.1.1 Antenna System . . . 133
8.1.2 Radiometer System . . . 136
8.1.3 Image Post Processing . . . 137
8.2 Applications . . . 138

A Technology transfer projects - 2004 ÷ 2009 **139**
A.1 SPINNER-The WIC Project . . . 139
A.2 UIT-Innovation Technology Office . . . 139
A.2.1 UIT Funded Projects for the IASF team . . . 140
A.3 PRISMA . . . 141
A.3.1 PRISMA Funded Projects for the IASF team . . . 142
A.4 ASTRO SFERA . . . 142
A.4.1 ASTRO SFERA Funded Projects for the IASF team . . . 142
A.5 ASI . . . 143

Bibliography **145**

List of Figures

1.1 Atmospheric attenuation 6
1.2 Spectral radiance 8
1.3 Radiometric effects 11
1.4 PMMW runway 12
1.5 94-GHz PMMW 13
1.6 FPA PMMW camera 16
1.7 Outdoors concealed weapons images 18
1.8 Indoors concealed weapons images 19
1.9 PMMW image through clouds 19
1.10 PMMW images of the Queen Mary 20

2.1 Reflectarray concept 26
2.2 Reflection phase versus varactor bias 27

3.1 Microstrip antenna 30
3.2 Shapes of microstrip 31
3.3 Typical feeds 32
3.4 Equivalent circuits 33
3.5 Microstrip line and its electric field lines 35
3.6 Effective permittivity 36
3.7 Physical and effective lengths 36
3.8 Rectangular microstrip patch and its equivalent circuit. 39
3.9 Slot conductance as a function of slot width 41
3.10 Recessed microstrip-line feed 43
3.11 Charge distribution on microstrip patch 46
3.12 Patch geometry 49
3.13 Field configurations – modes 50
3.14 Equivalent current densities 52
3.15 Radiating slots 54
3.16 Typical E- and H-plane patterns of each microstrip patch slot . 54

3.17 Current densities on non radiating slots 54
3.18 Unit cell in CST-MWS 56
3.19 TEM waveguide in HFSS 56

4.1 Reflectarray antenna 58
4.2 Various reflectarray elements 59
4.3 Microstrip reflectarray 61
4.4 Curve of phase versus L size 64
4.5 Spillover and illumination efficiency 66
4.6 $\cos^q$ feed pattern and the aperture efficiency 66
4.7 Phase delay of reflectarray 67

5.1 Passive and active radiometry 72
5.2 Planck's law for blackbody radiation 77
5.3 Rayleigh-Jeans approximation for blackbody radiation 77
5.4 Spectral irradiance 79
5.5 Solid angle 79
5.6 Co- e cross- polarization 83
5.7 Co- e cross- polar components 83

6.1 Mechanical drawing of the corrugated horn antenna 87
6.2 Return Loss response obtained through *FHAPP* simulation . . 87
6.3 *FHAPP* simulations at 32.5 GHz princ. plane 88
6.4 *FHAPP* simulations at 32.5 GHz $\Phi = 45°$ plane 88
6.5 *FHAPP* simulations at 35 GHz princ. plane 88
6.6 *FHAPP* simulations at 35 GHz $\Phi = 45°$ plane 89
6.7 *FHAPP* simulations at 37.5 GHz princ. plane 89
6.8 *FHAPP* simulations at 37.5 GHz $\Phi = 45°$ plane 89
6.9 Corrugation and the error analysis 90
6.10 Return Loss of the horn with the imposed error 91
6.11 *FHAPP* simulations at 32.5 GHz princ. plane (Step 6) 91
6.12 *FHAPP* simulations at 35 GHz princ. plane (Step 6) 91
6.13 *FHAPP* simulations at 37.5 GHz princ. plane (Step 6) 92
6.14 CST-MWS simulation for the corrugated horn 92
6.15 Return Loss response: CST-MWS vs. FHAPP 93
6.16 Horn Simulations at $f = 32.5$ GHz: CST-MWS vs. FHAPP . . 93
6.17 Horn Simulations at $f = 35$ GHz: CST-MWS vs. FHAPP . . . 94
6.18 Horn Simulations at $f = 37.5$ GHz: CST-MWS vs. FHAPP . . 94

6.19 Array dimensions 96
6.20 Single layer microstrip patch geometry 97
6.21 Offset configuration of the *ViKy* antenna system 98
6.22 Simulation geometry 100
6.23 Phase change with CST simulations 100
6.24 Phase change commercial sw 100
6.25 Feed reference system 101
6.26 Distribution of the distance and of the $\theta_{i,j}$ angle 102
6.27 Distribution of the $\Psi_{i,j}$ contribution 103
6.28 Total phase contribution (Offset case) 103
6.29 Grasp ray tracing (Offset config.) 104
6.30 Grasp ray tracing (Onset config.) 104
6.31 Amplitude and phase distribution (Offset) 105
6.32 Amplitude and phase distribution (Onset) 105
6.33 Distribution of patch dimensions (Offset and Onset cases) . . . 106
6.34 Radiometric diagram 108
6.35 Radiometer's picture 109
6.36 *ViKy's* structure 113
6.37 *ViKy's* structure (Front view). 113

7.1 Horn's measures and simulations at f=32.5 GHz 116
7.2 Horn's measures and simulations at f=35.0 GHz 116
7.3 Horn's measures and simulations at f=37.5 GHz 117
7.4 RL measures and simulations 117
7.5 Setup for the electromagnetic measures 119
7.6 On-set patterns 120
7.7 On-set patterns (with Rohacell) 120
7.8 E-plane on-set patterns (with in/out Rohacell) 120
7.9 H-plane on-set patterns (with in/out Rohacell) 121
7.10 Measures VS simulation (E-plane On-set) 121
7.11 Measures VS simulation (H-plane On-set) 121
7.12 Measures VS simulation (H-plane Off-set) 122
7.13 Setup for the Attenuator measurements 123
7.14 Setup for the amplifier measurements 123
7.15 Radiometric chain 123
7.16 Gain and amplitude curves for the first stage LNA 124
7.17 Gain and amplitude curves for the second stage LNA 124

7.18 Gain and amplitude curves for the LNAs 125
7.19 Diode Sensitivity 127
7.20 Diode linearity 128
7.21 Radiometric temperature measurements 128

8.1 *ViKy* antenna system in off set configuration 134
8.2 Schematic diagram of the patch's dimensions determination . 135
8.3 Radiometer 136
8.4 Electronic devices 137
8.5 Example of a customer interface software 138

List of Tables

1.1 Object Emissivity 10

2.1 Antenna specifications 26
2.2 Radiometer specifications 28

6.1 RF specifications of the feed-horn 86
6.2 Error analysis in the feed-horn design 90
6.3 Reflectarray specifications 95
6.4 Substrate characteristics 96

7.1 Horn analysis 117
7.2 LNA Gains 125
7.3 LNA properties 126
7.4 Y_{FACTOR} and T_{NOISE} measurements 126
7.5 Radiometer analysis 129
7.6 Radiometer analysis - The temperature is controlled. 129
7.7 Determination of the temperature error 129
7.8 Determination of the temperature error at $T \simeq T_{Nitrogen}$. 129

Introduction

The passive Video camera for Imaging in Ka-band, named *ViKy* project, was born in 2004 as one of the possible spin-offs based on the technology transfer of ESA PLANCK satellite program. The first year of the project, initially named WIC (W-band Imaging Camera), was financed by the SPINNER consortium (composed of Fondazione Alma Mater, ASTER Scienza Tecnologia Impresa, Sviluppo Italia) where SPINNER is the acronym of "Servizi per la Promozione dell'INNovazione E della Ricerca" (Services for the Promotion of the INNovation and Research). Since 2005 the project has been financed by INAF (Istituto Nazionale di AstroFisica).

***ViKy* project**

The WIC project was initially born thanks to an idea of Professor Nazzareno Mandolesi and Ing. Enrico Pagana. In a very short time they set up two teams of people, the first one responsible for the antenna design, the second for the radiometer chain design. At the end of the first year both teams have been grouped into the IASF team composed of Ing. Valerio Martorelli, Ing. Adriano De Rosa, Dr. Carlo Burigana, Dr. Luca Stringhetti, Dr. Luca Valenziano, Dr. Fabrizio Villa and me. In 2005 the IASF team decided to scale the project from W-band (92 GHz) to Ka-band (35 GHz) to allow the use of cheaper 35 GHz commercial components and then to reduce the costs of the prototyping phase. In this way *ViKy* system was born and from then on I dedicated my researches in the design on the whole project taking into account both the theoretical and the technical aspects.

This introduction presents an overview of the *ViKy* project, introduces the concept of millimeter passive systems and describes the *ViKy* subsystems. Finally the framework of the thesis is presented.

The *ViKy* subsystems

The aim of the *ViKy* project is to develop a passive mm-wave imaging camera. *ViKy* is a passive system because it does not need to illuminate the target (or an object in a scene) with an external radiation source as it happens for example in a radar system. A key part of *ViKy* project is the design of a compact and low cost antenna suitable for development of a commercial product. *ViKy* system scans the scene mechanically and recreates the image in false colors. The adopted solution for the prototyping system is a mechanical beam scanning reflectarray antenna but in the future this scanning system should be replaced with an electronic beam scanning without use of mechanical movements.

At system level the prototype can be subdivided in five units: the antenna system able to scan the scene quickly; the antenna electronic control that allows to carry out the scanning of the image; the radiometer that amplifies and detects the electromagnetic signal coming from the antenna; the Data Acquisition Electronics; the software for the image processing and the final interface.

The framework of the thesis

The know-how acquired during these three years has been collected in my PhD thesis that has been split in eight different chapters; in the first five chapters I have discussed the *ViKy* subsystems from a theoretical point of view whereas in the remaining two chapters I presented the design of the *ViKy* project, the description and the measurements of the prototype. The final chapter has been dedicated to summarize the whole study and to present the conclusions that have been also partially pointed out in every chapter.

The first chapter introduces the concept of passive radiometry providing an overview of the millimeter wave radiometry and of the passive millimeter wave camera. The main physical principles and applications are described.

The second chapter introduces the concept of Ka-band imaging camera describing a first important overview of the *ViKy* project, illustrates the antenna design, and presents the radiometer specifications.

The third chapter describes the microstrip antennas focusing on the aspects related to the methods of analysis.

The fourth chapter describes the reflectarray antenna and explains the main differences between the principal design procedures.

The fifth chapter introduces the total power radiometry theory, defines the principal radiometric quantities, and focuses the question of the physical aspects of radiation and emissivity materials.

The sixth chapter discusses the *ViKy* project in detail highlighting the requirements, the design procedures and the manufacturing aspects of all the *ViKy* subsystems.

The seventh chapter describes the electromagnetic measurements and the comparisons between them and the simulations.

The last chapter summarizes the *ViKy* project coming through the principal and crucial aspects of the design and finally presents main goals that have been achieved.

An appendix has been added to illustrate all the technology transfer projects that have been carried out by the IASF team since 2004 thanks to the contribution of the SPINNER Consortium and of the Innovation Technology Office which provided the possibility to develop the *ViKy* project.

Chapter 1

Passive radiometry

Passive millimeter-wave (PMMW) imaging is a method of forming images through the passive detection of naturally occurring millimeter-wave radiation from a scene. Although such imaging has been performed for decades (or more, if one includes microwave radiometric imaging), new sensor technology in the millimeter-wave range has enabled the generation of PMMW imaging at video level and has renewed interest in this area. This interest is, in part, driven by the ability to form images by day or night; in clear weather or in low-visibility conditions, such as haze, fog, clouds, smoke, or sandstorms; and even through clothing. This ability permits to see under conditions of low visibility, what otherwise visible or infrared (IR) sensors can do. In the commercial field, fog-bound airports could be eliminated as a cause for flight delays. For security concerns, imaging of concealed weapons could be accomplished in a nonintrusive manner with PMMW imaging.

Like IR and visible sensors, a camera based on PMMW sensors generates easily interpretable images. PMMW cameras are passive systems so they do not need to ionize the materials to receive the backscattered radiation; no discernible radiation is emitted, unlike radar and lidar. For this reason they work in a fully covert manner. However, like radar, PMMW sensors provide penetrability in a variety of low-visibility conditions (moderate/heavy rainfall is an exception). In addition, the underlying phenomenology that governs the formation of PMMW images leads to two important features. First, the signature of metallic objects is very different from natural and other backgrounds. Second, the clutter variability is much less in PMMW images than in other sensor images. Both characteristics lead to much easier automated target detection with fewer false alarms. The wide range of civilian missions that would benefit from an imaging capability through

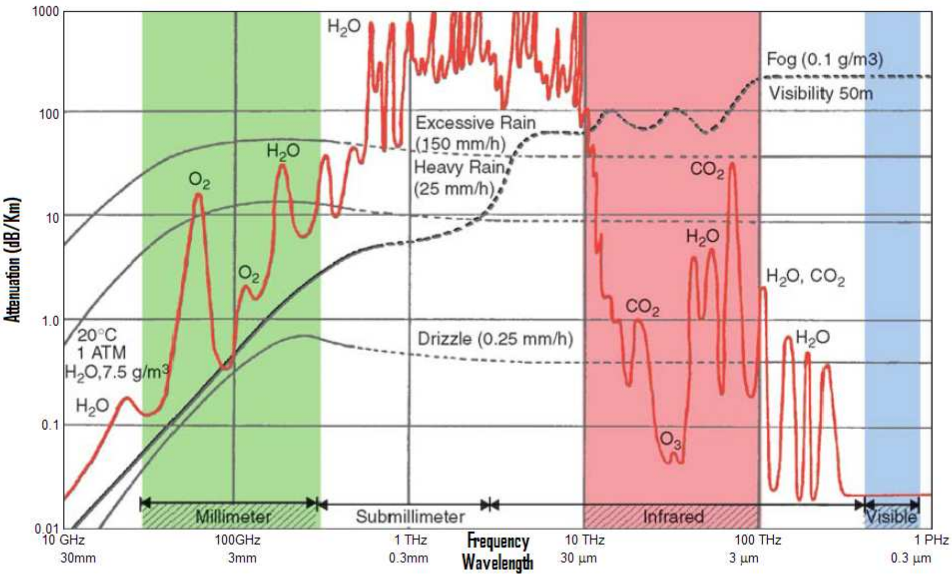

Figure 1.1: The attenuation of millimeter waves by atmospheric gases, rain, and fog.

low-visibility conditions, coupled with its inherent covertness, includes commercial aircraft landing aid in fog, airport operations in fog, harbor surveillance, highway traffic monitoring in fog, and concealed weapons detection in airports and other locations. Similarly, a number of military imaging missions would benefit, such as surveillance, precision targeting, navigation, aircraft landing, refueling in clouds, search and rescue, metal detection in a cluttered environment, and harbor navigation/surveillance in fog.

This section introduces the concept of PMMW imaging, describes the phenomenology that defines its performance, explains the technology advances that have made these systems a reality, and presents some of the missions in which these sensors can be used.

1.1 Overview of Millimeter-Wave Radiometry

The range of the electromagnetic spectrum where it is possible for humans to see is the part where is the peak of the Sun's radiance (at about 6000 K): the visible range. In that range, the human eye responds to different wavelengths of scattered light by seeing different colors.

In the absence of sunlight, however, the natural emissions from Earth objects (at about 300 K) are concentrated in the IR range. Advances in IR-sensor technology in the last 30 years have produced detectors sensitive in that frequency range, making night vision possible. The exploitation of the millimeter-wave range (defined to lie between 30 and 300 GHz, with corresponding wavelengths between 10 and 1 mm) follows as a natural progression in the quest to expand our vision. The great advantage of millimeter-wave radiation is that it can be used not only in day and night conditions, but also in fog and other poor visibility conditions that normally limit the "seeing" ability of both visual and IR sensors. Many good references exist to introduce imaging in this range, and a brief overview will be presented here [73] - [44].

1.1.1 Atmospheric Propagation

The usefulness of millimeter waves lies in the peculiarities of atmospheric attenuation phenomenologies over the prescribed frequency range. Figure 1.1 shows the attenuation of electromagnetic signals in decibels per kilometer of the propagation path length from the microwave through the visible range [61]. This spans the frequency range from 10 GHz to 1000 THz, with corresponding free-space wavelengths from 3 cm to 0.3 m. Propagation of electromagnetic waves over this frequency range is subject to continuous and resonant absorption by various atmospheric constituents, including water in both vapor and droplet form, oxygen, nitrogen, carbonic anhydride, ozone, etc. In clear, dry weather, IR and visible radiation propagate with little attenuation; however, atmospheric water content in the form of fog, clouds, and rain causes significant absorption and scattering. In the far IR and submillimeter-wave range, significant attenuation occurs from water vapor. Conversely, in the millimeter-wave range, there are propagation windows at 35, 94, 140, and 220 GHz, where the attenuation is relatively modest in both clear air and fog. Even taking into account the much higher blackbody radiation at IR and visible frequencies, millimeter waves give the strongest signals in fog when propagated over distances of useful interest (see Figure 1.2). In fact, millimeter-wave radiation is attenuated millions of times less in clouds, fog, smoke, snow, and sandstorms than visual or IR radiation. This is the crucial advantage of PMMW imagery. Moreover, millimeter-wave imagery is minimally affected by Sun or artificial illumination. Therefore, it operates equivalently in clear or low-visibility conditions during the day or night. It is this ability that makes millimeter waves the best candidate for imaging in most conditions of low visibility.

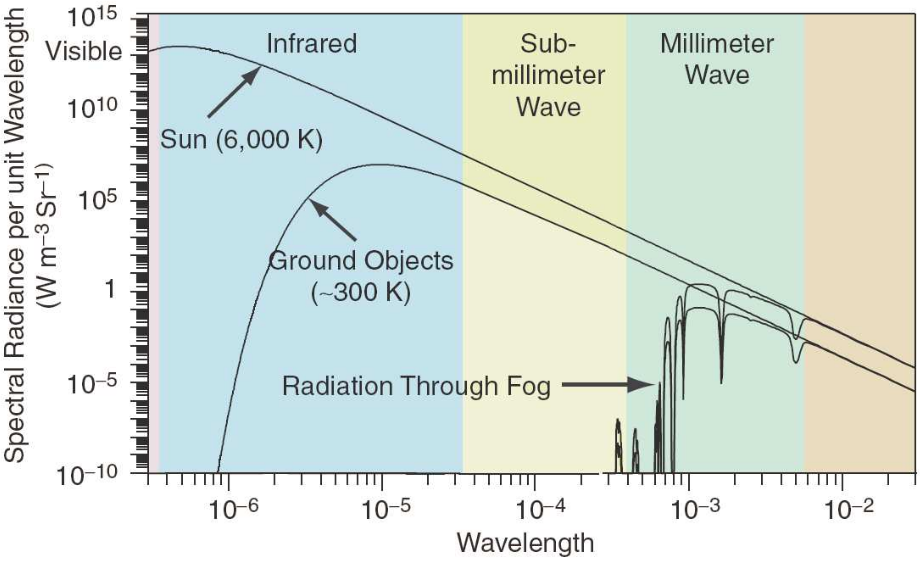

Figure 1.2: The effect of fog on the blackbody radiation intensity of the Sun (6000 K) and a ground object ($\sim 300K$) as a function of wavelength. Curves are shown for both objects without fog and with the effect of 1 Km of fog.

1.1.2 Emissivity and Brightness Temperature

Every object generates electromagnetic emissions at all wavelengths with intensity proportional to the product of its physical temperature and its emissivity in accordance with Planck's radiation law. In other words the objects reflect and emit radiation in the millimeter wave range, just as they do in the IR and visible ranges. The degree to which an object reflects or emits is characterized by the emissivity (ϵ) of the object. A perfect radiator (absorber) has $\epsilon = 1$ and is known as a blackbody. A perfect reflector (nonabsorber) has $\epsilon = 0$. Objects also reflect the radiation emanating from the environment to a degree of reflectivity which is the complement of their emissivity; the sum of the emissivity and the reflectivity is 1. Thus, an object that reflects 90 percent of the radiation striking it will have an emissivity of 10 percent. These values are generally a function of wavelength, so what might be reflecting at long wavelengths in the radio-frequency region may appear to be emissive in the infrared region. An example of this would be a metal mirror with a coating of dull black paint. An infrared sensor would receive an emissivity close to 1 and would be sensitive to the temperature of the coating, while an RF sensor would see the reflecting surface as the mirror, since the coating is readily penetrated by the long wavelengths.

The human body has an emissivity of about 65 percent at 100 GHz, increasing to about 95 percent at 600 GHz (see Table 1.1). This make a human body appear warm relative to a metal object, which would have a low emissivity and would thus reflect the temperature of the environment around the body (generally considered cooler than the body themselves). Plastics and ceramics have emissivities higher than those of metal but lower than those of human emissivity, so they would also be visible compared with the body, though to a lesser extent. Figure 1.2 has a curve labeled ”Ground Object ∼300 K” that shows the amount of radiation versus wavelength for a perfectly black body at 300 Kelvin (K), i.e. at approximately room temperature. Both the amplitude and the wavelength of the radiation peak are dependent on the temperature of the object. The higher the temperature of the body, the shorter the wavelength of radiation where the peak of the curve occurs.

Passive imaging systems require that there be an apparent temperature difference, either positive or negative, between the body and its surroundings. While the surrounding environment is generally cooler than the human body, some passive imaging systems use noncoherent sources that surround the body to enhance contrast by making reflective objects appear warmer than the body. These detection systems require the ability to differentiate between the temperatures of adjacent areas within the target area. The operation of a passive millimeter-wave imager can be compared with the operation of a camera. The equivalent of light for a millimeter-wave imager is the millimeter-wave energy, and the equivalent of film in a camera is the detector array in a millimeter-wave imager.

The emissivity of an object (which is polarization dependent) is a function of the dielectric properties of its components, its surface roughness, and the angle of observation. A sampling of emissivities for diverse materials at normal incidence, and measured at one polarization, is given in Table 1.1. The surface brightness (or radiometric) temperature T_S of an object is defined as the product between its physical thermodynamic temperature T_0 and its emissivity (ϵ).

$$T_S = \epsilon T_0 \tag{1.1}$$

The variation in emissivities of common scene materials, as shown in Table 1.1, is an important factor in the generation of scene images by causing variations in the power radiated from different parts of the scene. If this

Object	Emissivity (%)
Uman skin	65 to 95
Plastics	30 to 60, depending on type
Paper	30 to 70, depending on moisture content
Ceramics	30 to 70
Water	50
Metal	~ 0

Table 1.1: Examples of Object Emissivity

were the only factor involved, then images could be formed by simply mapping measured values of T_S in the scene. However, the way the scene is illuminated is critical in the way the scene actually looks. For example, a metal plate with $\epsilon = 0$ will have $T_S = 0$, but, because it is highly reflective, it will appear to have the radiometric temperature of whatever it is reflecting. This effect is captured by a surface scattered radiometric temperature T_{SC} defined as the product of the objects reflectivity ρ and the radiometric temperature $T_{ILLUMINATOR}$ of whatever happens to be illuminating it.

$$T_{SC} = \rho T_{ILLUMINATOR} \tag{1.2}$$

Combining the terms T_S and T_{SC} gives the effective radiometric temperature T_E of the object.

$$T_E = T_S + T_{SC} = \epsilon T_0 + \rho T_{ILLUMINATOR} \tag{1.3}$$

In outdoor imaging, the primary source of illumination is the down-welling of radiation from the sky itself. When a radiometer (an instrument for detecting thermal radiation) is aimed at the zenith, the radiometer will detect not only the residual radiation from deep space, the well know Cosmic Microwave Background Radiation (CMBR), but the low level of radiation that down-wells from the atmosphere itself, yielding a measured brightness temperature on the order of 60 K at 94 GHz [8]. Thus, a metal object with $\epsilon = 0$ e $\rho = 1$ will have T_E=60 K, and will, thus, appear very cold in an image. Imaging can be accomplished by measuring T_E as a function of position in the scene, thus creating a two-dimensional (2-D) map or image of the scene. Note that the above is highly simplified, not taking into account such factors as viewing angles, surface orientation, polarization effects, variations in the sky temperature as a function of angle relative to zenith, and both atmospheric emission and attenuation along the line of sight of the measurement. Such factors have been accurately modeled in the simulations [30].

1.1.3 Imaging Principles

The observed radiometric temperature of a scene is based on the following factors: emissions from scene constituents, reflections of the down-welling sky radiation by the scene, up-welling atmospheric emissions between the scene and the observer, and propagation of electromagnetic energy from the scene to the observer. Figure 1.3 illustrates these scene constituents. Image contrast is provided by differences in material, temperature, and sky illumination of the scene. Sky illumination is typically low level, i.e., radiometrically cold, at the zenith, rising to ambient temperatures at the horizon. Notice that the Sun's illumination is not needed to generate a millimeter-wave radiometric temperature-based image of the scene.

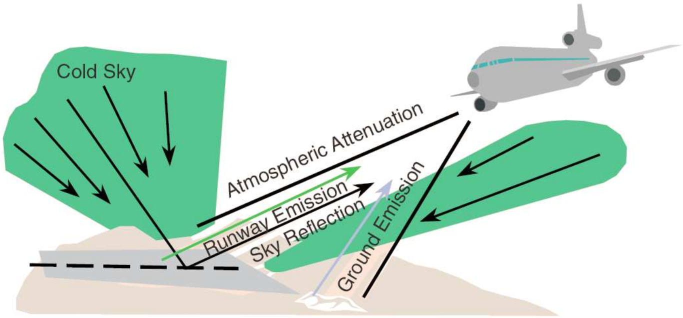

Figure 1.3: The observed image is the result of various radiometric effects.

An example of a radiometric image is illustrated in Figure 1.4. This figure contains a series of images that are obtained with a single 94-GHz radiometer mounted at the focus of a scanning 48-in diameter Cassegrain dish antenna. These images, acquired in both clear (b) and foggy (near zero visibility) (d) weather conditions , are of a runway as it would look to a pilot just before touchdown. Visible images (a) and (c) are included for comparison. The scanning process involved the repeated tilting of the dish antenna aim (pointing up and down) while slowly panning the entire dish from left to right. In this manner, the footprint of the antenna pattern on the scene was slowly moved over the entire scene. In this radiometric (or PMMW) image the increasingly darker shades denote increasingly colder radiometric temperatures, although this can be reversed for aesthetic or other reasons. The equipment parked next to the runway appears cold because their metal surfaces, which are nearly fully reflective, reflect the cold overhead sky. The asphalt runway, a good reflector at grazing incidence, reflects the sky at the horizon, which is warmer than the overhead sky. The dirt adjacent to the runway is colder than the asphalt because the roughness of the dirt surface mixes the reflections from various parts of the sky, effectively lowering the radiometric temperature of the dirt.

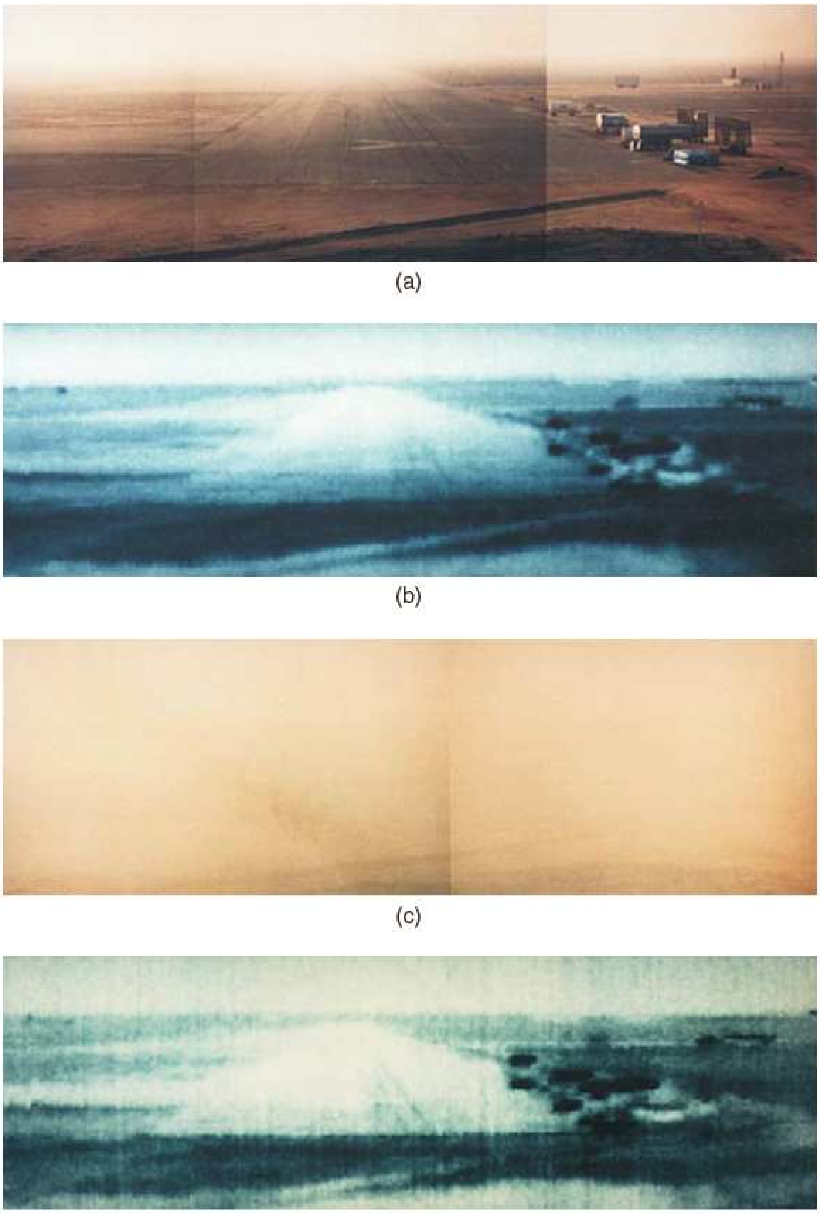

Figure 1.4: PMMW images of a runway viewed from the glide slope before touchdown: (a) and (c) show visible images in clear and foggy weather; (b) and (d) show the corresponding PMMW images.

The important features to be noticed in Figure 1.4 are the images through fog. The visual images are totally obscured except for the near foreground, while the PMMW images are nearly unaffected by the fog. An interesting feature that emerges from the PMMW images is the mirror reflection of the parked equipment on the asphalt runway. This occurs because the asphalt runway, instead of reflecting the warm sky at the horizon, now sees a colder part of sky overhead via reflections off the equipment. Note that PMMW images, unlike radar images, have a visual quality, but with less resolution than a visible light picture.

The limitation of PMMW imaging is that image resolution, i.e., sharpness is degraded compared to visible and IR images. The lower resolution is a consequence of the longer wavelengths used as compared to the aperture size of the sensors collection optics. Resolution improves increasing the aperture size. This is illustrated in Figure 1.5 at 94 GHz (3.1 mm wavelength) for three different dish antenna aperture sizes. As can be seen, the image becomes sharper as the aperture diameter increases. The same effect can also be attained with a higher frequency (shorter wavelength).

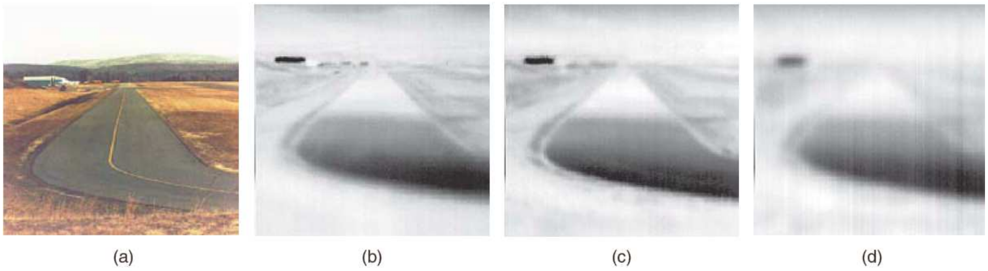

Figure 1.5: The airport scene in visible light (a) and with varying aperture sizes for the 94-GHz PMMW scanning system: (b) 120, (c) 60, and (d) 30 cm.

The limits on the resolution, however, will always limit the range over which imaging can be performed, and can be more restrictive than the atmospheric propagation constraints. For example, in Figure 1.5(b), just to the right of the large black bar in the upper left of the image, a large metal hangar building, are three black spots. These are school buses at a range of ~1 Km. These spots blur out to near nonexistence in Figure 1.5(d). Thus, the challenge is to construct a sensor that has such a high frequency that the sensor is small enough to fit easily within an aircraft platform, for example, and yet still provides sufficient resolution to permit safe and accurate navigation, landing, surveillance, or other desired functions.

1.2 The PMMW Camera

1.2.1 PMMW Imaging

As previously stated, all objects radiate or reflect natural radiation across the frequency spectrum. Similar to a visible camera (which detects visible radiation) and an IR camera (which detects IR radiation), a PMMW camera detects millimeter-wave radiation from the scene. All cameras are composed of a technique to measure the radiation level from the scene and a technique for forming the image (focusing the radiation onto the measurement device). The following will briefly describe these technique for the millimeter-wave range, that will, for the most part, be recognized as extensions of what is done in the microwave range.

The measurement of the scene radiation can be performed by a variety of methods. A typical method utilizes radiometers, which are basically calibrated receivers of thermal radiation. Radiometers come in several configurations, but the two most prevalent are the total power and the Dicke radiometers [69]. As the name implies, the total power radiometer simply integrates the power that the receiver collects and provides a measurement of the total power collected. Likewise, the Dicke radiometer collects the scene radiation, but for only half the time. During the other half, it views a reference load, and by rapidly switching between the two sources of radiation, it obtains a measurement of the received power level that is less sensitive to instrumental drifts. The receiver itself, whether configured as a total power or Dicke radiometer, can be built in many ways. The simplest is the bolometer, in which the incident radiation is focused onto a detector element, causing a temperature rise that is used to infer the incident power level. Somewhat more complex are electronic devices that directly amplify the incident radiation and measure the power content of the resultant signal using a particular detector. Finally, there are receiver designs that utilize both the amplitude and phase information of the incoming radiation. This chapter will deal primarily with total power or Dicke radiometer configurations using electronic amplification of the incoming signal. Then in the next chapters the radiometer's prototyping system working at 35 GHz I have studied during my PhD will be described.

There are also many techniques for forming the image. As described earlier, a single focused receiver can be raster scanned across the scene to form the image. The manner in which the radiation is focused onto the receiver varies from system to system, ranging from dish antennas as used by radio astronomers, to the quasi-optical use of plastic lenses having the proper dielectric constants. Systems have also been designed and built to scan a small array of focused receivers using mechanical methods (spinning mirrors or antennas, rotating arrays, etc.). Others scan a line array of focused receivers through the simple motion of an aircraft, a so-called pushbroom configuration in which the footprint of the array of receivers on the ground is swept along by the aircraft movement. In such a way it is possible to form an image simply vertically mounting the line array and rotating the camera around the vertical axis.

The most sophisticated methods involve the electronic scanning of the antenna pattern across the scene through phased-array techniques and interferometric methods using sparse arrays of widely separated antennas as performed in radio astronomy and other surveillance systems. Research groups around the world in academia, industry, and government have utilized these and other very novel and innovative methods to form PMMW images. This work will not review these many approaches, but the reader is referred to the suggested list of reading materials in the bibliography section.

In order to generate a video-like, real-time sequence of PMMW images, several methods have been investigated and developed around the world. These range from the rapid mechanical scanning of a small array, which has been shown to yield video-like PMMW imagery, to the complex but innovative phased-array approach utilizing the frequency range to perform the required rapid scanning [1]. A third approach uses a configuration similar to what is commonly used in visible and IR video cameras, that is, the use of a 2-D array of detectors. The millimeter-wave radiation from the objects within a scene is focused onto a Focal-Plane Array (FPA) of millimeter-wave receivers. By measuring and recording the variation in the resultant detected power or intensity levels across the scene, sequences of scene images can be collected and displayed to form a video-rate image stream.

1.2.2 PMMW Camera

Several recent technological advances have enabled the exploitation of millimeter waves. The advent of millimeter-wave monolithic integrated circuit (MMIC) technology has greatly increased the capabilities: direct, low-noise amplification, and detection of millimeter-wave radiation are now a reality. Low-noise amplifiers utilizing pseudomorphic high electron mobility transistor (PHEMT) technology on gallium arsenide (GaAs) substrates were first developed, then later combined with on-chip switches and a sensitive detector diode, to form a complete MMIC-based, 89-GHz Dicke-like receiver on a single 2 × 7-mm chip having a noise figure of 5.5 dB and bandwidth of 10 GHz [71].

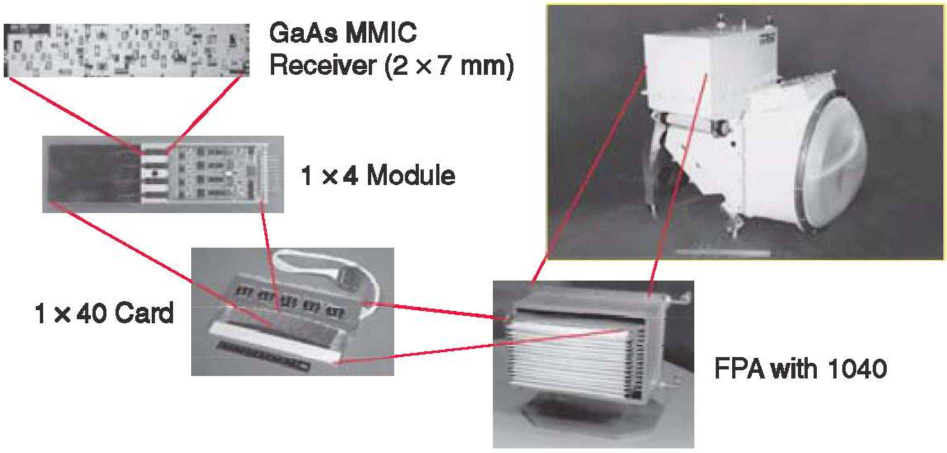

Figure 1.6: *The NGST PMMW video camera, shown here with its FPA components, was designed, built, and flight tested (from 1994-1999) by a consortium led by NGST, with participation by Boeing, Honeywell, and Composite Optics, Inc. under a White House Joint Dual-Use Technology Project. This project was cofunded by the Defense Advanced Research Projects Agency and managed by the National Aeronautics and Space Administration-Langley Research Center.*

The combination of high-sensitivity, low-cost, and low-power operation afforded by this MMIC device has enabled the construction of the first FPA PMMW video camera in the world, shown in Figure 1.6 [20, 46]. The MMIC chip is shown in the upper left. Four of them are placed on a 1 × 4 module to form a building-block unit for the camera FPA. The full FPA contains 260 of these 1 × 4 Modules (1040 receivers), arranged in 26 planar cards of 40 receivers each. The PMMW video camera shown in Figure 1.6 uses a 46 cm diameter plastic lens to collect and focus the radiation (a secondary lens within the camera is not visible), yielding a diffraction-limited 0.5° angular resolution. The size of the array, coupled with the optics, yields a 15° horizontal × 10° vertical field of view. A 45° turning mirror directs the focused radiation onto the FPA. This mirror also serves to dither the image on the FPA, i.e., it moves the image to four locations at the corners of a 0.5 × 0.5-pixel square, thereby quadrupling the number of points and attaining

Nyquist sampling of the scene. The camera is capable of an image update rate of 17 Hz (with a display rate of 30 Hz), with a minimum resolvable temperature of ~ 2 K [76]. The PMMW video camera was successfully tested on the ground, in flight, and at sea [78]. Flight testing began in September 1997 aboard a U.S. Air Force KC-135 that was flown into numerous airports for runway approach imaging. Under contract with the Office of Naval Research, the PMMW video camera was also flown on a UH-1N helicopter and a Twin Otter aircraft along the coast between Los Angeles and San Diego, California. Video-rate image sequences were collected from altitudes ranging from 150 to 450 m in both clear and overcast conditions [77].

1.2.3 Applications

As clearly indicated in the following, PMMW imaging sensors are useful for a wide variety of commercial and military missions requiring near-all-weather operations, as well as covertness (since there are no camera emissions). In addition, high sensitivity to metal objects, man-made targets, and ship wakes, as well as reduced sensitivity to variations in clutter, make a PMMW video camera an effective sensor asset. All of the images were taken either with the NGST PMMW video camera (single frames or sequences of single frames from the video sequence can only be shown here) or with a single raster-scanned 94-GHz radiometer mounted on a dish antenna, both described earlier in this chapter.

1.2.4 Imaging of People and Concealed Weapons Detection

The imaging of people in the millimeter-wave range produces images *that are somewhat strange*, especially when taken outdoors. Millimeter waves can easily penetrate clothing and hair. An image of a person will reveal a figure like a mannequin. The detected millimeter wave radiation is a combination of the natural emissions from the body and, since skin has a reflectivity on the order of 10%, what is reflected from the surroundings.

When outdoors, the sky is reflected off the skin of the upper surfaces of various body structures, while the warm ground is reflected by the lower body surfaces. This is illustrated in Figure 1.7, which was generated with a single 94-GHz radiometer mounted on a scanning 60 cm dish antenna adjusted to focus at 7.5 m.

If an object is placed under the clothing that has a dielectric constant different than skin, the millimeter wave image will reveal a radiometric

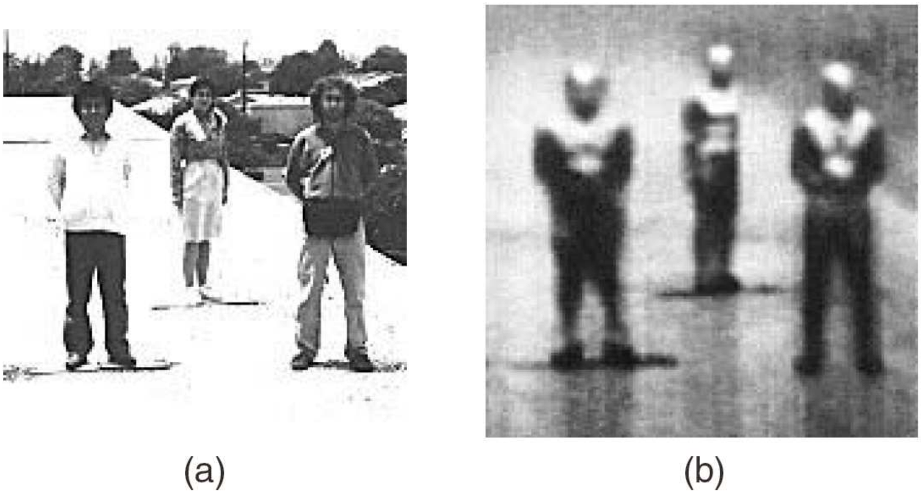

Figure 1.7: (a) Visible image and (b) PMMW image of three people standing in the open outdoors. White represents cold.

temperature change caused by the object. For example, a metal gun hidden under the clothing will not only block the natural emissions from the body but will reflect the radiation from the surroundings. Even nonmetallic objects, such as plastics and ceramics, will have a similar effect.

If indoors, where the room is illuminating the body with radiation at 295 K, the body's warmer emissions will be blocked or attenuated, and the object will be revealed to a PMMW imaging camera. Figure 1.8 is a collection of PMMW images of a person sitting indoors with various concealed weaponry. These were generated with a single 94-GHz radiometer on a scanning 60 cm dish antenna and adjusted to focus at 4.5 m. In all of the images, the person was wearing a cotton sweatshirt to conceal the weapons. As can be seen, the metal handgun is clearly visible. The orange plastic handgun on the left of the second figure is a training gun, while the other plastic handgun is a Glock with a metal barrel, and both are visible in the millimeter wave. The ceramic knives and the shrapnel in the plastic bag simulating a suicide bomber's weapon can also be seen.

1.2.5 Reconnaissance and Surveillance

An aircraft or unmanned aerial vehicle equipped with a PMMW camera can be used for near-all-weather look-down reconnaissance missions like the detection of ship wakes, low-radar cross-section boats, critical mobile, or other targets. In Figure 1.9, a single frame from a sequence taken by

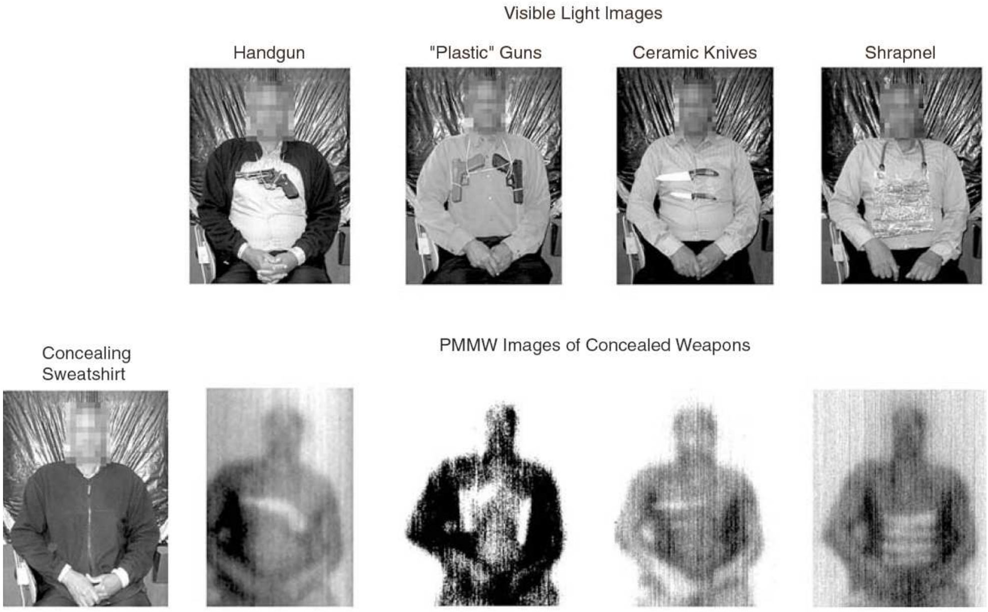

Figure 1.8: Visible (top row) and corresponding PMMW images of an individual with various weapons concealed by the sweatshirt shown in the first picture of the bottom row. The PMMW images were acquired indoors with a 94-GHz radiometer on a scanning 60 cm dish antenna. White represents cold in these images.

the PMMW video camera mounted on a Twin Otter, is superimposed on the corresponding visible-light still from a coboresighted video camera. An airplane C-17 is resolved from an altitude of 900 m. The PMMW signature of metal targets is unique in the PMMW frequency range, thus permitting auto-detection of such targets, as it is evident in Figure 1.9, where black shows colder objects. The image on the right is of roadways and buildings imaged through a cloud bank, from an altitude of 580 m.

Figure 1.9: On the left: PMMW imagery superimposed on a visible-light still frame of a C-17 on a taxiway. On the right: PMMW image of roadways and buildings through clouds.

1.2.6 Low-Visibility Navigation and Situation Awareness

A PMMW imaging system can be employed on patrol boats and amphibious landing vehicles (LCACs) as well as other ground and seagoing vehicles to provide covert, near-all-weather visibility for navigation, target location, and other enhanced vision needs, especially in fog and through marine cloud layers. Figure 1.10 shows a raster-scanned image (using a single 94-GHz radiometer at the focus of a 120 m aperture dish antenna) of a harbor scene in Long Beach, California, that would not have been impeded by fog if it had been present. Note the metal-domed structure reflecting the cold sky.

(a)

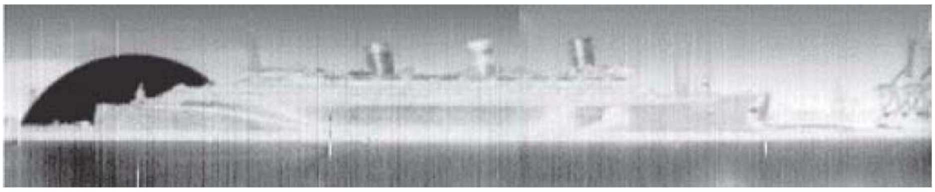

(b)

Figure 1.10: (a) Visible and (b) PMMW images of the Queen Mary and former Spruce Goose dome in Long Beach, California, harbor. The ship is 1,700 ft from the imaging system; black represents cold.

1.2.7 Perimeter Surveillance

Near-all-weather surveillance of harbors, docks, and other designated areas can be performed with PMMW sensors. In addition, monitoring of all traffic in and out of specified areas is easily accomplished.

1.2.8 Other applications

Other interesting applications can be envisaged profiting by the capability of millimeter-wave camera: aircraft landing and guidance; search and rescue; ground navigation; drug interdiction; beacon detection; oil-spill detection;

monitoring volcano activity through the smoke; control of the vehicular traffic through the smoke and the smog inside the galleries; etc.

1.3 Conclusion

PMMW imaging has a variety of applications that can be of great utility to make life safer and provide the military with a key advantage under low-visibility conditions, such as in fog, clouds, smoke, or sandstorms. Some of these applications have been presented with sample imagery, but many others are being studied by investigators around the world. Particularly exciting has been the advancement of MMIC technology to allow the development of the video-rate PMMW camera. The near-all-weather operation holds the promise of providing an autonomous enhanced vision landing capability for commercial airlines and the covert manner and the uniqueness of the PMMW signatures of targets of interest make this new window in the electromagnetic spectrum extremely promising for all branches of military applications. With the advent of the PMMW video camera and the ability to view the world in the millimeter-wave range, low-visibility conditions as a threat to safety or a hindrance to travel will be overcome.

Chapter 2

Ka-Band Imaging Camera

2.1 Introduction

The advanced technology involved in Planck satellite opens new opportunities in the field of mm-wave technologies. The *ViKy* (*"Video camera per Imaging in Ka banda"*) project was born as one of the possible spin-off based on the technology transfer of Planck. The aim of this project is to develop a mm-wave imaging camera. A key part of *ViKy* project is the design of a compact and low cost antenna suitable for development of a commercial product. The adopted solution is a mechanical beam scanning reflectarray antenna.

In this chapter, an overview of the *ViKy* project is presented. The antenna optimal configuration for *ViKy* has been derived as a trade off between the image quality needed and cost.

2.2 The *ViKy* project

The Low Frequency Instrument (LFI) is an Italian led instrument that will be located on board the ESA Planck satellite devoted to cosmology; it is the most advanced mm-wave instrumentation based on the state-of-the-art in the radiometric and bolometric technology, as well as in cryogenics. LFI is an High Electron Mobility Transistor (HEMT) based array working at 30, 44 and 70 GHz built by a consortium of more than 22 scientific institutes led by the Principal Investigator N. Mandolesi of the Istituto di Astrofisica Spaziale e Fisica Cosmica (IASF) in Bologna, Italy. IASF is part of the nationwide Istituto Nazionale di Astrofisica (INAF) whose activities are devoted to ground and space astrophysics. Moreover, INAF also operates in the field of technology transfer and know-how. Specifically, the *ViKy* project was born as one of the possible spin-off, based on the technology transfer of Planck/LFI.

The aim of this project is to develop a mm-wave imaging camera operating at 35 GHz. The receiver derives from the experience maturated in LFI.

It is well know that the atmosphere absorption changes dramatically form visible wavelength to microwaves. In addition, weather conditions may affect the attenuation coefficient, depending on wavelength. The main interest in using microwave antennas is to obtain a very good compromise between electrical performances, due to the atmospheric attenuation conditions, and mechanical dimensions of the antenna. The angular resolution (i.e. the HPBW) is proportional to the effective area of the antenna used, then to have useful angular resolution at low frequency range, where the atmospheric attenuation is negligible, a very big antenna is needed.

In the Figure 1.1 the atmospheric attenuation from 10 GHz to 1000 GHz is shown. The red-noisy line represents the atmospheric loss at different frequencies (20, 1 Atm, $H_2O = 7,5g/m^3$). In the same Figure other three lines appear, represent three different meteorological conditions: drizzle (0,25 mm/h), heavy rain (25 mm/h), deluge (150 mm/h). The upper line represents the fog $(0,1g/m^3)$ with visibility 50 m. There are two minimum of atmospheric attenuation at 35 and 94 GHz which provide good observational conditions for *ViKy*. At these frequency bands, electromagnetic waves may provide high contrast images in unfavourable weather conditions and may penetrate opaque solids. Millimeter wave detectors, like *ViKy*, can detect metal objects, since they reflect the sky, which is colder than the background emission.

Advantage and potentiality of mm-wave passive imaging are well known. Several prototypes have been developed by different research and industrial groups. Moreover, commercial millimeter wave passive images already exist, even if they are not diffused. Rather than to show the advantages of mm-waves, the aim of *ViKy* prototype is to demonstrate the feasibility and to identify the technology of the reflectarray antennas at these frequency and to assess low-cost technical solutions for passive imaging at millimeter wavelengths.

At higher frequencies from 20 to 100 GHz there are two different deeps in the attenuation curve; in this range the best frequency channel is centered in the Wband ($94GHz$) due to the best achievable resolution. However the *ViKy* team decided to build a prototype imaging camera working at 35 GHz for the following reasons:

- the Ka band is a well known frequency band extensively used in satellite applications and in many other commercial applications; active components, as amplifier or diodes, can be found at lower cost;
- the antenna solution chosen, that will be described later on, will employ technologies already used with well known mechanical tolerances.

At system level the prototype can be separate in five units:

- the antenna system able to receive the signal coming from the scene;
- the mechanical system that allows the raster scanning of the image;
- the radiometer that amplifies and detects the electromagnetic signal coming from the antenna;
- the data acquisition electronics;
- the software for the image processing and the customer interface.

2.3 Antenna System

2.3.1 Antenna specifications

The choice of the specifications depends on the usage. The demanded sensitivity and resolution for the antenna will depend on the use it is aimed at. For instance, an antenna used for airport security will differ from one used in the field of medical diagnostic. The aim of the *ViKy* system is to provide a real time optical image obtained from the radiometric signal by imaging processing. The following specifications are chosen for the concealed object detection.

For the theorem of the critical sampling (see [66]) the step can be 1/3 or 1/2 by the beam at 3dB. This allows the reduction of the antenna dimensions.

2.4 Antenna Design and Technology

A reflectarray combines the features of both array antennas and reflector and was first introduced by Berry in 1963 [7]. A reflectarray basically is an array of antennas illuminated by a feed horn instead of being fed by conventional transmission line feeding. There are several advantages of this type of antenna as compared to the phased array or conventional reflector, but the most important among these is the capability to implement a scanning

Parameters:	1th case	2nd case	Unit:
Resolution	10^2	0.4	m
Obj. distance	3	100	m
Obj. dimensions	2×1		m^2
Azimuth angle	±10		deg
$\Delta\theta_{Az}$ (3dB)	0.6	0.23	deg
Elevation angle	±20		deg
$\Delta\theta_{El}$ (3dB)	0.6	0.23	deg
Imaging processing			
Frame	1	1	sec
Integration time	5^{-5}	5^{-5}	sec
$FWHM = \Delta\theta_{Az} \cdot \Delta\theta_{El}$	$0.6 \cdot 0.6$	$0.6 \cdot 0.6$	deg · deg
Step scanning angle	0.2	0.69	deg

Table 2.1: Antenna specifications

antenna without the need of complex feed network or expensive mechanical movements.

The concept of reflectarray, made of microstrip patches printed on a dielectric substrate, was first presented by Malagisi in 1978 [49]. The reflectarray concept is shown in Figure 2.1. During the last tens years many theoretical studies and experimental works have been presented. They mainly focused their efforts on these points: the use of different geometries of patches to obtain higher bandwidth and the investigation of novel ways of introducing a phase change in the impedance of the patches to obtain a shift in the main beam of the antenna (see [39, 14]).

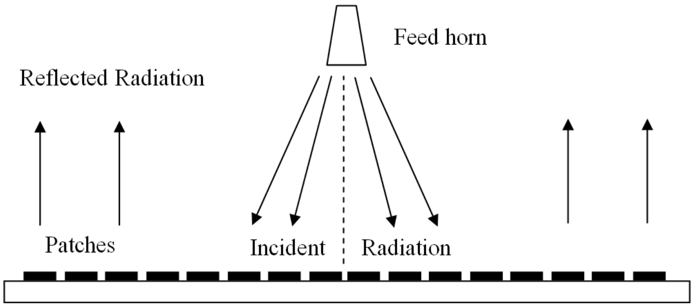

Figure 2.1: The reflectarray concept.

The *ViKy* antenna that is under design is a single layer microstrip patch antenna. The solution adopted offers many advantages as well as disadvantages. One of the latter is the narrow bandwidth of the system.

In principle there is no such need of bandwidth because the physical phenomenon is present at all the frequency bands, but the more large is the band the more sensitivity we can obtain as shown in § 2.5. A typical bandwidth of reflectarray applications is a few percent of the band. It is possible to improve the bandwidth with multilayer design, i.e. by patches coupled with slots on ground planes [14]. This solution and other multilayer solutions give rice to the problem of aligning the layers, what could be not trivial to be solved at 35 GHz. In the future, the *ViKy* project will use MEMS related technology [63] to connect each patch by a varactor diode to the ground. The varactor diode will change in a mostly continuous way the impedance of the patch to obtain different phase contribution (see [10, 68]). The typical phase variation of such components is show in the Figure 2.2. The application needs to operate such reflectarray in near field to obtain the requested specifications. In near field the assumptions made in the typical array design for far field applications are no longer valid.

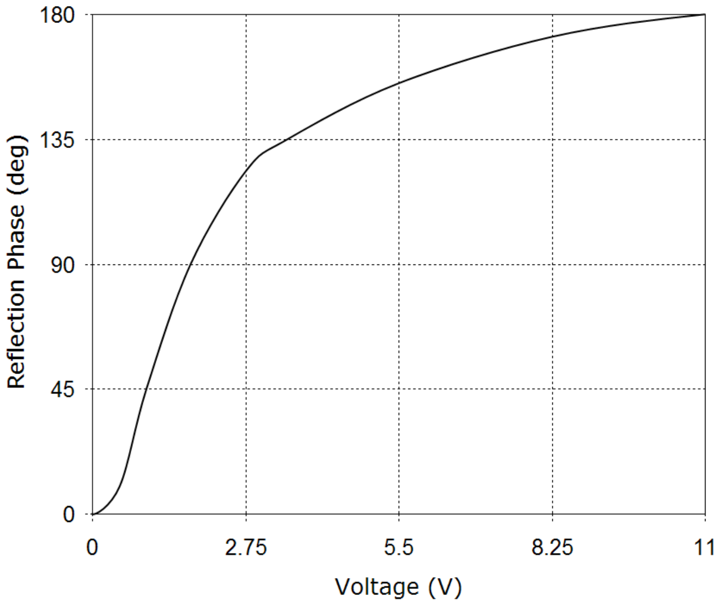

Figure 2.2: Reflection phase versus varactor bias.

In the next chapters I will describe the radiometer performances, required to obtain high contrast images, and the antenna configuration.

2.5 Radiometer specifications

The radiometer measures the signal coming from the antenna. The total gain of the radiometer needs to be high enough to output a measurable signal of the order of mV at least. The noise figure, together with the bandwidth and the integration time determines the minimum detectable signal by:

$$\Delta T_{rms} = \frac{\alpha \cdot (T_A + T_N)}{\sqrt{\Delta\nu \cdot \frac{1}{N_{pixel} \cdot F_{rate}}}} \tag{2.1}$$

where α is a coefficient depending on the kind of receiver, $\Delta\nu$ is the bandwidth, N_{pixel} is the image total number of pixels, F_{rate} is the frame rate of the image, T_N is the noise temperature of the radiometer, and T_A is the antenna temperature. Ka band commercial amplifiers show a typical noise figure (NF) of about 3 dB ($\sim 300K$ of noise temperature) according to $NF|_{dB} = 10 \cdot \log[(T_N/295) + 1]$. With such amplifiers, a 10 % of bandwidth, and a frame rate of 1 Hz, the minimum detectable signal is of the order of 1 K for a 300 K typical target temperature. High contrast images may be possible with this sensitivity. The radiometer input signal is of the order of $10^{-10} \div 10^{-11}$ Watts. Hence, a gain of 70 dB at least is required to provide at the output a detectable signal. The performace of the commercial Low Noise Amplifier (LNA) that will be used in this prototype is reported in Table 2.2.

Technology	HEMT
Number of stages	2
Total Gain	72.5 dB
Frequency band	35 GHz ±5÷10 %
Noise Figure	2.72dB
Detector Sensitivity	2612 mV/mW

Table 2.2: Radiometer specifications

Chapter 3

Microstrip Antennas

3.1 Introduction

In high-performance aircraft, spacecraft, and satellite applications, where size, weight, cost, performance, ease of installation, and aerodynamic profile are constraints, low-profile antennas may be required. To meet these requirements, microstrip antennas (see [19, 60]) can be used. These antennas are low profile, conformable to planar and nonplanar surfaces, simple and inexpensive to manufacture using modern printed-circuit technology, mechanically robust when mounted on rigid surfaces, compatible with MMIC designs. When the particular patch shape and mode are also selected, they are very versatile in terms of resonant frequency, polarization, pattern, and impedance.

This chapter introduces the concept of Microstrip Antennas, describes the principal methods of analysis and explains the main techniques used to simulate the problem, from an electromagnetic point of view, with commercial softwares.

3.1.1 Basic Characteristics

Microstrip antennas, as shown in Figure 3.1(a), consist of a very thin ($t \ll \lambda_0$, where λ_0 is the free-space wavelength) metallic strip (patch) placed a small fraction of a wavelength ($h \ll \lambda_0$, usually $0.003\lambda_0 \leq h \leq 0.05\lambda_0$) above a ground plane. The microstrip patch is designed such that its pattern maximum should be normal to the patch (broadside radiator). This is accomplished by properly choosing the mode (field configuration) of excitation beneath the patch. End fire radiation (the radiation in the opposite direction respect to the broadside radiation) can also be accomplished by judicious mode selection. For a rectangular patch, the length L of the

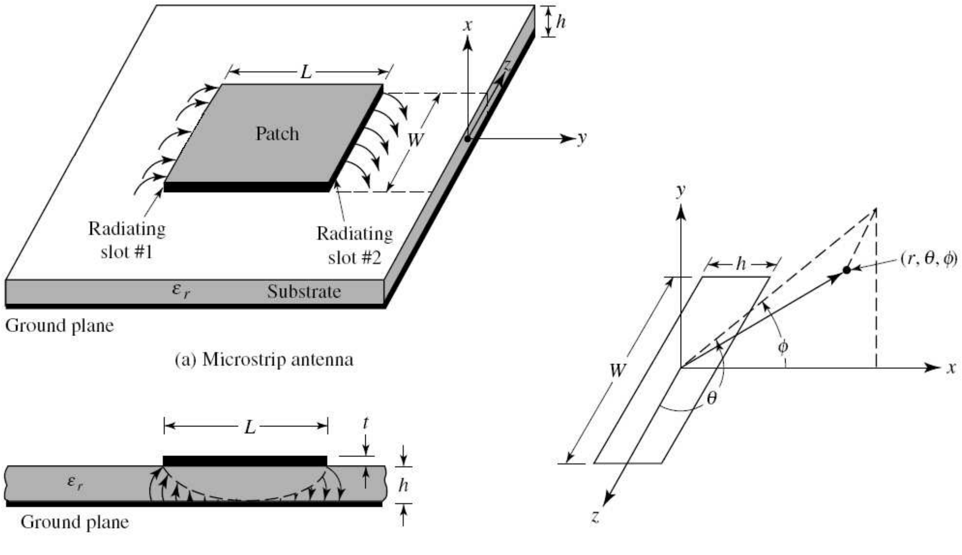

(a) Microstrip antenna

(b) Side view

(c) Coordinate system for each radiating slot

Figure 3.1: Microstrip antenna and coordinate system.

element is usually $\lambda_0/3 < L < \lambda_0/2$. The strip (patch) and the ground plane are separated by a dielectric sheet (referred to as the substrate), as shown in Figure 3.1(a). There are numerous substrates that can be used for the design of microstrip antennas, and their permittivities are usually in the range of $2.2 \leq \epsilon_r \leq 12$.

Often microstrip antennas are also referred to as patch antennas. The radiating elements and the feed lines are usually photoetched on the dielectric substrate. The radiating patch may be square, rectangular, thin strip (dipole), circular, elliptical, triangular, or of any other configuration as illustrated in Figure 3.2. Square, rectangular, dipole (strip), and circular are the most common because of ease of analysis and fabrication and their attractive radiation characteristics, especially low cross-polarization radiation. Linear and circular polarizations can be achieved with either single elements or arrays of microstrip antennas. Arrays of microstrip elements, with single or multiple feeds, may also be used to introduce scanning capabilities and achieve greater directivities.

3.1.2 Feeding Methods

There are many configurations that can be used to feed microstrip antennas. The four most popular are the microstrip line, coaxial probe, aperture coupling, and proximity coupling (see [2, 12, 41, 60]). These are displayed

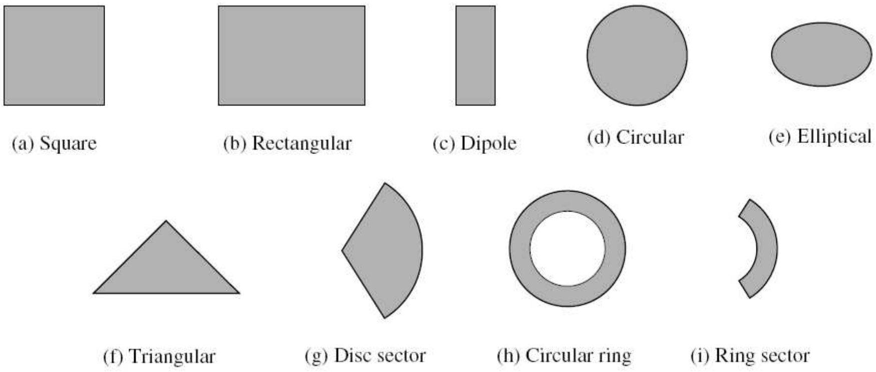

Figure 3.2: Representative shapes of microstrip patch elements.

in Figure 3.3. One set of equivalent circuits for each one of these is shown in Figure 3.4

The microstrip feed line is also a conducting strip, usually of much smaller width compared to the patch. The microstrip-line feed is easy to fabricate, simple to match by controlling the inset position and rather simple to model. However as the substrate thickness increases, surface waves and spurious feed radiation increase, which for practical designs limit the bandwidth (typically $2 \div 5\%$).

Coaxial-line feeds, where the inner conductor of the coax is attached to the radiation patch while the outer conductor is connected to the ground plane, are also widely used. The coaxial probe feed is also easy to fabricate and match and has low spurious radiation. However, it too has narrow bandwidth and is more difficult to model, especially for thick substrates ($h > 0.02\lambda_0$).

Both the microstrip feed line and the probe possess inherent asymmetries which generate higher order modes which produce cross-polarized radiation. To overcome some of these problems, noncontacting aperture-coupling feeds, as shown in Figures 3.3(c,d), have been introduced. The aperture coupling of Figure 3.3(c) is the most difficult of all four to fabricate and it too has narrow bandwidth. However, it is somewhat easier to model and has moderate spurious radiation. The aperture coupling consists of two substrates separated by a ground plane. On the bottom side of the lower substrate lies a microstrip feed line whose energy is coupled to the patch through a slot on the ground plane separating the two substrates. This arrangement allows independent optimization of the feed mechanism

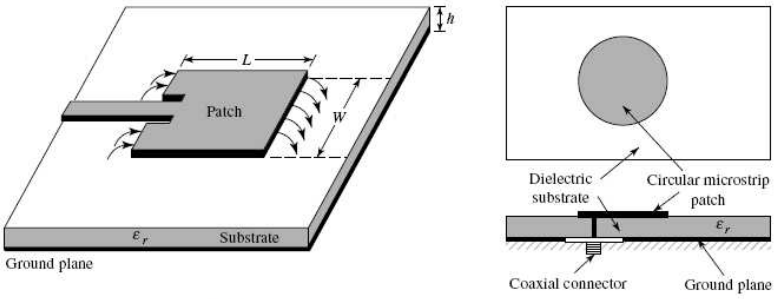

(a) Microstrip line feed (b) Probe feed

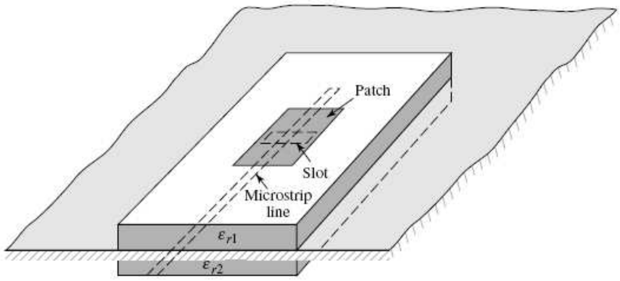

(c) Aperture-coupled feed

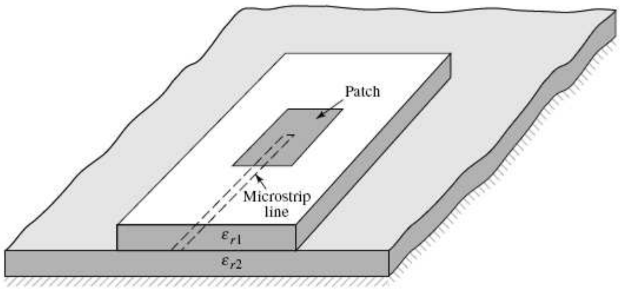

(d) Proximity-coupled feed

Figure 3.3: Typical feeds for microstrip antennas.

and the radiating element. Typically, a high dielectric material is used for the bottom substrate, and thick low permittivity material for the top substrate. The ground plane between the substrates also isolates the feed from the radiating element and minimizes interference of spurious radiation for pattern formation and polarization purity.

Of the four feeds described here, the proximity coupling has the largest bandwidth (as high as 13 percent), is somewhat easy to model and has low spurious radiation. However its fabrication is somewhat more difficult. The length of the feeding stub and the width to line ratio of the patch can be used to control the match [56].

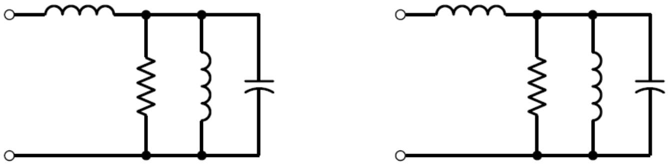

(a) Microstrip line (b) Probe

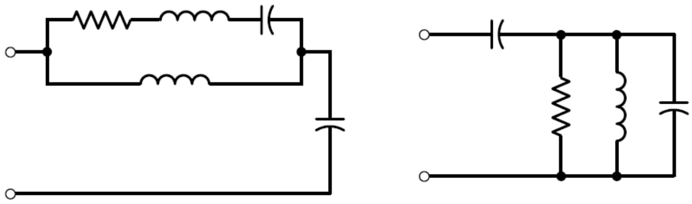

(c) Aperture-coupled (d) Proximity-coupled

Figure 3.4: Equivalent circuits for typical feeds of Figure 3.3.

3.2 Methods of analysis

There are many methods of analysis for microstrip antennas. The most popular models are the transmission-line [12, 38], cavity [47, 12, 38], and full wave (which include primarily integral equations or moment method) [62, 3]. The transmission-line model is the easiest of all, it gives good physical insight, but is less accurate and presents more difficulties to model coupling. Compared to the transmission-line model, the cavity model is more accurate but at the same time more complex. In general, when applied properly, the full-wave models are very accurate and versatile and can treat single elements, finite and infinite arrays, stacked elements, arbitrary shaped elements and coupling. In this chapter I will cover the transmission-line and some aspects related to the cavity models. Results and design from full-wave models will also be included in the chapter dedicated to the electromagnetic simulations. Since it is used in the *ViKy* project, in this chapter the only patch configuration that will be considered is the rectangular one.

3.2.1 Transmission Line Model for Rectangular Patch

The rectangular patch is by far the most widely used configuration. It is very easy to analyze using both the transmission-line and cavity models, which are most accurate for thin substrates [67].

Fringing effects

As the dimensions of the patch are finite along the length and width, the fields at the edges of the patch undergo fringing. This is illustrated along the length in Figures 3.1(a,b) for the two radiating slots of the microstrip antenna. The same applies along the width. The amount of fringing is a function of the dimensions of the patch and the height of the substrate. For the principal E-plane (xy–plane) fringing is a function of the ratio of the length of the patch L to the height h of the substrate (L/h) and the permittivity ϵ_r of the substrate. Since for microstrip antennas $L/h \gg 1$, fringing is reduced; however, it must be taken into account because it influences the resonant frequency of the antenna. The same applies for the width (W) of the patch.

For a microstrip line shown in Figure 3.5(a), typical electric field lines are shown in Figure 3.5(b). This is a nonhomogeneous line of two dielectrics; typically the substrate and air. As can be seen, most of the electric field lines reside in the substrate and parts of some lines lie in air. As $W/h \gg 1$ and $\epsilon_r \gg 1$, the electric field lines concentrate mostly in the substrate. Fringing in this case makes the microstrip line look electrically wider compared to its physical dimensions. Since a portion of each wave travels in the substrate and the remaining in air, an *effective permittivity* ϵ_{r_eff} is introduced to account for fringing and the wave propagation in the two means.

To introduce the effective permittivity, let us assume that the center conductor of the microstrip line with its original dimensions and height above the ground plane is embedded into one dielectric, as shown in Figure 3.5(c). The effective permittivity is defined as *the permittivity of the uniform dielectric material so that the line of Figure 3.5(c) has identical electrical characteristics, particularly propagation constant, as the actual line of Figure 3.5(a).* For a line with air above the substrate, the effective permittivity has values in the range of $1 < \epsilon_{r\_eff} < \epsilon_r$. For most applications where the permittivity of the substrate is much greater than unity ($\epsilon_r \gg 1$), the value of ϵ_{r_eff} will be closer to the value of the actual permittivity ϵ_r of the substrate. The effective permittivity is also a function of frequency. As the frequency of operation increases, most of the electric field lines concentrate in the substrate. Therefore the microstrip line behaves more like a homogeneous line of one dielectric (only the substrate), and the effective permittivity approaches the value of the permittivity of the substrate. Typical variations, as a function of frequency, of the effective dpermittivity for a microstrip line with three different substrates are shown in Figure 3.6.

For low frequencies the effective permittivity is essentially constant. At intermediate frequencies its values begin to monotonically increase and eventually approach the values of the permittivity of the substrate, which are reported in Figure 3.6. The initial values (at low frequencies) of the effective permittivity are referred to as the static values, and they are given approximately by [4]:

$$W/h > 1 \tag{3.1}$$

$$\epsilon_{r\_eff} = \frac{\epsilon_r + 1}{2} + \frac{\epsilon_r - 1}{2}\left[1 + 12\frac{h}{W}\right]^{-1/2} . \tag{3.2}$$

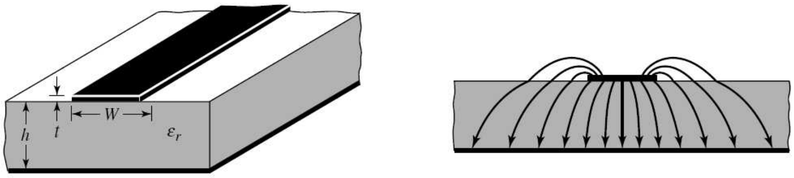

(a) Microstrip line

(b) Electric field lines

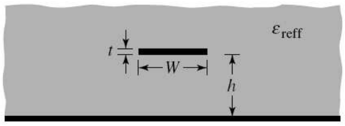

(c) Effective dielectric constant

Figure 3.5: Microstrip line and its electric field lines, and effective permittivity geometry.

Effective Length, Resonant Frequency and Effective Width

Because of the fringing effects, electrically the patch of the microstrip antenna looks greater than its physical dimensions. For the principal E-plane (xy-plane), this is demonstrated in Figure 3.7 where the dimensions of the patch along its length have been extended on each end by a distance ΔL, which is a function of the effective permittivity ϵ_{r_eff} and the width-to-height ratio (W/h). A very usual approximate relation for the normalized extension of the length is [26]

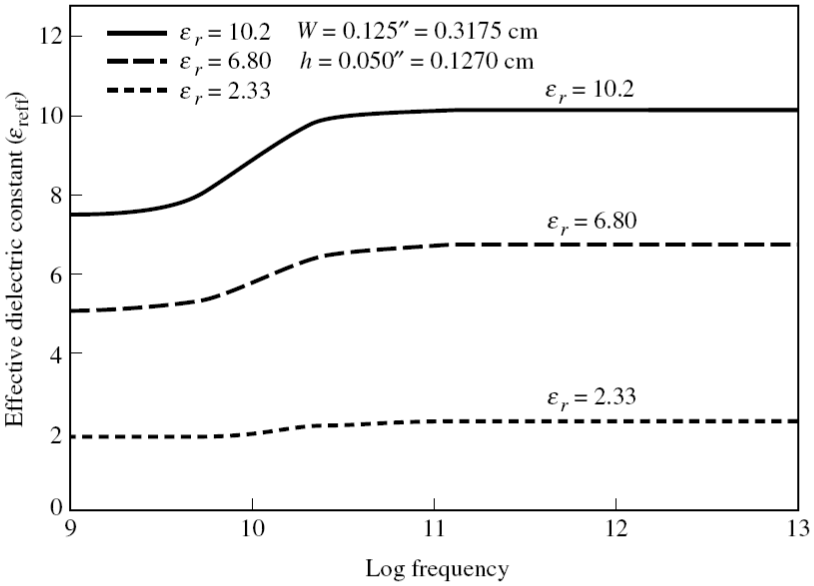

Figure 3.6: Effective permittivity versus frequency for typical substrates.

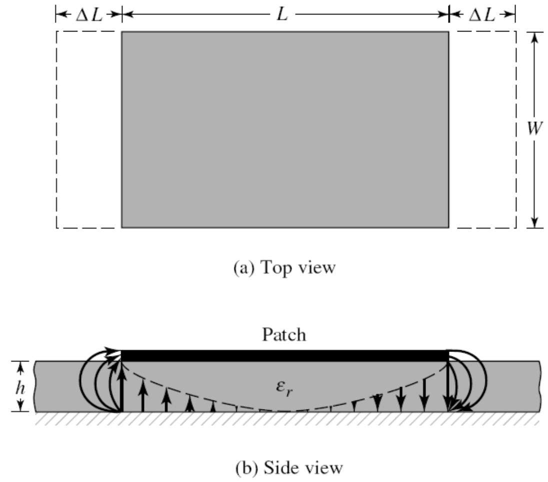

Figure 3.7: Physical and effective lengths of rectangular microstrip patch.

$$\frac{\Delta L}{h} = 0.412 \frac{(\epsilon_{r\_eff} + 0.3)\left(\frac{W}{h} + 0.264\right)}{(\epsilon_{r\_eff} - 0.258)\left(\frac{W}{h} + 0.8\right)} \quad . \tag{3.3}$$

Since the length of the patch has been extended by ΔL on each side, the effective length of the patch is now ($L = \lambda/2$ for dominant TM_{010} mode with no fringing)

$$L_{eff} = L + 2\Delta L \quad . \tag{3.4}$$

For the dominant TM_{010} mode, the resonant frequency of the microstrip antenna is a function of its length. In literature it is given by:

$$(f_r)_{010} = \frac{1}{2L\sqrt{\epsilon_r}\sqrt{\mu_0\epsilon_0}} = \frac{v_0}{2L\sqrt{\epsilon_r}} \tag{3.5}$$

where v_0 is the velocity of light in free space. Since Equation 3.5 does not account for fringing, it must be modified to include edge effects and should be computed using

$$\begin{aligned}(f_{rc})_{010} &= \frac{1}{2L_{eff}\sqrt{\epsilon_{r\_eff}}\sqrt{\mu_0\epsilon_0}} = \frac{1}{2(L + 2\Delta L)\sqrt{\epsilon_{r\_eff}}\sqrt{\mu_0\epsilon_0}} \\ &= q\frac{1}{2L\sqrt{\epsilon_r}\sqrt{\mu_0\epsilon_0}} = q\frac{v_0}{2L\sqrt{\epsilon_r}}\end{aligned} \tag{3.6}$$

where

$$q = \frac{(f_{rc})_{010}}{(f_r)_{010}} \tag{3.7}$$

The q factor is referred to as the *fringe factor* (length reduction factor). As the substrate height increases, fringing also increases and leads to larger separations between the radiating edges and lower resonant frequencies.

Design

Based on the simplified formulation that has been described, a design procedure is outlined which leads to practical designs of rectangular microstrip antennas. The procedure assumes that the specified information includes the permittivity of the substrate (ϵ_r), the resonant frequency (f_r), and the height of the substrate h.

The procedure is as follows

Specify:

ϵ_r, f_r (in Hz) and h

Determine:

$$W, L$$

according to the following design procedure:

1. For an efficient radiator, a practical width that leads to good radiation efficiencies is [2]

$$W = \frac{1}{2f_r\sqrt{\mu_0\epsilon_0}}\sqrt{\frac{2}{\epsilon_r+1}} = \frac{v_0}{2f_r}\sqrt{\frac{2}{\epsilon_r+1}} \tag{3.8}$$

   where v_0 is the free-space velocity of light.

2. Determine the effective permittivity of the microstrip antenna using (3.2).

3. Once W is found using (3.8), determine the extension of the length ΔL using (3.3).

4. The actual length of the patch can now be determined by solving (3.6) for L, or

$$L = \frac{1}{2f_r\sqrt{\epsilon_{r\_eff}}\sqrt{\mu_0\epsilon_0}} - 2\Delta L \tag{3.9}$$

Conductance

A very important concept related to the transmission line model is the conductance; in terms of electromagnetic fields each radiating slot can be represented by an equivalent circuit characterized by an admittance (Y), a conductance (G) and susceptance (B).
Admittance is an expression of the ease with which alternating current (AC) flows through a complex circuit or system. Admittance is a vector quantity expressing two independent scalar phenomena: conductance and susceptance .

Conductance is a measure of the ease with which charge carriers can pass through a component or substance. The more easily the charge carriers move in response to a given applied electric potential, the higher the conductance, which is expressed in positive real-number Siemens . Conductance is observed with AC and also with direct current (DC).

Susceptance is an expression of the readiness with which an electronic component, circuit, or system releases stored energy as the current and voltage fluctuate. Susceptance is expressed in imaginary number Siemens. It is observed for AC, but not for DC.

When AC passes through a component that has susceptance, energy might be stored and released in the form of a magnetic field, in which case the susceptance is inductive (denoted $-jB_L$), or energy might be stored and released in the form of an electric field, in which case the susceptance is capacitive (denoted $+jB_C$).

Admittance is the vector sum of conductance and susceptance. Susceptance is conventionally multiplied by the positive square root of -1, the so called unit imaginary number symbolized by j , to express Y as a complex quantity $G - jB_L$ (when the net susceptance is inductive) or $G + jB_C$ (when the net susceptance is capacitive).

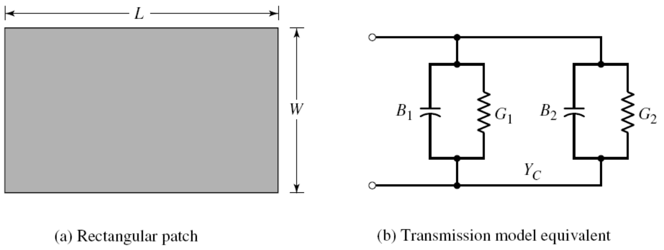

(a) Rectangular patch

(b) Transmission model equivalent

Figure 3.8: Rectangular microstrip patch and its equivalent circuit transmission-line model.

In parallel connenctions, conductance and susceptance add together independently to yield the composite admittance. In Figure 3.8 both a rectangular patch and its parallel equivalent circuit are shown.

The slots are labeled as #1 and #2. The equivalent admittance of slot #1, referred to an infinitely wide, uniform slot, is given by [29]:

$$Y_1 = G_1 + jB_1 \, , \tag{3.10}$$

where for a slot of finite width W, a free-space propagation vector $k_0 = \frac{2\pi}{\lambda_0}$ and a free-space wavelength λ_0

$$G_1 = \frac{W}{120\lambda_0}\left[1 - \frac{1}{24}(k_0 h)^2\right] \tag{3.11}$$

$$B_1 = \frac{W}{120\lambda_0}\left[1 - 0.636\ln(k_0 h)\right] \qquad \text{when} \qquad \frac{\mathrm{h}}{\lambda_0} < \frac{1}{10} \tag{3.12}$$

Since slot #2 is identical to slot #1, its equivalent admittance is

$$Y_2 = Y_1, \qquad G_2 = G_1, \qquad B_2 = B_1 \tag{3.13}$$

The conductance of a single slot can also be obtained by using the field expression derived by the cavity model.
Considering the electric field expression:

$$E_\phi \simeq +j\frac{V_0 e^{-jk_0 r}}{\pi r}\left\{\sin\theta \frac{\sin(\frac{k_0 W}{2}\cos\theta)}{\cos\theta}\right\} \tag{3.14}$$

where V_0 is the voltage across the slot. The radiated field power is written as

$$P_{rad} = \frac{|V_0|^2}{2\pi\eta_0}\int_0^\pi \left[\frac{\sin\left(\frac{k_0 W}{2}\cos\theta\right)}{\cos\theta}\right]^2 \sin^3\theta d\theta \tag{3.15}$$

In general, the conductance is defined as

$$G_1 = \frac{2P_{rad}}{|V_0|^2} \tag{3.16}$$

Therefore the conductance of Equation (3.16) can be expressed as

$$G_1 = \frac{I_1}{120\pi^2} \tag{3.17}$$

where

$$\begin{aligned} I_1 &= \int_0^\pi \left[\frac{\sin\left(\frac{k_0 W}{2}\cos\theta\right)}{\cos\theta}\right]^2 \sin^3\theta d\theta \\ &= -2 + \cos(X) + XS_i(X) + \frac{\sin(X)}{X} \end{aligned} \tag{3.18}$$

$$X = k_0 W \tag{3.19}$$

Asymptotic expressions for Equations (3.17) and (3.18) are

$$G_1 = \begin{cases} \frac{1}{90}\left(\frac{W}{\lambda_0}\right)^2 & W \ll \lambda_0 \\ \frac{1}{120}\left(\frac{W}{\lambda_0}\right) & W \gg \lambda_0 \end{cases} \tag{3.20}$$

The values of Equation (3.20) for $W \ll \lambda_0$ are identical to those given by (3.11) for $h \ll \lambda_0$. A plot of G as a function of W/λ_0 is shown in Figure 3.9.

Resonant Input Resistance

The total admittance at slot #1 (input admittance) is obtained by transferring the admittance of slot #2 from the output terminals to input terminals using the admittance transformation equation of transmission lines [12, 4, 15].

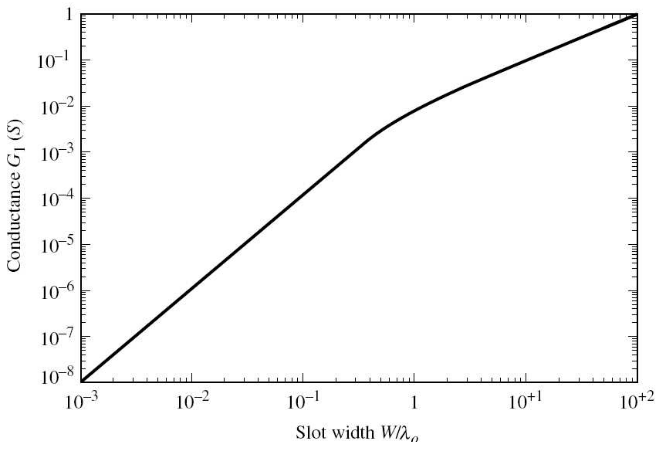

Figure 3.9: Slot conductance as a function of slot width.

Ideally the two slots should be separated by $\lambda/2$ where λ is the wavelength in the dielectric (substrate). However, because of fringing, the length of the patch is electrically greater than the geometric length. Therefore the geometric separation of the two slots is slightly less than $\lambda/2$. If the reduction of the length is properly chosen using Equation (3.3) (typically $0.48\lambda < L < 0.49\lambda$), the transformed admittance of slot #2 becomes

$$\tilde{Y}_2 = \tilde{G}_2 + j\tilde{B}_2 = G_1 - jB_1 \tag{3.21}$$

or

$$\tilde{G}_2 = G_1 \tag{3.22}$$

$$\tilde{B}_2 = -B_1 \tag{3.23}$$

Therefore the total resonant input admittance is real and is given by

$$Y_{in} = Y_1 + \tilde{Y}_2 = 2G_1 \tag{3.24}$$

Since the total input admittance is real, the resonant input impedance is also real, or

$$Z_{in} = \frac{1}{Y_{in}} = R_{in} = \frac{1}{2G_1} \tag{3.25}$$

The resonant input resistance, as given by (3.25), does not take into account mutual effects between the slots. This can be accomplished by modifying (3.25) to [18]

$$R_{in} = \frac{1}{2(G_1 \pm G_{12})} \tag{3.26}$$

where the plus (+) sign is used for modes with odd (antisymmetric) resonant voltage distribution beneath the patch and between the slots while the minus (-) sign is used for modes with even (symmetric) resonant voltage distribution. The mutual conductance is defined, in terms of the far-zone fields, as

$$G_{12} = \frac{1}{|V_0|^2} \operatorname{Re} \iint_S \mathbf{E}_1 \times \mathbf{H}_2^* \cdot d\mathbf{s} \tag{3.27}$$

where $\mathbf{E}_1$ is the electric field radiated by slot #1, $\mathbf{H}_2$ is the magnetic field radiated by slot #2, V_0 is the voltage across the slot, and the integration is performed over a sphere of large radius. It can be shown that G_{12} can be calculated using [18], [64]

$$G_{12} = \frac{1}{120\pi^2} \int_0^{\pi} \left[\frac{\sin\left(\frac{k_0 W}{2} \cos\theta\right)}{\cos\theta} \right]^2 J_0(k_0 L \sin\theta) \sin^3\theta d\theta \tag{3.28}$$

where J_0 is the Bessel function of the first kind of order zero. For typical microstrip antennas, the mutual conductance obtained using (3.28) is small compared to the self conductance G_1 of (3.28) or (3.17).

As shown by Equations (3.28) and (3.26), the input resistance is not strongly dependent upon the substrate height h. In fact for very small values of h, such that $k_0 h \ll 1$, the input resistance is not dependent on h. Modal-expansion analysis confirms that the input resistance is not strongly influenced by the substrate height h. It is apparent from (3.28) and (3.26) that the resonant input resistance can be decreased by increasing the width W of the patch. This is acceptable as long as the ratio of W/L does not exceed 2 because the aperture efficiency of a single patch begins to drop as W/L increases beyond 2.

The resonant input resistance, as calculated by (3.26), is referenced at slot #1. However, it has been shown that the resonant input resistance can be changed by using an inset feed, recessed a distance y_0 from slot #1, as shown in Figure 3.10(a). This technique can be used effectively to match the patch antenna using a microstrip-line feed whose characteristic impedance is given by [4]

$$Z_c = \begin{cases} \frac{60}{\sqrt{\epsilon_{r\_eff}}} \ln\left[\frac{8h}{W_0} + \frac{W_0}{4h}\right] & \frac{W_0}{h} \leq 1 \\ \frac{120\pi}{\sqrt{\epsilon_{r\_eff}}\left[\frac{W_0}{h} + 1.393 + 0.667 \ln\left(\frac{W_0}{h} + 1.444\right)\right]} & \frac{W_0}{h} > 1 \end{cases} ,$$

where W_0 is the width of the microstrip line, as shown in Figure 3.10(a). Using modal expansion analysis, the input resistance for the inset feed is

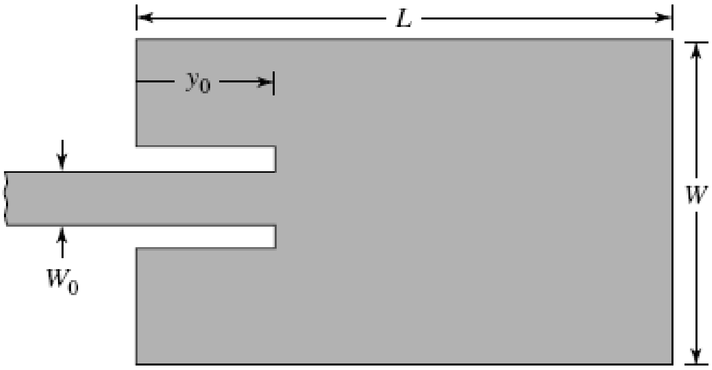

(a) Recessed microstrip-line feed

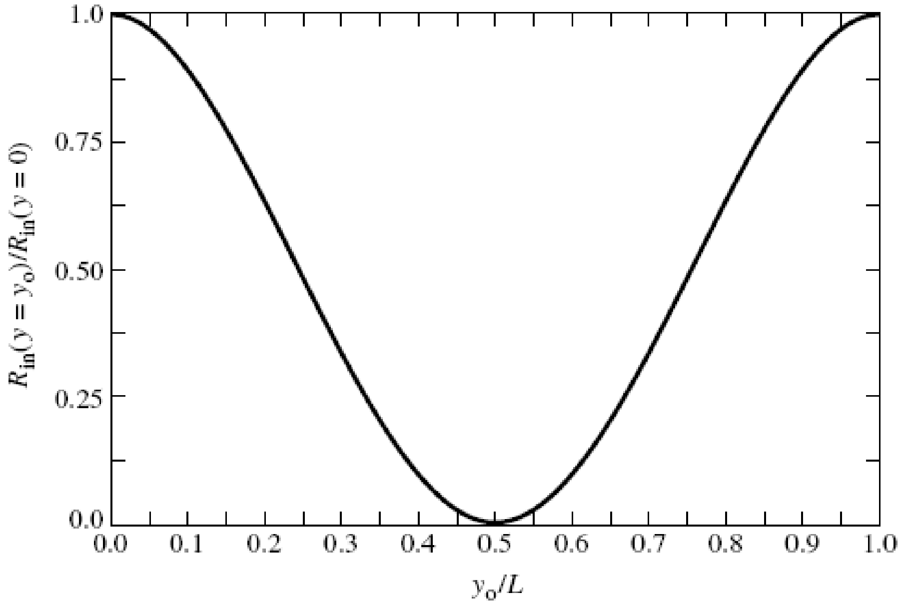

(b) Normalized input resistance

Figure 3.10: Recessed microstrip-line feed and variation of normalized input resistance.

given approximately by [18], [12]:

$$R_{in}(y = y_0) = \frac{1}{2(G_1 \pm G_{12})}\left[\cos^2\left(\frac{\pi}{L}y_0\right) + \frac{G_1^2 + B_1^2}{Y_c^2}\sin^2\left(\frac{\pi}{L}y_0\right) - \frac{B_1}{Y_c}\sin\left(\frac{2\pi}{L}y_0\right)\right] \tag{3.29}$$

where $Y_c = 1/Z_c$. Since for most typical microstrips $G_1/Y_c \ll 1$ and $B_1/Y_c \ll 1$, (3.29) reduces to

$$\begin{aligned} R_{in}(y = y_0) &= \frac{1}{2(G_1 \pm G_{12})}\cos^2\left(\frac{\pi}{L}y_0\right) = \\ &= R_{in}(y = 0)\cos^2\left(\frac{\pi}{L}y_0\right) \end{aligned} \tag{3.30}$$

A plot of the normalized value of 3.30 is shown in Figure 3.10(b).

The values obtained using (3.30) agree fairly well with experimental data. However, the inset feed introduces a physical notch, which in turn introduces a junction capacitance. The physical notch and its corresponding junction capacitance slightly influence the resonance frequency, which typically may vary by about 1%. It is apparent from (3.30) and Figure 3.10(b) that the maximum value occurs at the edge of the slot ($y_0 = 0$) where the voltage is maximum and the current is minimum; typical values are in the 150÷300 ohms range. The minimum value (zero) occurs at the center of the patch ($y_0 = L/2$) where the voltage is zero and the current is maximum. As the inset feed point moves from the edge toward the center of the patch the resonant input impedance decreases monotonically and reaches zero at the center. When the inset feed point approaches the center of the patch ($y_0 = L/2$), the $\cos^2(\pi y_0/L)$ function varies very rapidly; therefore the input resistance also changes rapidly with the position of the feed point. To maintain very accurate values, a close tolerance must be preserved.

3.2.2 Cavity Model

Microstrip antennas resemble dielectric-loaded cavities and exhibit higher order resonances. The normalized fields within the dielectric substrate (between the patch and the ground plane) can be found more accurately by treating that region as a cavity bounded by electric conductors (above and below it) and by magnetic walls (to simulate an open circuit) along the perimeter of the patch. This is an approximate model, which in principle leads to a reactive input impedance (of zero or infinite value at resonance), and does not radiate any power. However, assuming that the actual fields approximate those generated by such a model, the computed pattern, input admittance, and resonant frequencies compare well with measurements [47], [12], [65]. This is an accepted approach and is similar to the perturbation methods which have been very successful in the analysis of waveguides, cavities and radiators [29].

To shed some insight into the cavity model, a physical interpretation about the formation of the fields within the cavity and radiation through its side walls will be explained. When the microstrip patch is energized, a charge distribution is established on the upper and lower surfaces of the patch, as well as on the surface of the ground plane, as shown in Figure 3.11. The charge distribution is controlled by two mechanisms; an attractive and a repulsive mechanism [64]. The attractive mechanism is between the corresponding opposite charges on the bottom side of the patch and the ground plane, which tends to maintain the charge concentration on the bottom of the patch. The repulsive mechanism is between like charges on the bottom surface of the patch, which tends to push some charges from the bottom of the patch, around its edges, to its top surface. The movement of these charges creates corresponding current densities $\mathbf{J}_b$ and $\mathbf{J}_t$, at the bottom and top surfaces of the patch, respectively, as shown in Figure 3.11. Since for most practical microstrips the height-to-width ratio is very small, the attractive mechanism dominates and most of the charge concentration and current flow remain underneath the patch. A small amount of current flows around the edges of the patch to its top surface. However, this current flow decreases as the height-to-width ratio decreases. In the limit, when h/W tends to zero, the current flow to the top would be zero, which ideally would not create any tangential magnetic field components to the edges of the patch. This would allow the four side walls to be modeled as perfect magnetic conducting surfaces which ideally would not disturb the magnetic field and, in turn, the electric field distributions beneath the patch. Since in practice there is a finite height-to-width ratio, although small, the tangential magnetic fields at the edges would not be exactly zero. However, since they will be small, a good approximation to the cavity model is to treat the side walls as perfectly magnetic conductors. This model produces good normalized electric and magnetic field distributions (modes) beneath the patch. If the microstrip antenna were treated only as a cavity, it would not be sufficient to find the absolute amplitudes of the electric and magnetic fields. In fact by treating the walls of the cavity, as well as the material within it, as lossless, the cavity would not radiate and its input impedance

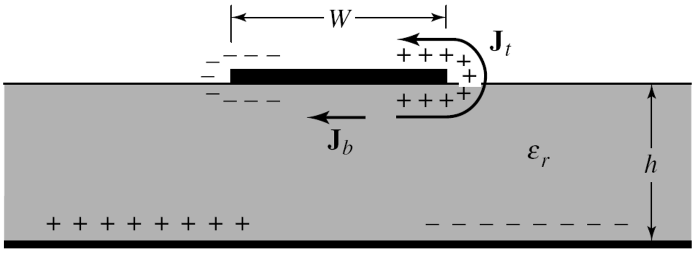

Figure 3.11: Charge distribution and current density creation on microstrip patch.

would be purely reactive. Also, the function representing the impedance would only have real poles. To make the microstrip lossy using the cavity model, which would then represent an antenna, the loss is taken into account by introducing an effective loss tangent δ_{eff}. The effective loss tangent is chosen appropriately to represent the loss mechanism of the cavity, which now behaves as an antenna, and is assumed as the reciprocal of the antenna quality factor Q ($\delta_{eff} = 1/Q$).

As the thickness of the microstrip is usually very small, the waves generated within the dielectric substrate (between the patch and the ground plane) undergo considerable reflections when they arrive at the edge of the patch. Therefore only a small fraction of the incident energy is radiated; thus the antenna is considered to be very inefficient. The fields beneath the patch form standing waves that can be represented by cosinusoidal wave functions. Since the height of the substrate is very small ($h \ll \lambda$ where λ is the wavelength within the dielectric), the field along the height will be considered constant. In addition, because of the very small substrate height, the fringing of the fields along the edges of the patch are also very small whereby the electric field is nearly normal to the surface of the patch. Therefore only TM^x, along x field configurations, will be considered within the cavity. While the top and bottom walls of the cavity are perfectly electric conducting, the four side walls will be modeled as perfectly conducting magnetic walls (tangential magnetic fields vanish along those four walls).

Field Configurations (*modes*)

– TM^x

The field configurations within the cavity can be found using the vector potential approach described in detail in [4]. Referring to Figure 3.12, the volume beneath the patch can be treated as a rectangular cavity loaded with a dielectric material having permittivity ϵ_r. The dielectric material of the substrate is assumed to be truncated and not extended beyond the edges of the patch. The vector potential A_x must satisfy the homogeneous wave equation of:

$$\nabla^2 A_x + k^2 A_x = 0 \tag{3.31}$$

$$A_x = [A_1 \cos(k_x x) + B_1 \sin(k_x x)] \cdot [A_2 \cos(k_y y) + B_2 \sin(k_y y)] \cdot [A_3 \cos(k_z z) + B_3 \sin(k_z z)] \tag{3.32}$$

where k_x, k_y and k_z are the wave numbers along the x, y, and z directions, respectively. These will be determined taking into account the boundary conditions. The electric and magnetic fields within the cavity are related to the vector potential A_x by [4]

$$\begin{aligned}
E_x &= -j\frac{1}{\omega\mu\epsilon}\left(\frac{\partial^2}{\partial x^2} + k^2\right)A_x & H_x &= 0 \\
E_y &= -j\frac{1}{\omega\mu\epsilon}\frac{\partial^2 A_x}{\partial x \partial y} & H_y &= \frac{1}{\mu}\frac{\partial A_x}{\partial z} \\
E_z &= -j\frac{1}{\omega\mu\epsilon}\frac{\partial^2 A_x}{\partial x \partial z} & H_z &= \frac{1}{\mu}\frac{\partial A_x}{\partial y}
\end{aligned} \tag{3.33}$$

subject to the boundary conditions of

$$\begin{gathered}
E_y(x' = 0,\ 0 \le y' \le L,\ 0 \le z' \le W) = \\
= E_y(x' = h,\ 0 \le y' \le L,\ 0 \le z' \le W) = 0 \\
H_y(0 \le x' \le h,\ 0 \le y' \le L,\ z' = 0) = \\
= H_y(0 \le x' \le h,\ 0 \le y' \le L,\ z' = W) = 0 \\
H_z(0 \le x' \le h,\ y' = 0,\ 0 \le z' \le W) = \\
= H_z(0 \le x' \le h,\ y' = L,\ 0 \le z' \le W) = 0
\end{gathered} \tag{3.34}$$

The coordinates x', y', z' are used to represent the fields within the cavity.

Applying the boundary conditions:

$$E_y(x' = 0,\ 0 \le y' \le L,\ 0 \le z' \le W) = 0\ ,$$

$$E_y(x' = h,\ 0 \le y' \le L,\ 0 \le z' \le W) = 0\ ,$$

it can be shown that $B_1 = 0$ and

$$k_x = \frac{m\pi}{h},\ m = 0, 1, 2, ... \tag{3.35}$$

Similarly, applying the boundary conditions:

$$H_y(0 \le x' \le h,\ 0 \le y' \le L,\ z' = 0) = 0\ ,$$

$$H_y(0 \le x' \le h,\ 0 \le y' \le L,\ z' = W) = 0\ ,$$

it can be shown that $B_3 = 0$ and

$$k_z = \frac{p\pi}{W},\ p = 0, 1, 2, ... \tag{3.36}$$

Finally, applying the boundary conditions $H_z(0 \le x' \le h,\ y' = 0,\ 0 \le z' \le W) = 0$ and $H_z(0 \le x' \le h,\ y' = L,\ 0 \le z' \le W) = 0$, it can be shown that $B_2 = 0$ and

$$k_y = \frac{n\pi}{L},\ n = 0, 1, 2, ... \tag{3.37}$$

Thus the final form for the vector potential A_x within the cavity is

$$A_x = A_{mnp} \cos(k_x x') \cos(k_y y') \cos(k_z z') \qquad , \tag{3.38}$$

where A_{mnp} represents the amplitude coefficients of each mnp mode. The wavenumbers k_x, k_y, k_z are equal to

$$m = n = p \neq 0 \begin{cases} k_x = \left(\frac{m\pi}{h}\right), & m = 0, 1, 2.... \\ k_y = \left(\frac{n\pi}{L}\right), & n = 0, 1, 2.... \\ k_z = \left(\frac{p\pi}{W}\right), & p = 0, 1, 2.... \end{cases}$$

where $m,\ n,\ p$ represent, respectively, the number of half-cycle field variations along the x, y, z directions.

Since the wavenumbers k_x, k_y, and k_z are related by the Equation (3.39)

$$k_x^2 + k_y^2 + k_z^2 = \left(\frac{m\pi}{h}\right)^2 + \left(\frac{n\pi}{L}\right)^2 + \left(\frac{p\pi}{W}\right)^2 = k_r^2 = \omega_r^2 \mu \epsilon \tag{3.39}$$

the resonant frequecies for the cavity are given by

$$(f_r)_{mnp} = \frac{1}{2\pi\sqrt{\mu\epsilon}} \sqrt{\left(\frac{m\pi}{h}\right)^2 + \left(\frac{n\pi}{L}\right)^2 + \left(\frac{p\pi}{W}\right)^2} \tag{3.40}$$

Substituting Equation (3.38) into (3.33), the electric and magnetic fields within the cavity are written as:

$$E_x = -j\frac{(k_r^2 - k_x^2)}{\omega\mu\epsilon} A_{mnp} \cos(k_x x') \cos(k_y y') \cos(k_z z')$$

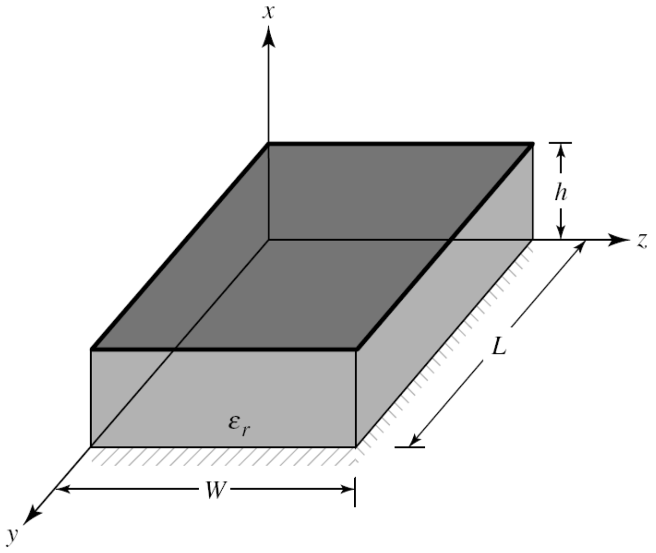

Figure 3.12: Rectangular microstrip patch geometry.

$$\begin{aligned}
E_y &= -j\frac{k_x k_y}{\omega\mu\epsilon}A_{mnp}\sin(k_x x')\sin(k_y y')\cos(k_z z')\\
E_z &= -j\frac{k_x k_z}{\omega\mu\epsilon}A_{mnp}\sin(k_x x')\cos(k_y y')\sin(k_z z')\\
H_x &= 0\\
H_y &= -\frac{k_z}{\mu}A_{mnp}\cos(k_x x')\cos(k_y y')\sin(k_z z')\\
H_z &= -\frac{k_y}{\mu}A_{mnp}\cos(k_x x')\sin(k_y y')\cos(k_z z')\ .
\end{aligned} \tag{3.41}$$

To determine the dominant mode with the lowest resonance, we need to examine the resonant frequencies. The mode with the lowest order resonant frequency is referred to as the *dominant* mode. Placing the resonant frequencies in ascending order, one determines the order of the modes of operation. For all microstrip antennas $h \ll L$ and $h \ll W$. If $L > W > h$, the mode with the lowest frequency (dominant mode) is the TM^x_{010} whose resonant frequency is given by

$$(f_r)_{010} = \frac{1}{2L\sqrt{\mu\epsilon}} = \frac{v_0}{2L\sqrt{\epsilon_r}}\ , \tag{3.42}$$

where v_0 is the velocity of light in free-space. If in addition $L > W > L/2 > h$, the next higher order (second) mode is the TM^x_{001} whose resonant frequency is given by

$$(f_r)_{001} = \frac{1}{2W\sqrt{\mu\epsilon}} = \frac{v_0}{2W\sqrt{\epsilon_r}}\ . \tag{3.43}$$

If, however, $L > L/2 > W > h$, the second order mode is the TM^x_{020}, instead of the TM^x_{001}, whose resonant frequency is given by

$$(f_r)_{020} = \frac{1}{L\sqrt{\mu\epsilon}} = \frac{v_0}{L\sqrt{\epsilon_r}} \,. \tag{3.44}$$

If $W > L > h$, the dominant mode is the TM^x_{001}whose resonant frequency is given by Equation (3.43), while if $W > W/2 > L > h$ the second order mode is the TM^x_{002}. Figure 3.13 shows the distributions of the tangential electric field along the side walls of the cavity for the TM^x_{010}, TM^x_{001}, TM^x_{020} and TM^x_{002} respectively as derived from Equations (3.41). In the above discussion, it was assumed that there is no fringing of the fields along the edges of the cavity. This is not completely valid, but it is a good approximation. However, fringing effects and their influence were discussed previously and they should be taken into account in determining the resonant frequency. This was done in Equation (3.6) for the dominant TM^x_{010} mode.

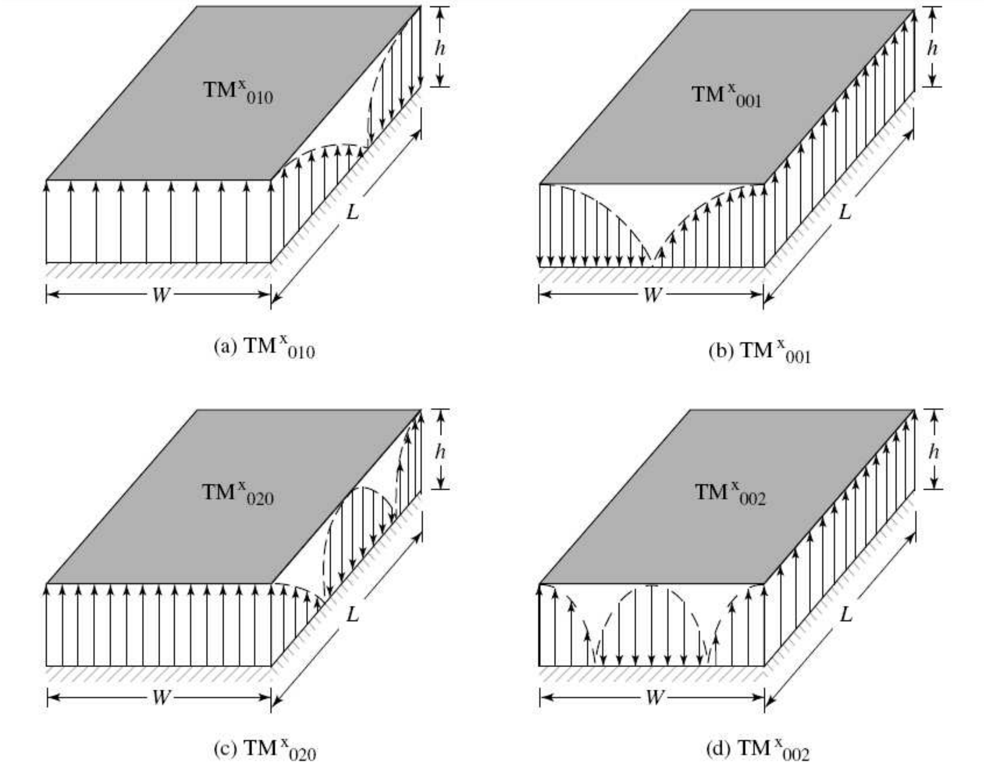

(a) TM^x_{010} (b) TM^x_{001}

(c) TM^x_{020} (d) TM^x_{002}

Figure 3.13: Field configurations (modes) for rectangular microstrip patch.

Equivalent Current Densities

It has been shown using the cavity model that the microstrip antenna can be modeled reasonably well by a dielectric-loaded cavity with two perfectly conducting electric walls (top and bottom) and four perfectly conducting magnetic walls (sidewalls). It is assumed that the material of the substrate is truncated and does not extend beyond the edges of the patch. The four sidewalls represent four narrow apertures (slots) through which radiation takes place. Using the Field Equivalence Principle (Huygens Principle), the microstrip patch is represented by an equivalent electric current density, $\mathbf{J}_t$, at the top surface of the patch to account for the presence of the patch (there is also a current density, $\mathbf{J}_b$, at the bottom of the patch which is not needed for this model). The four side slots are represented by the equivalent electric current density, $\mathbf{J}_s$, and equivalent magnetic current density, $\mathbf{M}_s$, as shown in Figure 3.14(a), expressed by:

$$\mathbf{J}_s = \hat{\mathbf{n}} \times \mathbf{H}_a \tag{3.45}$$

and

$$\mathbf{M}_s = -\hat{\mathbf{n}} \times \mathbf{E}_a \tag{3.46}$$

where $\mathbf{E}_a$ and $\mathbf{H}_a$ represent, respectively, the electric and magnetic fields in the slots.

As it was shown for microstrip antennas with very small height-to-width ratio that the current density $\mathbf{J}_t$ at the top of the patch is much smaller than the current density $\mathbf{J}_b$ at the bottom of the patch, it will be assumed negligible here and will be set to zero. Also it was argued that the tangential magnetic fields along the edges of the patch are very small, ideally zero. Therefore the corresponding equivalent electric current density $\mathbf{J}_s$ will be very small (ideally zero) and will be set to zero here. Thus the only nonzero current density is the equivalent magnetic current density $\mathbf{M}_s$ (3.46) along the side periphery of the cavity radiating in the presence of the ground plane, as shown in Figure 3.14(b). The presence of the ground plane can be taken into account by image theory which will double the equivalent magnetic current density of (3.46). Therefore the final equivalent quantity is a magnetic current density of twice (3.46) or

$$\mathbf{M}_s = -2\hat{\mathbf{n}} \times \mathbf{E}_a \tag{3.47}$$

around the side periphery of the patch radiating into free space, as shown in Figure 3.14(c)

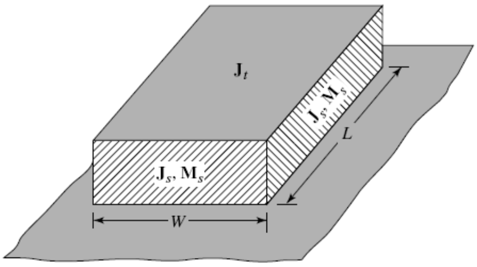

(a) $\mathbf{J}_s, \mathbf{M}_s$ with ground plane

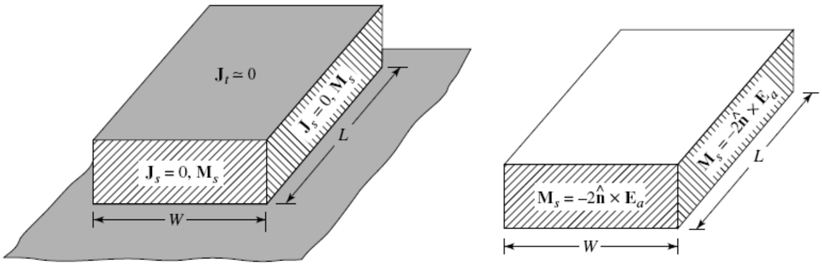

(b) $\mathbf{J}_s = 0$, $\mathbf{M}_s$ with ground plane

(c) $\mathbf{M}_s$ with no ground plane

Figure 3.14: Equivalent current densities on four sides of rectangular microstrip patch.

It was shown, using the transmission-line model, that the microstrip antenna can be represented by two radiating slots along the length of the patch (each of width W and height h). Similarly it will be shown here also that while there are a total of four slots representing the microstrip antenna, only two (the radiating slots) account for most of the radiation; the fields radiated by the other two, which are separated by the width W of the patch, cancel along the principal planes. Therefore the former two slots, separated by the length of the patch, are referred to here also as *radiating slots*. The slots are separated by a very low-impedance parallel-plate transmission line of length L, which acts as a transformer. The length of the transmission line is approximately $\lambda/2$, where λ is the guide wavelength in the substrate, in order to have opposite polarization for the fields at the aperture of the two slots. This is illustrated in Figures 3.1(a) and 3.14(a). The two slots form a two-element array with a spacing of $\lambda/2$ between the elements. It will be shown here that in a direction perpendicular to the ground plane the components of the field add in phase and give a maximum radiation normal to the patch; thus the antenna is of a broadside type. Assuming that the dominant mode within the cavity is the TM^x_{010} mode, the electric and magnetic field components reduce from (3.41) to

$$\begin{aligned} E_x &= E_0 \cos\left(\frac{\pi}{L} y'\right) \\ H_z &= H_0 \sin\left(\frac{\pi}{L} y'\right) \\ E_y &= E_z = H_x = H_y = 0 \end{aligned} \tag{3.48}$$

where $E_0 = -j\omega A_{010}$ and $H_0 = (\pi/\mu L)A_{010}$. The electric field structure within the substrate and between the radiating element and the ground plane is sketched in Figures 3.1(a,b) and 3.14(a). It undergoes a phase reversal along the length but it is uniform along its width. The phase reversal along the length is necessary for the antenna to have broadside radiation characteristics.

Using the equivalence principle, each slot radiates the same fields as a magnetic dipole with current density $\mathbf{M}_s$ (3.47). By referring to Figures 3.15 the equivalent magnetic current densities along the two slots, each of width W and height h, are both of the same magnitude and of the same phase. Therefore these two slots form a two-element array with the sources (current densities) of the same magnitude and phase, and separated by L. Thus these two sources will add in a direction normal to the patch and ground plane forming a broadside pattern. This is illustrated in Figures 3.16(a) where the normalized radiation pattern of each slot in the principal E-plane is sketched individually along with the total pattern of the two. In the H-plane, the normalized pattern of each slot and of the two together is the same, as shown in Figure 3.16(b).

The equivalent current densities for the other two slots, each of length L and height h, are shown in Figure 3.17. Since the current densities on each wall are of the same magnitude but of opposite direction, the fields radiated by these two slots cancel each other in the principal H-plane. Also since corresponding slots on opposite walls are 180° out of phase, the corresponding radiations cancel each other in the principal E-plane. The radiation from these two side walls in non principal planes is small compared to the other two side walls. Therefore these two slots are usually referred to as *non radiating slots*.

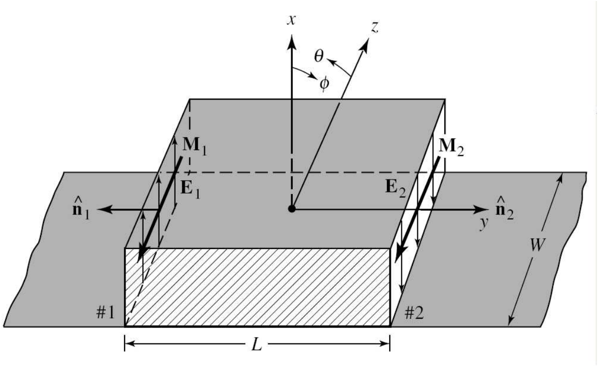

Figure 3.15: Rectangular microstrip patch radiating slots and equivalent magnetic current densities.

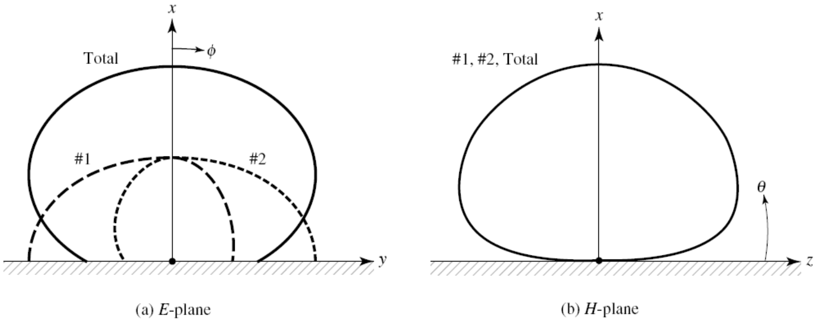

(a) *E*-plane

(b) *H*-plane

Figure 3.16: Typical E- and H-plane patterns of each microstrip patch slot, and of the two together.

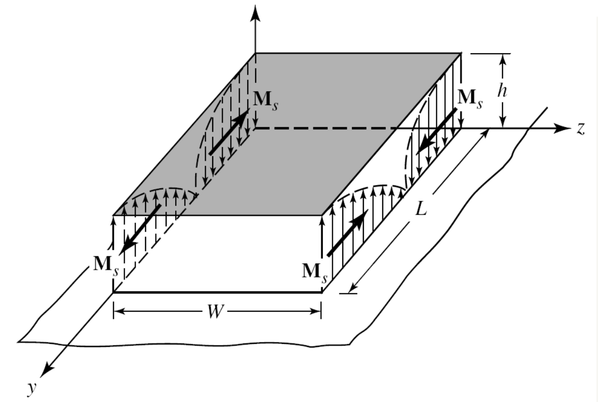

Figure 3.17: Current densities on non radiating slots of rectangular microstrip patch.

3.2.3 Full Wave Model

As mentioned in § 3.2 the last of the well known models used to design a microstrip antenna consists in using a full wave model. The knowledge of the phase delay related to every element is of primary importance in a reflectarray design as shown in [59]. In this work the necessary phase shift at each element is obtained by varying the resonant side of every element and its correct dimension comes from software CST - Micro Wave Studio [17] after a fine comparison with the one obtained by HFSS [37]. Both CST-MWS and HFSS are specialist tools for 3D EM simulations of high frequency components. The former solves Maxwell equations using a ″finite integral technique″ in the time and frequency domain. The latter implements a ″finite elements method″ in the frequency domain instead. To design every single element, the reflectarray can be approximate as an infinite periodical array of identical elements (elementary cells).

CST Micro Wave Studio

As a full wave analysis method, the Finite-Difference Time-Domain (FDTD) method plays an important role in the microstrip antenna design. However, its major drawback is that it requires a large amount of computer time and storage. It is very important to improve the efficiency of the method. Recently, H. Lee and J. Kim have developed a novel FDTD method to model periodic structures. Thanks to the use of Floquet's theorem, the simulation domain is restricted from full structure to one unit, so the computational time and memory are reduced. The pattern reconfigurable antenna is a periodic structure; the use of FDTD method combined with Floquet's theorem can also lead to the reduction of the computational time and memory. It should be noted that CST-MWS makes possible to use the *unit-cell* approach (as illustrated in Figure 3.18) supported by the *Floquet's* theorem [55] formulation to model the scattered field and employ a transmission-line approach to relate the linear polarized normally incident plane wave with the scattered radiation. The phase delay of the field is given in terms of phase of a reflection coefficient. The Floquet theory is a branch of the theory of ordinary differential equations relating to the class of solutions to linear differential equations of the form:

$$\dot{x} = A(t)x \tag{3.49}$$

where $A(t)$ is a continuous periodic function with period T (see [22]). The Floquet theorem and the unit cell approach allow to study the behaviour of the electric field due to a single antenna in a periodic structure as compared with the electric field product to the whole array.

HFSS

In HFSS, to build a procedure to calculate the reflection coefficient, two pairs of opposite perfect electric and magnetic walls are used and the whole structure is considered as a Transverse Electro-Magnetic (TEM) waveguide terminated by an elementary cell as shown in Figure 3.19. The cell works as a complex load with negligible real part and imaginary part dependent on resonant side. In consequence, the amplitude of reflection coefficient is close to 1 whereas the phase will depend on dimension of resonant side.

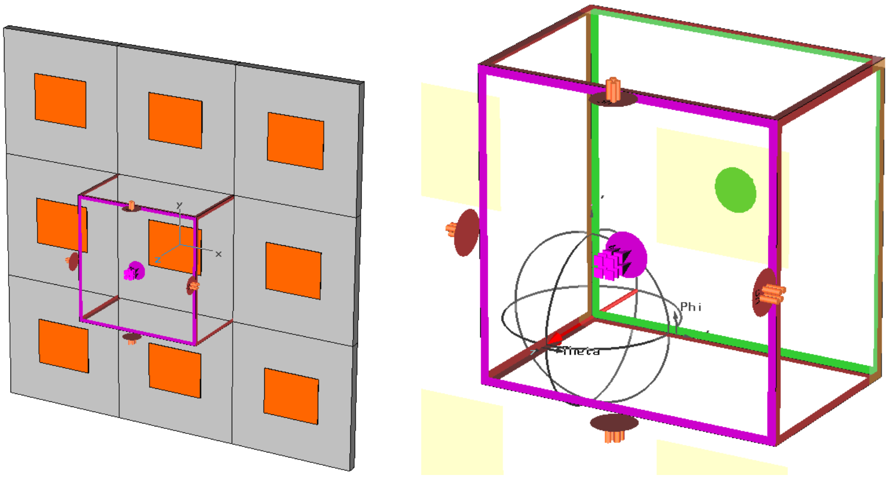

Figure 3.18: Infinite periodic array modeled with "Unit cell" in CST-MWS.

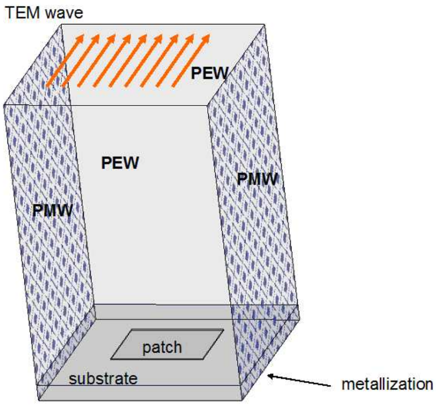

Figure 3.19: Infinite periodic array modeled with a TEM waveguide in HFSS.

Chapter 4

Reflectarray Antenna

The reflectarray antenna consists of a flat or slightly curved reflecting surface and an illuminating feed, as shown in Figure 4.1. On the reflecting surface, there are many isolated elements (e.g., open-ended waveguides, printed patches, dipoles, or rings) without any power division transmission lines. The feed antenna illuminates these isolated elements, which are designed to scatter the incident field with electrical phases, which are required to form a planar phase front in the far-field distance. This operation is similar in concept to the use of a parabolic reflector that naturally reflects and forms a planar phase front when a feed is placed at its focal point. Thus the term ″flat reflector″ is sometimes used to describe the reflectarray, which utilizes technologies of both reflector and array.

In this chapter the concept of the reflectarray antenna will be introduced and a detailed analysis of the design procedures will be presented.

As shown in Figure 4.2, there are several methods for reflectarray elements to achieve a planar phase front. For example, one is to use identical microstrip patches with different-length phase-delay lines attached to enable them to compensate for the phase delays over the different paths from the illuminating feed. Another method employs variable-size patches, dipoles, or rings to provide the elements with different scattering impedances and, thus, different phases to compensate for the different feed path delays. In the third method, for circular polarization only, the reflectarray has all identical circularly polarized elements but with different angular rotations to compensate for the feed path length differences. To achieve low reflecting surface profile and low antenna mass, reflectarrays using printed microstrip elements have been developed. These reflectarrays combine some of the best features of the traditional parabolic reflector antenna and the microstrip array technology. Similar to a parabolic reflector, the reflectarray can achieve very good efficiency (> 50%) for very large aperture since no power divider is needed and thus very little resistive insertion loss is encountered here.

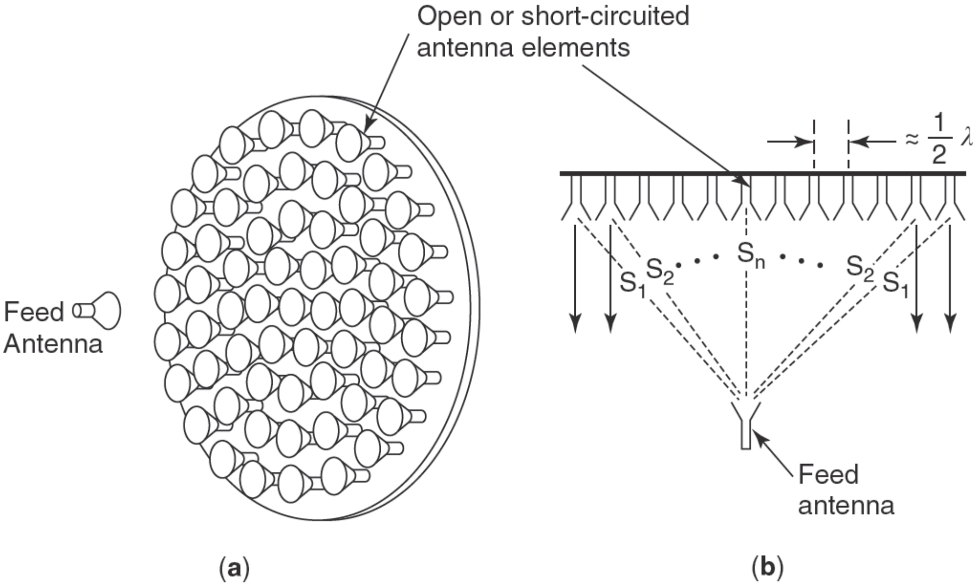

Figure 4.1: Configuration of a reflectarray antenna: three- (a) and two-dimensional (b) views.

On the other hand, very similar to an array antenna, the reflectarray can have its main beam designed to tilt at a large angle (> 50°) from its broadside direction. Low-loss electronic phase shifters can be implanted into the elements for wide-angle electronic beam scanning. With this beam-scanning capability of the reflectarray, the complicated high-loss beam forming network and high-cost transmit/receive (T/R) amplifier modules of a conventional phased array are no longer needed. One significant advantage of the printed reflectarray is that it is easy to use and versatile. When a large aperture (e.g., 10-m) spacecraft antenna requires a deployment mechanism, the flat structure of the reflectarray allows a much simpler and more reliable folding or inflation mechanism than does the curved surface of a parabolic reflector. The flat reflecting surface of the reflectarray also lends itself for flush mounting onto an existing flat structure without adding significant mass and volume to the overall system structure. The reflectarray, which is in the form of a printed microstrip antenna, can be fabricated with a simple and low-cost etching process. Another major feature of the reflectarray is that, with more than hundreds or thousands of elements in a general reflectarray having phase adjustment capability, it can achieve very accurate contour beam shape with a phase synthesis technique.

With all these capabilities, there is one distinct disadvantage associated with the reflectarray antenna. This is its inherent narrow bandwidth, which generally cannot exceed much beyond 10%. This narrow bandwidth behavior is discussed further in §4.3.

Although the reflectarray has narrow bandwidth, due to its multitude of capabilities, the development, research, and application of the printed reflectarray antenna seem to be potentially boundless in the future.

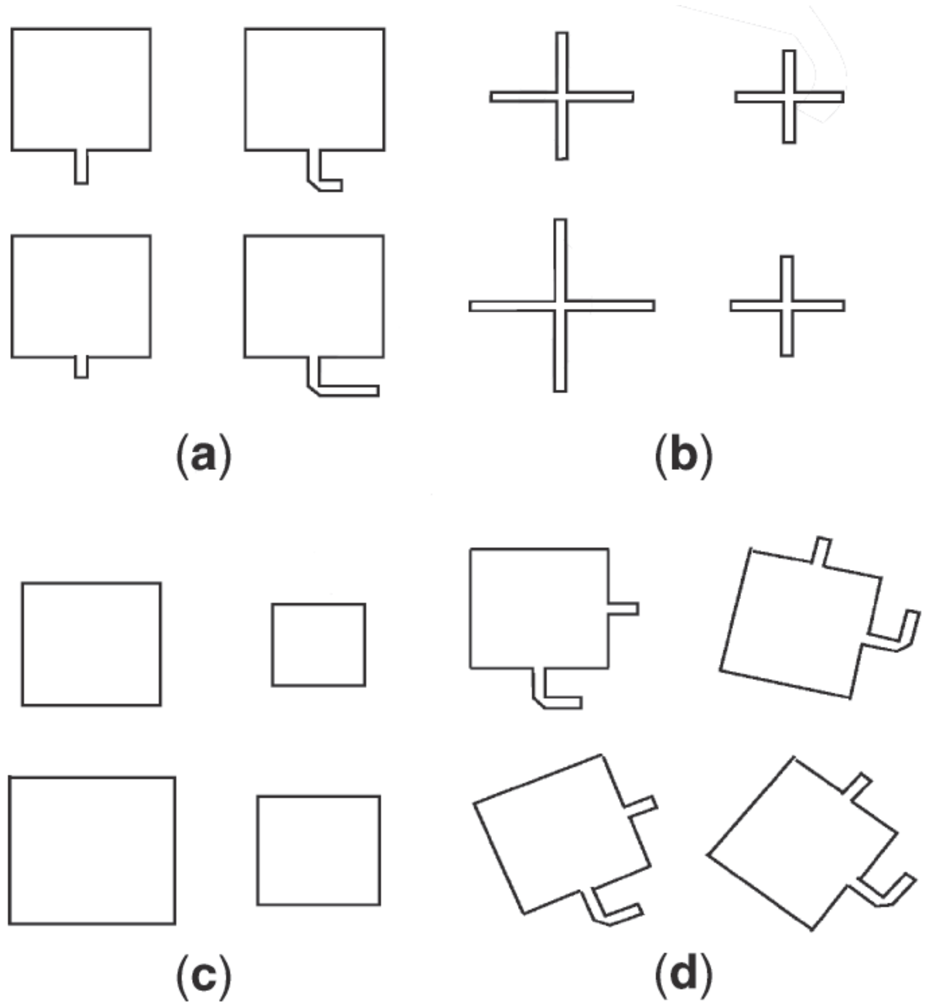

Figure 4.2: Various reflectarray elements: (a) identical patches with variable-length phase delay lines; (b) variable-size dipoles; (c) variable-size patches; (d) variable angular rotations.

4.1 Review of development history

The reflectarray antenna concept, shown in Figure 4.1, was first demonstrated during the early 1960s [7]. Open-ended waveguide elements with variable-length waveguides were used to demonstrate the capability of achieving cophasal reradiated far-field beams. During this early time, since most wireless operations were done at relatively low microwave frequencies, the large-waveguide reflectarrays resulted in very bulky and heavy antennas. In addition, the efficiencies of these reflectarrays were not studied and optimized.

More than 10 years later (in the mid-1970s), the very ingenious concept of ″spiraphase″ reflectarray was developed [54], where switching diodes were used in an eight-arm spiral or dipole element of a circularly polarized reflectarray to electronically scan its main beam to large angles from the broadside direction. This is possible because, by angularly rotating a circularly polarized radiating element, its propagating electrical phase will also change by an appropriate amount proportional to the amount of rotation. However, because of the thick spiral cavity and large electronic components, the spiraphase reflectarray was still relatively bulky and heavy. Its aperture efficiency was still relatively poor. Thus, no continued development effort was followed.

It should be noted here that, in order to ensure good efficiency for the reflectarray, the antenna must be well designed taking into account the intricate relations between the element beamwidth, element spacing, and focal length/diameter (f/D) ratio; otherwise, a large backscattered component field or a mismatched surface impedance would result.

Following the introduction of the printable microstrip antennas, the technologies of reflectarray and microstrip radiators were combined. A typical resulting configuration is illustrated in Figure 4.3. Various printed microstrip reflectarray antennas were developed in the late 1980s and early 1990s for the purpose of achieving reduced antenna size and mass. These printed reflectarrays came in various forms as shown in Figure 4.2 and all flat low-profile and low-mass reflecting surfaces. The ones using identical patch elements with different-length phase-delay lines [51] - [13] have elements similar to those shown in Figure 4.2a. The phase-delay lines, having lengths in the order of half-wavelength or less, are used to compensate for the phase differences of different pathlengths from the illuminating feed. A

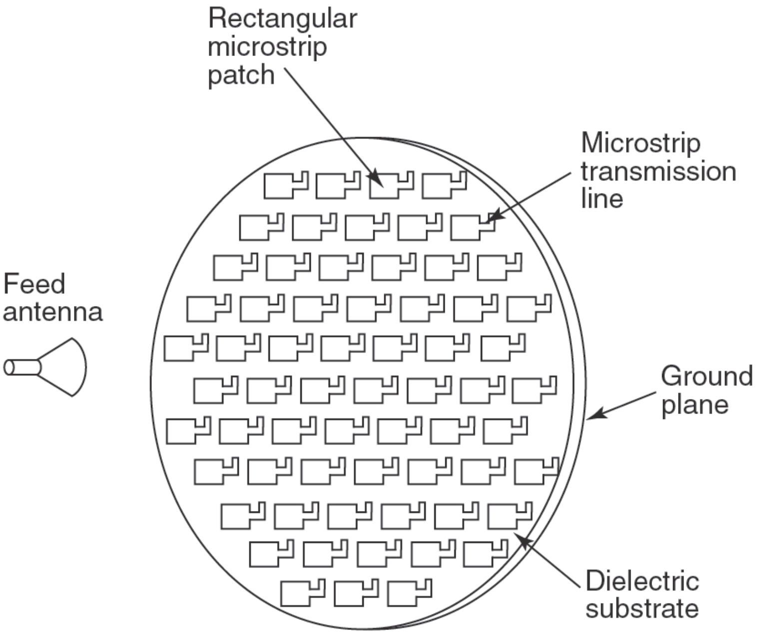

Figure 4.3: Microstrip reflectarray with identical patches but different-length phase delay lines.

second approach, shown in Figure 4.2b, used elements that are made of printed dipoles with variable dipole lengths [42]. Different dipole lengths will yield different scattering impedances, which then provide the different phases needed to compensate for the different pathlength delays. Similarly, microstrip patches with variable patch sizes [57], shown in Figure 4.2c, were also developed. Circularly polarized microstrip patches with identical size but variable angular rotations [34, 36], shown in Figure 4.2d, were designed to form a cophasal far field reflectarray beam. In addition to those shown in Figure 4.2, several other reflectarray or equivalent antennas developed during the 1990's are worth mentioning here. Printed variable-length dipole elements were used to form a frequency scanned grating-reflector antenna with an offset feed [40]. Printed annular rings of variable diameters arranged in Fresnel-zone configuration were also used to focus the beam [23]. In the 1996 Phased Array Conference, a 94- GHz monolithic reflectarray [16], using one-bit pin (positive-intrinsic–negative) diode phase shifters, was reported to achieve wide-angle (±45°) electronic beam scanning. In the same conference, a 35-GHz reflectarray, using waveguide and dielectric elements with 3-bit ferrite phase shifters [72], was also reported to achieve ±25° beam scanning. One technique proposed [34], although not yet developed, is worth mentioning here. By using the angular rotation technique with circularly polarized elements, miniature or micromachined motors could be placed under each element to achieve wide-angle beam scanning without the need of appropriate T/R modules and phase shifters. For application in the spacecraft area, a deployable and low-mass one-meter diameter inflatable reflectarray antenna [31] at the X-band frequency (8÷12 GHz) was developed. Another unique spacecraft application of the reflectarray was conceived [35] and developed [58] by using its many elements, with a numerical phase synthesis technique, to form a uniquely shaped contour beam. From all these achievements, it can be seen that, at the end of twentieth century, reflectarray antenna technology has reached a state of complete development and has had a variety of possible applications throughout the microwave and millimeter-wave spectra.

In early 2000, the development of mushroomed reflectarray and several performance improvement techniques are worth mentioning here. One used multilayer stacked patches to improve the reflectarray bandwidth from a few percent to more than 10% [21]. As an extension to the 1-m X-band inflatable reflectarray mentioned above, a 3-m Ka-band inflatable reflectarray consisting of 200000 elements was also developed [33], which is currently known as the "electrically largest reflectarray". An amplifying reflectarray was developed [9], each element of which amplified the transmitted signal, thus, achieving very high overall radiated power. In order to achieve good antenna efficiency, the most critical segment of the reflectarray design is its elements. The element performance was optimized by using the genetic algorithm (GA) method [80]. A reflectarray using subreflector and array feed configuration to achieve fine beam scanning was also studied [43]. To combat the shortcomings of narrow-bandwidth, dual-band multilayer reflectarrays using annular rings [27] and crossed dipoles [79] are also being developed. Another development that is worth mentioning here is a folded reflectarray configuration [50], where two reflecting surfaces are used to reduce the dimensions of the overall antenna profile due to the feed height in the case of a conventional reflectarray.

4.2 Analysis and design procedures

The design and analysis of a reflectarray can be separated into four essential steps, which are discussed separately below.

4.2.1 Element characterization

The most important and critical aspect of the reflectarray design is its element characterization. If the element design is not optimized, it will not scatter the signal from the feed effectively to form an efficient far-field beam. Its beamwidth must be properly correlated with the reflectarray's f/D ratio to accommodate all incident angles from the feed. Its phase change versus element change (patch size, delay line length, etc.) must be calibrated correctly. One very popular technique for calibrating the phase is to use the infinite-array approach [57, 59] to include local mutual coupling effect due to surrounding elements. It is not feasible with the current computer technology to have a complete rigorous solution to include all the mutual coupling effects of all elements since the reflectarray generally consists of too many elements. The infinite array approach can be followed by using the method-of-moment technique [57, 59] or, equivalently, by a finite-difference time-domain (FDTD) analysis on a unit cell of a single element [24]. Mathematical waveguide simulation, which simulates the infinite-array approach, can also be adopted by using the commercial software HFSS (high-frequency structure simulator; a finite-element technique) to achieve the element phase information. All these techniques are used to derive the phase-versus-element-change curve, which is generally an ″S″-shaped curve expressing a nonlinear relationship, as illustrated in Figure 4.4. The antenna designer should minimize the slope at the center of the curve to ensure that the phase change will not be excessively sensitive to the element change. If the curve is too steep, the element change or fabrication tolerance may become an issue, in particular at high microwave frequencies.

4.2.2 Required Phase Delay

The pathlengths from the feed to all elements are all different, and this variation leads to different phase delays. To compensate for these, the elements must have corresponding phase advancements designed according to a unique ″S″ curve similar to that shown in Figure 4.4. The following two equations give examples of how the compensating phase is calculated for each element of a reflectarray with a broadside-directed beam. The differential pathlength for each element is given as

$$\Delta L_{m,n} = L_{m,n} - L_{0,0} \ , \tag{4.1}$$

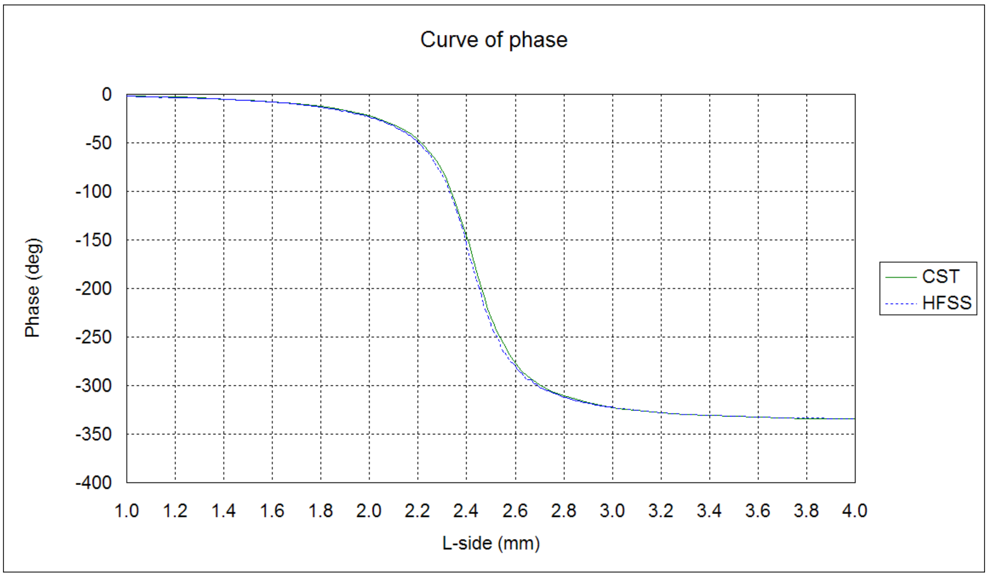

Figure 4.4: Curves of phase obtained with different software.

where $L_{m,n}$ is the distance between the feed and the mnth element, which can be obtained by using simple geometry and $L_{0,0}$ is the distance between the feed and a reference point on the reflectarray surface, such as the center point. $\Delta L_{m,n}$ thus represents the differential feed pathlength for the mnth element. To achieve a collimated radiation, the phase advancement $\Delta\Phi_{m,n}$ needed for the mnth element is given by

$$\Delta\Phi_{m,n} = \frac{\Delta L_{m,n}}{\lambda_0} \tag{4.2}$$

where $\Delta\Phi_{m,n}$ is expressed in radiants and have a periodicity of 2π

4.2.3 Pattern Calculation

With all element's compensating phases known, the far-field radiation patterns can be calculated by the conventional array theory, where the radiation of all elements are summed together as follows. Consider a planar array consisting of $M \times N$ elements that are nonuniformly illuminated by a low-gain feed at position vector $\vec{r}_f$. Let the desired beam direction be specified by unit vector $\hat{u}_0$. Then the far-field of the reflectarray in the $\hat{u}$ direction will be of the form

$$E(\hat{u}) = \sum_{m=1}^{M}\sum_{n=1}^{N} F(\vec{r}_{mn}\cdot\vec{r}_f)\cdot A(\vec{r}_{mn}\cdot\hat{u}_0)\cdot A(\hat{u}\cdot\hat{u}_0)\cdot exp[jk(|\vec{r}_{mn}-\vec{r}_f|+\vec{r}_{mn}\cdot\hat{u})+j\alpha_{mn}] \tag{4.3}$$

where F is the feed pattern function, A is the reflectarray element pattern function, $\vec{r}_{mn}$ is the position vector of the mnth element and a_{mn} is the required compensating phase of the *mn*th element calculated by Eq. 4.2. The $cos^q\theta$ factor is used for both F and A functions with no azimuth (ϕ) dependence.

4.2.4 Reflectarray Geometry Design

The determination of the geometry of a reflectarray basically consists in determining its f/D ratio, which is governed by its desired aperture efficiency. Equations (4.4) and (4.5) are used by assuming a circular aperture only for demonstration of the design procedures. The aperture efficiency (η_a) can be defined as the product of the illumination (η_I) and spillover (η_s) efficiencies: $\eta_a = \eta_I \times \eta_s$. By integrating the pattern function of Equation (4.3), the illumination efficiency for a center-fed reflectarray can be obtained in a closed form [32] as given by:

$$\eta_I = \frac{[((1-\cos^{q+1}\theta_e)/(q+1)) + ((1-\cos^{q}\theta_e)/q)]^2}{2\tan^2\theta_e[(1-\cos^{2q+1}\theta_e)/(2q+1)]} \tag{4.4}$$

and the spillover efficiency is given by:

$$\eta_s = 1 - \cos^{2q+1}\theta_e\ , \tag{4.5}$$

where q is the exponent of the feed pattern function represented by $\cos^q\theta$ and θ_e is half of the subtend angle from the feed to the reflectarray aperture. The reflectarray element is approximated by cosine function. Similar closed-form equations can be easily obtained for square, rectangular, or elliptical apertures by performing proper integrations. To give an example of how Equations (4.4) and (4.5) can be used to optimize a reflectarray design, Figure 4.5 shows the calculated curve of spillover and illumination efficiencies versus the feed pattern factor q (feed beamwidth) for a 0.212-m 35-GHz reflectarray with a fixed f/D ratio of 0.8 ($\theta_e \sim 35°$). It demonstrates that the maximum aperture efficiency is achieved at $q = 7.5$ corresponding to a feed with a -3dB beamwidth of ∼ 35° as shown in the left panel of Figure 4.6. Another curve, shown in the right panel of the Figure 4.6, gives aperture efficiency as a function of f/D ratio for the same 0.212-m 35-GHz reflectarray where the Edge Taper (ET) is of 13dB at 35°. In this case, the maximum aperture efficiency is achieved when the f/D ratio is ∼ 0.9. It can be seen that curves derived from Equations (4.4) and (4.5) are essential to obtain an optimum efficiency design. The above discussion has been limited to the center-fed reflectarray. Offset reflectarray can also be optimally designed by using equations similar to (4.4) and (4.5).

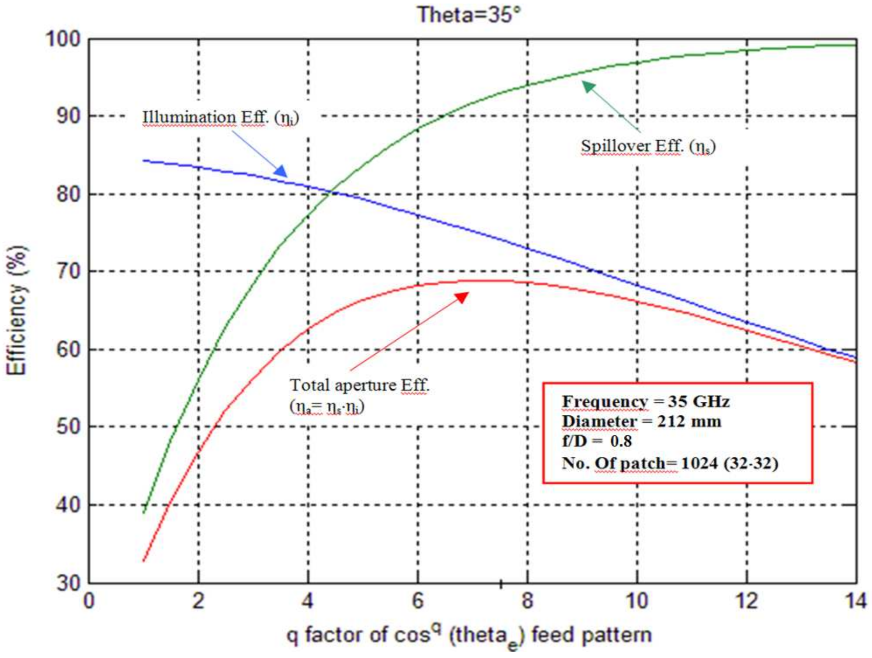

Figure 4.5: Spillover, illumination and total efficiencies versus feed pattern shape.

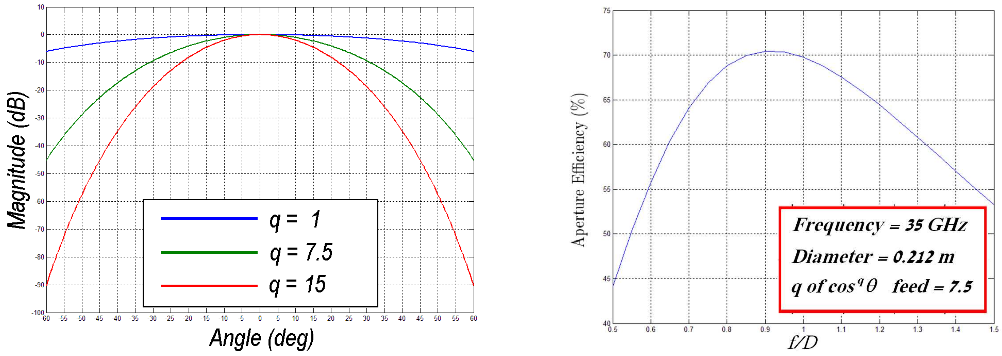

Figure 4.6: Left panel: $\cos^q$ feed horn pattern shape - right panel: aperture efficiency versus f/D ratio.

4.3 Bandwidth

The bandwidth performance of a reflectarray [34] is completely different from that of a parabolic reflector, where infinite bandwidth theoretically exists. The bandwidth of a printed microstrip reflectarray is limited primarily by two factors: (1) the narrow bandwidth of the microstrip patch elements on the reflectarray surface and (2) the differential spatial phase delay.

The microstrip patch element generally has a bandwidth of about 35%. To achieve wider bandwidth for a conventional microstrip array several techniques have been employed, such as the use of a thick substrate for the patch, the stack of multiple patches and the use of sequentially rotated subarray elements. More than 15% bandwidths have been reported.

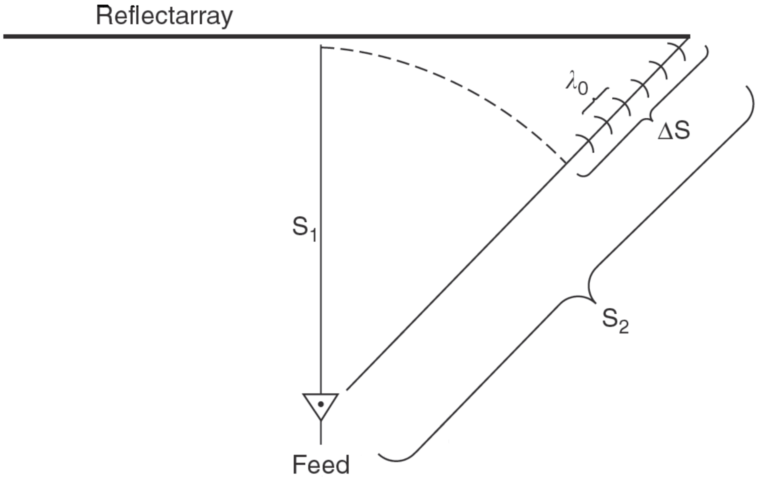

Figure 4.7: Differential spatial phase delay of reflectarray.

The second reflectarray limiting factor, the differential spatial phase delay, can be best explained by referring to Figure 4.7, where the differential spatial phase delay, ΔS, is represented by the phase difference between the two paths, S_1 and S_2, from the feed to the reflectarray elements. The value of ΔS can be equal to many multiples of the wavelength (λ) at the center operating frequency. It can be expressed as $\Delta S = (N + d)\lambda$, where N is an integer and d is a fractional number of a free-space wavelength (λ). At each element location, d is compensated by an appropriate phase delay achieved by the reflectarray element design (obtained by variable patch size, variable phase-delay line length, etc.). As frequency changes, the factor $(N + d)\lambda$ becomes $(N + d)(\lambda + \Delta\lambda)$. Since the design and the compensating phase for each element is fixed at the center frequency, a frequency excursion error will occur in the reradiated phase front. The amount of phase change in each path when compared to a reference path, say, S_1, is $(N + d)\Delta\lambda$, which can constitute a significant portion of a wavelength of 360°. To reduce the amount of frequency excursion error, the integer number N must be reduced. Several methods can be used to reduce N:

1. Design the reflectarray with a larger f/D ratio and hence minimize the difference between paths S_1 and S_2.

2. Simply avoid the use of a reflectarray with a large electrical diameter.

The effects of f/D ratio and diameter on bandwidth performance were given in Figure 4.5 and in the right panel of Figure 4.6.

3. Reduce frequency excursion error by using time-delay lines or partial time-delay lines instead of the phase delays. In other words, when using the phase-delay line technique (not the variable-patch-size technique), instead of using $d\Delta\lambda$ for the delay-line length, $(N + d)\Delta\lambda$ could be used. Certainly, additional line insertion loss and needed real estate for the lines are issues to be encountered.

4. Increase the bandwidth by using, instead of a complete flat reflectarray surface, a concavely curved reflectarray with piecewise flat surfaces. This curved reflectarray will remain advantageous over a curved parabolic reflector; for instance, its beam can be scanned to large angles with a phase shifter inserted into each element, and, for a space-deployable antenna, the piecewise flat surfaces in some cases can be folded more easily into a smaller stowed volume.

In order to mitigate the bandwidth problem, a recent technique of using multilayer stacked-patch elements [21] has not only increased the element bandwidth but also reduced the effect of differential spatial phase delay. As a net result, the bandwidth has increased from a few percent to more than 10%. Multi band techniques can also be applied to the reflectarray. Recently, two dual-band techniques have been developed for the X- and Ka-band frequencies: (1) use of a double layer with two different size rings and variable angular rotations [27] and (2) use of a double layer with X-band crossed dipoles over Ka-band patches [79].

To summarize, although the narrow bandwidth is the primary shortcoming of a reflectarray, several techniques can be employed to improve bandwidth performance.

4.4 Summary

The reflectarray antenna has come a long way. However, its development and application had not been widely adopted until the early 1990s, when the printable microstrip reflectarray was introduced. Except for its narrow bandwidth characteristic, the reflectarray has many advantages over a parabolic reflector antenna type. The main beam of a reflectarray can be designed to tilt to a large angle from its broadside direction. Phase shifters can be implanted into the elements for wide-angle electronic beam scanning.

For large-aperture spacecraft antenna applications, the reflectarrays flat surface allows the antenna to be realized as an inflatable structure with relative ease in maintaining its surface tolerance in comparison to a curved parabolic surface. Its flat surface also can be made of multiple flat panels for ease in folding into a more compact structure for launch vehicle stowage. Very accurate beam shape can be achieved with phase synthesis technique for Earth contour beam coverage applications. Due to these multitudes of capabilities, the door has just opened for the development, research, and application of printed reflectarray antennas. Two major areas that need further improvement in performance are the reflectarray's bandwidth and radiation efficiency.

Chapter 5

The Total Power Radiometer

When we are talking about Radiometry we intend all it is concerned with the measurement, analysis, and interpretation of radiant electromagnetic energy. The instrument used is the radiometer which allows to receive the electromagnetic power in a given frequency band. Some instruments, however, analyze the received energy's spectral distribution (spectroradiometers), its polarization (polarimeters), or its angular distribution in space (imaging radiometers). Radiometry uses the different dielectrical, chemical and physical properties of the materials according to the electromagnetic radiation that is emitted, reflected, or transmitted. Radiometry is therefore a branch of remote sensing and could be considered to include radar. In practice, however, the term radiometry is usually used to describe the measurement and characterization of naturally occurring radiation, or (unlike radar) scattered radiation originating as a narrow-band signal. The former, called passive radiometry, deals principally with self-emitted thermal radiation and reflected radiation of solar origin. The latter, called active radiometry, relies on artificial illumination. Figure 5.1 illustrates these different types of radiometers. Active radiometers are sometimes called scatterometers.

Since all radiometers depend for their operation on the measurement of one or more parameters of electromagnetic radiation, a brief review of such electromagnetic radiation will follow, the principal radiometric quantities will be defined and the blackbody radiation and its emissivity will be described.

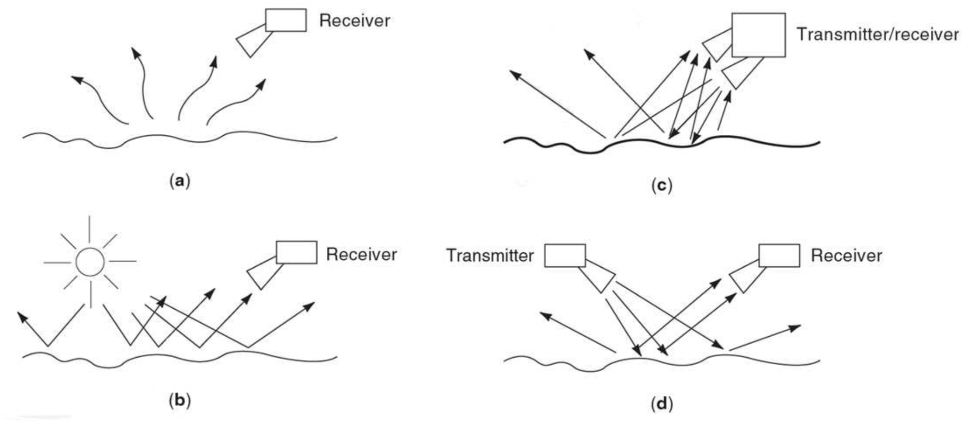

Figure 5.1: Passive and active radiometry: (a) passive measurements of self-emitted thermal radiation; (b) passive measurements of scattered solar radiation; (c) active (scatterometer) measurements employing monostatic geometry; (d) active (scatterometer) measurements employing bistatic geometry.

5.1 Electromagnetic radiation

Whenever charges accelerate (other than those carried by electrons in stable orbits around the nuclei of atoms), or a subatomic particle in an atom makes a transition to a lower energy level, electromagnetic energy is radiated. This energy propagates as a disturbance of the electric and magnetic fields existing in space. An electromagnetic wave propagating in an isotropic, homogeneous medium has, sufficiently far from its source, an electric field vector **E**, magnetic field vector **B**, and unit vector pointing in the direction of wave propagation **u**, which are mutually perpendicular. Furthermore, the wavefront has a curvature that is sufficiently small for it to be considered locally plane. (In a truly uniform plane wave **E** and **B** would be constant with respect to position in any plane normal to the direction of propagation.)

For radiation of a single frequency (said to be *monochromatic*), **E** and **B** will vary sinusoidally with time and space. The amplitude (A) of such a wave is the peak value of its electric field strength, and its cyclical frequency f is the number of oscillations (or cycles) that the electric field completes, at a given point in space, per second. [The angular frequency ω is the phase advance in radians, at a given point in space, that the wave makes in one second and is related to cyclical frequency by $\omega = 2\pi f$]. The phase constant β is the phase advance in radians that the wave makes, at a given instant of time, over one meter of space in the direction of propagation and is related to wavelength λ by $\beta = 2\pi/\lambda$. ($1/\lambda$ and β are therefore the spatial equivalent of cyclical and angular frequency, respectively.)

Non monochromatic radiation has an amplitude at a point in space that fluctuates over time as the phase relationships between the constituent (and elemental) monochromatic waves change. The timescale over which this amplitude fluctuation occurs is related to the bandwidth Δf of the radiation and is characterized by a coherence time. For an electromagnetic wave, coherence time is the time over which a propagating wave may be considered coherent. In other words, it is the time interval within which its phase is, on average, predictable. In long-distance transmission systems, the coherence time may be reduced by propagation factors such as dispersion, scattering and diffraction. Coherence time, Δt, is calculated by dividing the coherence length by the phase velocity of light in a medium; approximately given by $\Delta t = \lambda^2/(c\Delta\lambda)$ where λ is the central wavelength of the source, $\Delta\lambda$ is the spectral width of the source, and c is the velocity of light in vacuum.

If the tip of the **E** vector, representing a wave at a single point in space, traces out an elliptical curve, the wave is said to be (fully) polarized. If the curve traced out is random, the wave is said to be unpolarized. A wave with an **E** vector locus that can be resolved into a deterministic component and a random component is said to be partially polarized. A fully polarized wave having a polarization ellipse with an axial ratio of 1.0 or ∞ is said to be circularly or linearly polarized, respectively. A linearly polarized wave is therefore defined as a transverse electromagnetic wave whose electric field vector (at a point in an isotropic medium) at all times lies along a fixed line.

The concepts of coherence and polarization are not entirely related since a wave observed on a timescale that is short with respect to its coherence time is always fully polarized. As the observation time increases, the polarization of the wave may gradually change; however, the changes appear random on a timescale large with respect to the waves coherence time. A wave will remain fully polarized even when observed on a timescale much longer than its coherence time if energy is radiated in one polarization only.

In passive radiometry the received electromagnetic radiation is usually non coherent, spread across a wide band of frequencies, and unpolarized. The useful measurable quantities in this case are the power density (W/m^2), the radiation intensity (W/sr), the power spectral density (W/Hz), and the angular/spatial radiation distribution. In radiometry the first three of these quantities are generally referred to as irradiance (E), radiant intensity (I), and radiant spectral flux (Φ_f), respectively.

5.2 Definition of radiometric quantities

The commonly used radiometric quantities are as follows:

- Radiant energy Q (J) the quantity of electromagnetic energy in a specified region of space or associated with a specified process
- Radiant flux Φ (W) radiant energy per unit time crossing a specified surface
- Radiant density w (J/m^3) radiant energy per unit volume
- Radiant flux density E or M (W/m^2) radiant flux per unit area normal to a specified direction
- Irradiance E (W/m^2) radiant flux density arriving at a specified surface
- Radiant excitance (or emittance) M (W/m^2) radiant flux density leaving a specified surface
- Radiant intensity I (W/sr) radiant flux per unit solid angle in a specified direction
- Radiance L ($Wsr^{-1}m^{-2}$) radiant intensity in a specified direction per unit projected area of the source normal to the specified direction

Radiation consisting of electromagnetic power distributed over a continuum of frequencies has infinitesimally small power at any single frequency. Each of the preceding quantities can be characterized at a single frequency, however, by considering the quantity to be measured within a small bandwidth Δf (centered on frequency f), dividing by Δf, and taking the limit as $\Delta \rightarrow 0$. The result is a spectral density having those units of the original quantity per Hertz. (An obvious variation on this definition uses angular frequency instead of cyclical frequency.) At optical frequencies spectral densities are usually expressed as quantities per meter of wavelength rather than per hertz of frequency. A spectral density is typically indicated by preceding the quantity with the word *spectral* and adding a subscript f, ω, or l to the appropriate symbol. Spectral irradiance, for example, can be expressed in any of the following ways:

$$E_f(f) = \lim_{\Delta f \rightarrow 0} \left[\frac{P_{\Delta f}}{\Delta f} \right] \tag{5.1}$$

$$E_\omega(\omega) = \lim_{\Delta\omega \to 0} \left[\frac{P_{\Delta\omega}}{\Delta\omega} \right] \tag{5.2}$$

$$E_\lambda(\lambda) = \lim_{\Delta\lambda \to 0} \left[\frac{P_{\Delta\lambda}}{\Delta\lambda} \right] \tag{5.3}$$

where:

$P_{\Delta f}$ is the power density contained in frequency band $(f - \frac{\delta_f}{2})$ to $(f + \frac{\Delta_f}{2})$;
$P_{\Delta\omega}$ is the power density contained in frequency band $(\omega - \frac{\delta_\omega}{2})$ to $(\omega + \frac{\Delta_\omega}{2})$;
$P_{\Delta\lambda}$ is the power density contained in frequency band $(\lambda - \frac{\delta_\lambda}{2})$ to $(\lambda + \frac{\Delta_\lambda}{2})$.

The relationship between these various expressions is summarized by

$$E_f(f) = \frac{E_\omega(\omega)}{2\pi} = E_\lambda\!\left(\frac{c}{\lambda}\right)\frac{c}{f^2} \tag{5.4}$$

Spectral densities may be a function of frequency and, if so, may be measured by a spectroradiometer to yield information about the source of the radiation, material through which it has passed, or a surface from which it has been reflected. When spectral densities are constant with frequency (at least over the frequency band of interest) they are referred to as white and are characterized by a single value.

5.3 Blackbody radiation and emissivity

A body that absorbs all electromagnetic radiation falling into (converting the incident radiant energy to thermal energy) is called a blackbody. Such a body, in thermal equilibrium with its surroundings, must supply precisely as much energy back to, as it receives from, these surroundings. In the absence of conduction and convection the energy transfer mechanism is limited to thermal radiation. The thermal radiant energy emitted by a body can never, therefore, be greater than that emitted by a blackbody of the same size, shape, and physical temperature. The degree of blackness of a body is quantified by its surface emissivity, defined as follows.

Emissivity (e) is defined as the ratio between the spectral radiant excitance at the surface of a body to the spectral radiant excitance at the surface of a blackbody with the same physical temperature.

The maximum value of emissivity, corresponding to that of a blackbody, is therefore unity and the minimum value, corresponding to a surface that reflects all radiant energy falling on it, is zero. A body with an emissivity that is independent of frequency, but less than unity, is called a graybody.

Many natural materials have emissivities that are frequency-dependent, however, and this dependence, if measured radiometrically, can yield useful information about the material's composition and physical state.

The reflecting, transmitting, and absorbing properties of a material's surface, which can also be inferred from radiometric measurements, are quantified as follows:

- Reflectance, ρ-ratio of reflected to incident spectral radiant flux at a surface.
- Transmittance, τ-ratio of transmitted to incident spectral radiant flux at a surface.
- Absorptance, α-ratio of absorbed to incident spectral radiant flux at a surface.

It is clear that:

$$\rho + \tau + \alpha = 1 \tag{5.5}$$

The surface of a blackbody has an absorptance of unity and, therefore, a reflectance and transmittance of zero. More generally, for any opaque ($\tau = 0$) material, $\rho = 1 - \alpha$ and emissivity is numerically equal to absorptance (i.e., $\epsilon = \alpha$).

A good model of a blackbody is the surface represented by a small hole drilled in a hollow cavity. Provided that the reflectance of the interior surface of the cavity is not too close to unity, then any radiant energy falling on to the hole is reflected a sufficient number of times inside the cavity for it to be fully absorbed before it can reemerge.

The spectral radiant excitance $M_f(f)$ of a blackbody (Figure 5.2), is given by Planck's law [74]:

$$M_f(f) = \frac{2\pi h}{c^2} \frac{f^3}{exp(hf/kT) - 1} \tag{5.6}$$

For optical frequencies, where it is traditional to express spectral quantities on a per meter of wavelength, rather than a per Hertz of frequency, Equation 5.6 can be written as:

$$M_f(f) = \frac{2\pi hc^2}{\lambda^5} \frac{1}{exp(hc/\lambda kT) - 1} \tag{5.7}$$

For $hf \ll kT$, which is appropriate for microwave radiometry at all commonly encountered temperatures, (5.6) reduces to the Rayleigh-Jeans approximation (Figure 5.3):

$$M_f(f) = \frac{2\pi}{c^2} kTf^2 \tag{5.8}$$

[The Rayleigh-Jeans version of (5.7) is $M_\lambda(\lambda) = 2\pi ckT/\lambda^4$.] The spectral radiant excitance of a body with emissivity < 1.0 is therefore given by:

$$M_f(f) = \epsilon(f)\frac{2\pi}{c^2} kTf^2 \tag{5.9}$$

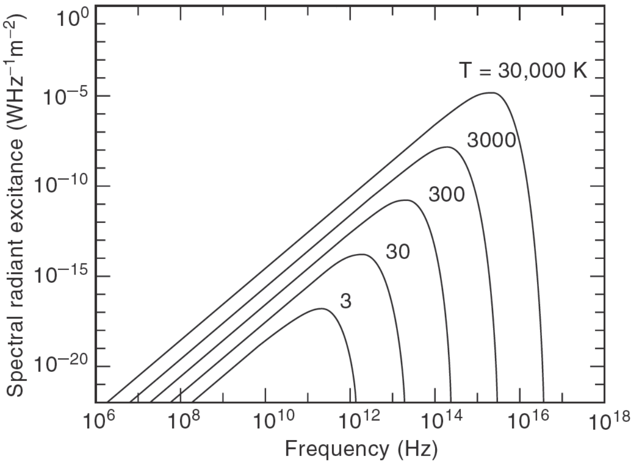

Figure 5.2: Planck's law for blackbody radiation.

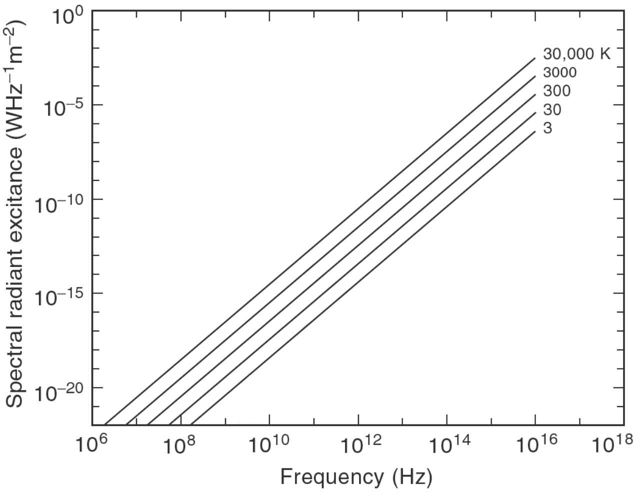

Figure 5.3: Rayleigh-Jeans approximation for blackbody radiation.

5.3.1 Lambert's Law and Lambertian Radiators

Lambert's cosine law states that the radiant intensity from a blackbody surface is proportional to $\cos\psi$, where ψ is the angle between the direction of observation and the surface normal. Any surface (irrespective of its emissivity) that has this distribution of radiant intensity is said to be *Lambertian*. The radiance of such a surface is independent of ψ. The spectral radiant excitance of an arbitrary surface is related to its spectral radiance by

$$M_f(f) = \int_0^{2\pi} \int_0^{\pi/2} L_f(\psi, f) \cos\psi \sin\psi d\psi d\gamma \tag{5.10}$$

which, for a Lambertian surface, reduces to:

$$M_f(f) = L_f(f)\pi \tag{5.11}$$

The spectral radiance of a blackbody surface is therefore given by:

$$L_f(f) = \frac{2h}{c^2} \frac{f^3}{exp(hf/kT) - 1} \tag{5.12}$$

which for $kT \gg hf$ gives the Rayleigh–Jeans approximation:

$$L_f(f) = \frac{2kT}{c^2} f^2 = \frac{2kT}{\lambda^2} \tag{5.13}$$

5.3.2 Radiometric Brightness and Antenna Temperatures

Consider a lossless antenna (i.e., one having an ohmic efficiency of 100%) with effective aperture area $A_e(\theta, \phi)$ receiving radiant energy from a surface S (Figure 5.4). If a surface element of area dS lies at a distance R from the antenna in the direction (θ, ϕ), then the spectral radiant flux density arriving at the antenna due to this element is:

$$dE_f = \frac{I_f(\theta, \phi)}{R^2} = \frac{L_f(\theta, \phi) dS \cos\psi}{R^2} \tag{5.14}$$

The power spectral density (or spectral radiant flux) received by the antenna is therefore:

$$d\Phi_f = 0.5 A_e(\theta, \phi) dE_f = \frac{0.5 A_e(\theta, \phi) L_f(\theta, \phi) dS \cos\psi}{R^2} \tag{5.15}$$

(The factor of 0.5 accounts for the fact that the antenna will be polarization-matched to only half of the randomly polarized incident energy.) The quantity $dS(\cos\psi)/R^2$ in Equation (5.15) can be identified as the solid angle $d\Omega$ subtended by the surface element at the antenna (Figure 5.5). The power

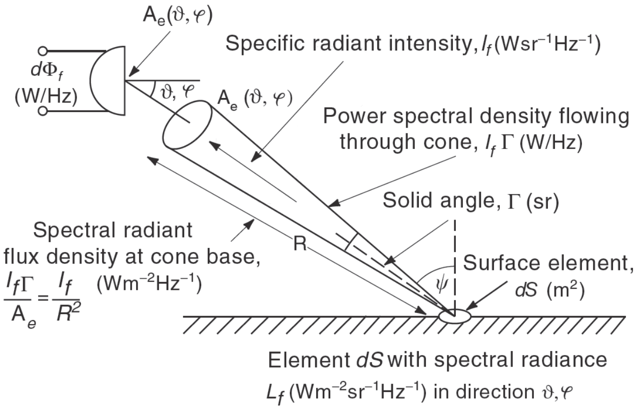

Figure 5.4: Spectral irradiance at radiometer antenna aperture due to radiating surface element *dS*.

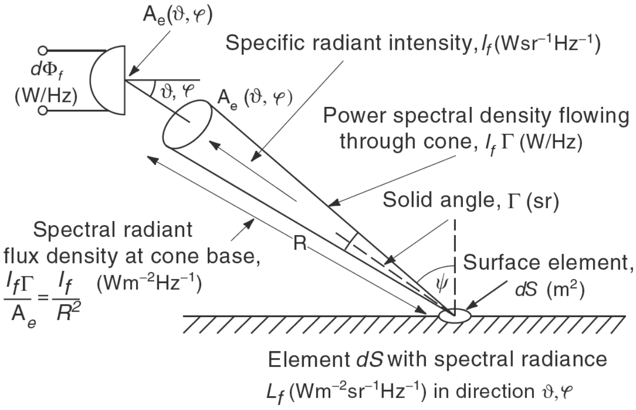

Figure 5.5: Solid angle subtended at radiometer antenna aperture by radiating surface element dS.

spectral density available at the antenna output terminals can therefore be expressed as either a surface, or a solid angle, integral:

$$\Phi_f = 0.5 \int_S \int \frac{A_e(\theta,\phi)L_f(\theta,\phi)\cos\psi dS}{R^2} = \int_\Omega \int A_e(\theta,\phi)L_f(\theta,\phi)d\Omega \;. \quad (5.16)$$

The power, or radiant flux, received within a band of frequencies f_{min} to f_{max} is then given by:

$$\Phi = \int_{f_{min}}^{f_{max}} \Phi_f(f)\, df \;. \quad (5.17)$$

Since Equation (5.16) is a power spectral density, an antenna aperture temperature T_a may be defined such that the noise power measured by a noiseless radiometer (i.e., one that has a noise figure of 0 dB), with a lossless antenna, is kT_aB_N (where B_N is the radiometer noise bandwidth and k is Boltzmann's constant). For small B_N, such that $\Phi_f(f)$ can be considered white, $T_a = \Phi/kB_N = \Phi_f/k$ and

$$T_a = \frac{0.5}{k} \int_\Omega \int A_e(\theta,\phi)L_f(\theta,\phi)d\Omega \quad (5.18)$$

In a lossless antenna, effective area is related to antenna directivity by $A_e(\theta,\phi) = D(\theta,\phi)\lambda^2/4\pi$ [70], where $D(\theta,\phi)$ is the antenna directivity pattern. Equation (5.18) may therefore be written as:

$$T_a = \frac{0.5}{k}\frac{\lambda^2}{4\pi} \int_\Omega \int D(\theta,\phi)L_f(\theta,\phi)d\Omega \quad (5.19)$$

The quantity $(0.5\lambda^2/k)L_f(\theta,\phi)$ is usually referred to as a radiometric brightness temperature $T_B(\theta,\phi)$. The Equation (5.19) can be written as:

$$T_a = \frac{1}{4\pi} \int_\Omega \int D(\theta,\phi)T_B(\theta,\phi)d\Omega \;. \quad (5.20)$$

(In microwave radiometry the term brightness is often used as a synonym for spectral radiance.) The radiometric brightness temperature of a body is related to the body's physical temperature T by the body's emissivity:

$$T_B(\theta,\phi) = \epsilon(\theta,\phi)T(\theta,\phi) \quad (5.21)$$

[The emissivity's dependence on ψ is not shown explicitly in Equation (5.21) but is implied in its θ,ϕ dependence. The frequency dependence is suppressed only for clarity.] The first step in conventional radiometer data analysis usually requires that the radiometric brightness temperature of a particular region be estimated from a measurement of an antenna noise temperature T_A, defined by

$$T_A = \frac{\Phi_R}{kB_N} \tag{5.22}$$

where Φ_R is the power supplied to the radiometer by the antenna. If the antenna has nonzero ohmic loss, the measured antenna noise temperature will comprise an attenuated aperture temperature (the aperture temperature is the temperature measured by a lossless antenna) and a thermal contribution from the physical antenna structure itself. For an antenna with ohmic (or radiation) efficiency η_Ω (expressed as a per unit, not percent, quantity) and physical structure temperature T_s the measured antenna noise temperature will be:

$$T_A = \eta_\Omega T_a + (1 - \eta_\Omega)T_s \tag{5.23}$$

If the antenna loss is sufficiently small, then $T_a \cong T_A$. Equation (5.18) shows, however, that the antenna aperture temperature is a weighted average of the observed brightness temperature, the weighting function being the antenna directivity pattern. If the antenna has a radiation pattern with low sidelobes and a beamwidth that is narrow with respect to the angular rate of change of brightness temperature, then T_a gives the required brightness temperature, in the direction of the mainlobe, directly. For an imaging radiometer (which scans a beam over some solid angle, e.g., to form an image), with a beam that is not sufficiently narrow, deconvolution of the antenna pattern from the resulting image may be necessary. Since antenna directivity and gain are related [70] by $G(\theta, \phi) = \eta_\Omega D(\theta, \phi)$, then Equations (5.20) and (5.23) can be combined and written as:

$$T_A = \frac{1}{4\pi} \int_{4\pi}\!\!\int G(\theta, \phi) T_B(\theta, \phi) d\Omega + (1 - \eta_\Omega)T_s \tag{5.24}$$

In the absence of significant atmospheric effects (losses and scattering), Equation (5.24) shows that an adequate knowledge of antenna ohmic efficiency and antenna gain pattern will allow the brightness temperature of a surface (with a spatial resolution determined by the antenna beamwidth) to be found from a measurement of antenna temperature. (The noise figure of the radiometer must be considered, of course, when making this measurement [69]).

5.3.3 Atmospheric Loss and Scattering

If atmospheric effects cannot be neglected, then the brightness temperature inferred from Equation (5.24) must be interpreted as an apparent brightness temperature since it will comprise a contribution from the target surface plus a contribution from the thermal emission of the atmosphere itself. Furthermore, the thermal radiation from each source (i.e., each surface element of the target and each volume element of the atmosphere) will be attenuated by the loss associated with the intervening atmosphere. Since atmospheric thermal emission is essentially isotropic, half of the thermal energy from each element is radiated upward (called *upwelling radiation*) and half is radiated downward (called *downwelling radiation*). For a downward-pointing radiometer (such as might be used in planetary surface remote sensing applications), downwelling radiation may be reflected by the ground back into the antenna's mainlobe. The contribution of this ground-scattered radiation will depend on the ground reflectance and the integrated specific attenuation along the ground-reflected path to the radiometer. An upward-pointing radiometer (such as might be used in terrestrial atmospheric remote sensing applications) observes downwelling radiation from the atmosphere directly. The contribution from ground-scattered downwelling radiation, and ground thermal emission, will now be coupled into the antenna through its downward-pointing sidelobes or backlobes. The significance of this radiation will depend on the gain of these lower hemisphere lobes and the brightness temperature of the region within the mainlobe of the antenna. (If a microwave radiometer with high antenna gain is pointed at high elevation angle into a clear sky, well away from any discrete sources of radiation, then the brightness temperature observed by its mainlobe may be as low as a few Kelvin degrees. Radiation emitted by, or reflected from, the ground may, under these conditions, be a very significant source of measurement error.)

The preceding description assumes that the atmosphere is an absorbing, but nonscattering, medium. For an atmosphere filled with scattering particles, or more general scattering inhomogeneities, this simplified description is inadequate. (The operating wavelength, and the physical size and composition of inhomogeneities, will determine whether they act as significant scatterers or not [5].) In this case more rigorous theories must be used to account for, and interpret, observed radiometric measurements [11].

5.3.4 Definition of Co- and Cross- polarization

The Co-polar and Cross-polar vectors are born from *3th Ludwig's Definitions* [48]. The mathematic expressions of Co-polar field $E_{co}(\theta,\varphi)$ and Cross-polar field $E_x(\theta,\varphi)$ in terms of components in spherical coordinates $E_\theta(\theta,\varphi)$ and $E_\varphi(\theta,\varphi)$ respectively are:

$$\begin{bmatrix} E_{co}(\theta,\varphi) \\ E_x(\theta,\varphi) \end{bmatrix} = \begin{bmatrix} \cos\varphi & -\sin\varphi \\ \sin\varphi & \cos\varphi \end{bmatrix} \begin{bmatrix} E_\theta(\theta,\varphi) \\ E_\varphi(\theta,\varphi) \end{bmatrix} \tag{5.25}$$

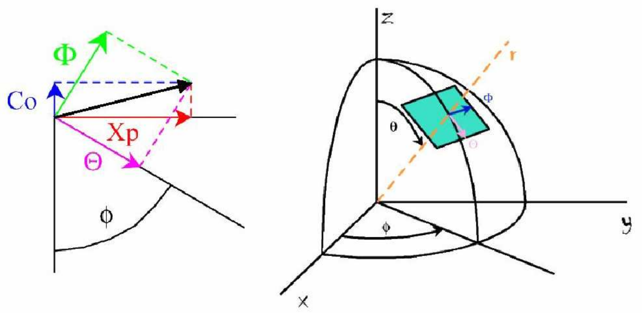

Figure 5.6: Vectors Θ and Φ are defined corresponding to $E_\theta(\theta,\varphi)$ and $E_\varphi(\theta,\varphi)$ from Equation (5.25).

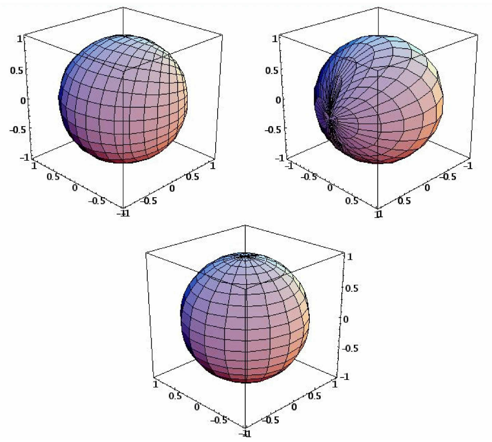

Figure 5.7: Representation of the co- and cross- polar components over a sphere.

XPD

The *Cross Polar Discrimination* (XPD) can be defined as the ratio between the maximum of the co-polar component to the maximum of the cross-polar component:

$$\text{XPD} = \frac{|E_{co}^{(max)}|^2}{|E_x^{(max)}|^2} \tag{5.26}$$

Chapter 6

The *ViKy* Project

The *ViKy* project was born as one of the possible technology transfer of PLANCK/LFI during my PhD thesis. Initially we focused our activity on the design of the radiometer in order to make the temperature resolution of the whole passive *ViKy* system possible. This requirement has been used to design all the other *ViKy's* components.

In this chapter I will present the results of the design of the principal *ViKy's* subsystems: horn, reflectarray, radiometer and motion control. For each subsystem the main requirements are introduced and the analysis to achieve them are described. In this chapter the principal innovative manufacturing processes are also explained.

6.1 The *ViKy's* Horn

The horn is one of the two principal components of the *ViKy* antenna system. It is used to illuminate the reflectarray in both the onset and offset configurations.

6.1.1 Requirements

The feed horn has been realized thanks to the knowledge matured during the PLANCK project.

A corrugated profile has been chosen to improve the performance in terms of pattern shape, taper and return loss. The frequency band has been chosen around the 20%, this value being a good compromise between manufacturing process and performance. The edge taper has been optimized to illuminate the edge of the reflectarray with a power of about $-13dB$ with respect to the incident power at the center of the array. This value allows to neglect the diffraction of the radiation incident on the border of the reflectarray. Table 6.1 shows the RF specifications of the feed-horn.

Object	Requirements
Horn type	Corrugated
Frequency band	32.5 ÷ 37.5 GHz
Taper	-10 dB 30° ($\pm 1dB$) at 35 GHz
Return loss	< - 25 dB in band
Losses	To be measured

Table 6.1: RF specifications of the feed-horn

6.1.2 Description of the design process

The design of the corrugated horn antenna has been initially conducted by using the FHAAP software, that performs a Mode Matching analysis that is specific for circular horn design. In a second step, the identified solution has been checked through a more accurate full-wave Electro Magnetic (EM) analysis of the device performed through CST Microwave Studio (MWS).

The result of the entire design process is a circular corrugated horn characterized by:

- 22.1 mm aperture,
- variable taper angle to better optimize the return loss,
- 13 corrugations.

Varying the width, the length and the number of corrugations it is possible to optimize the shape of the pattern or, in other words, the edge taper of the feed horn.

A sketch of the mechanical drawing of the feed-horn is given in Figure 6.1. The effective external dimensions of the feed-horn will be fixed during the fabrication, due to the peculiarity of the electroforming process.

6.1.3 Results of *FHAPP* simulations

In this section the theoretical results (Return Loss and radiation patterns) as obtained through *FHAPP* analysis and CST MWS analysis are presented and compared.

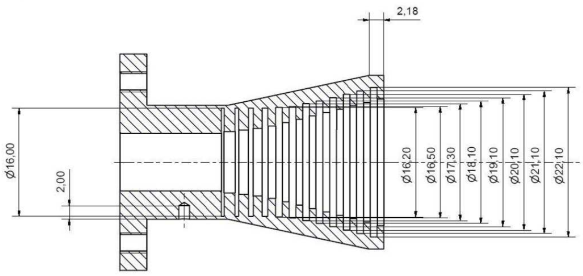

Figure 6.1: Mechanical drawing of the corrugated horn antenna.

Return Loss

The Figure 6.2 shows that the Return Loss simulated by *FHAPP* is less than $-30dB$ over the whole band, so it seems better than the RL requested in the specification (see Table 6.1).

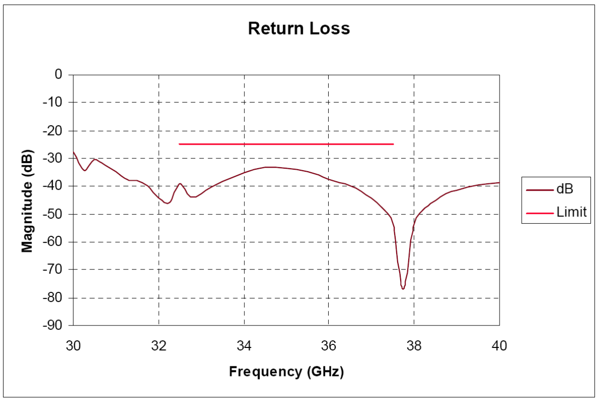

Figure 6.2: Return Loss response obtained through *FHAPP* simulation.

Radiation Patterns

The results of the radiation pattern simulations as obtained through *FHAPP* analysis are here presented in the following Figures 6.3 and 6.4 for the principal cuts and for the 45° cut (*3th Ludwig's Definitions*) [48] at the central frequency, f = 35 GHz, and at the limit frequencies of the band, f = 32.5 GHz and f = 37.5 GHz.

Error Analysis

The horn will be fabricated by electroforming technique, with the purpose to test and ensure the quality of the industrial process. An aluminium mandrel

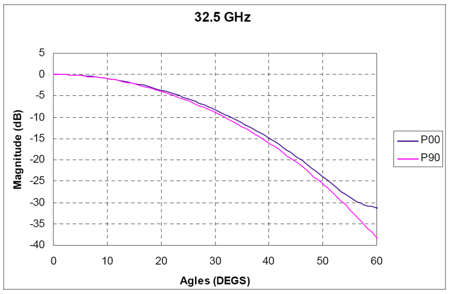

Figure 6.3: *FHAPP* calculated radiation patterns at f = 32.5 GHz: co-polar component in the principal planes (P00: Φ = 0°; P90: Φ = 90°).

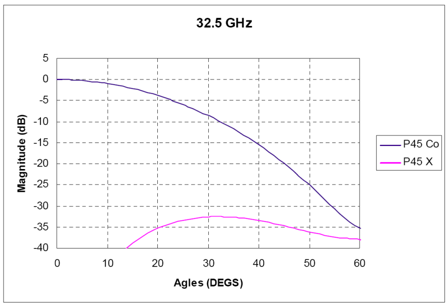

Figure 6.4: *FHAPP* calculated radiation patterns at f = 32.5 GHz in the Φ = 45° plane (P45 Co: co-polar; P45 X: Φ = 45°, cross-polar).

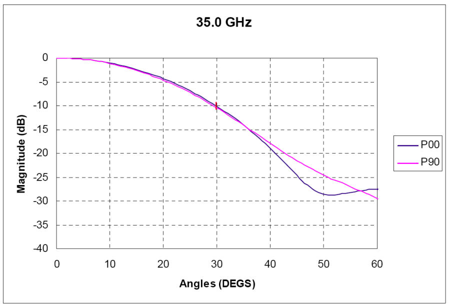

Figure 6.5: *FHAPP* calculated radiation patterns at f = 35.0 GHz: co-polar component in the two principal planes (Φ = 0° and Φ = 90°).

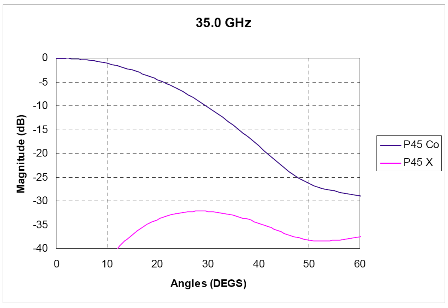

Figure 6.6: *FHAPP* calculated radiation patterns at f = 35 GHz: co-polar and cross-polar components in $\Phi = 45°$ plane

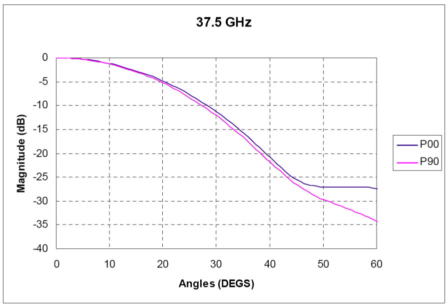

Figure 6.7: *FHAPP* calculated radiation patterns at f = 37.5 GHz: co-polar component in two principal planes ($\Phi = 0°$; $\Phi = 90°$).

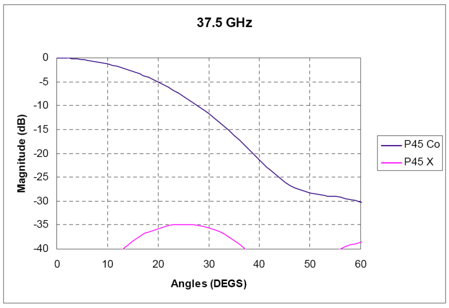

Figure 6.8: *FHAPP* calculated radiation patterns at f = 37.5 GHz: co-polar and cross-polar components in $\Phi = 45°$ plane

will be built in order to obtain precise internal dimensions of the horn. The most critical aspect of the manufacturing process is the precision in the height of each tooth, due to the fact that the currents on the mandrel surface are stronger in correspondence to the corrugations, and may close the way to form the teeth. In order to examine the effect of the tolerances on the height of the teeth, an error on the diameter dimensions has been imposed on some corrugations in different positions along the horn, as described in Table 6.2 and Figure 6.9. The corresponding Return Loss responses (*FHAPP* analysis) are given in Figure 6.10.

Best	Nominal condition
Step 1	First Corrugation radius increased by 0.01 mm
Step 2	First tooth radius increased by 0.01 mm (Point 1 in Figure 6.9)
Step 3	Tooth N 1 radius increased by 0.02 mm (Point 1 in Figure 6.9)
Step 4	Tooth N 3 radius increased by 0.01 mm (Point 3 in Figure 6.9)
Step 5	Tooth N 3 radius increased by 0.02 mm (Point 3 in Figure 6.9)
Step 6	Teeth N 2 3 4 radii increased by 0.02 mm (Point 2,3,4 in Figure 6.9)

Table 6.2: List of the error steps imposed to the nominal geometry.

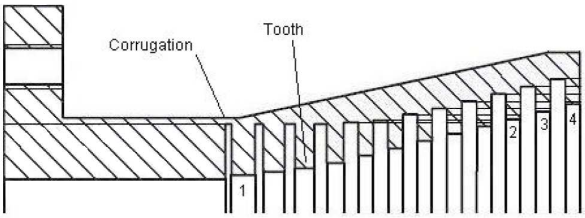

Figure 6.9: Sketch of the horn with indication of the teeth where error have been imposed.

From the results in Figure 6.10 it is clear that a tolerance on the diameter less than 0.02 mm would be acceptable. In Figures 6.11 and 6.13 the principal patterns for the worst case (Step6) are given, showing that there is no substantial difference from the patterns obtained in the nominal condition.

6.1.4 CST Microwave Studio Simulations

In order to check the accuracy of the results obtained with FHAPP analysis, the feed-horn has been analyzed by a full-wave technique, by using the commercial software CST MWS (finite integration in time domain). A sketch of the model that has been simulated is shown in Figure 6.14.

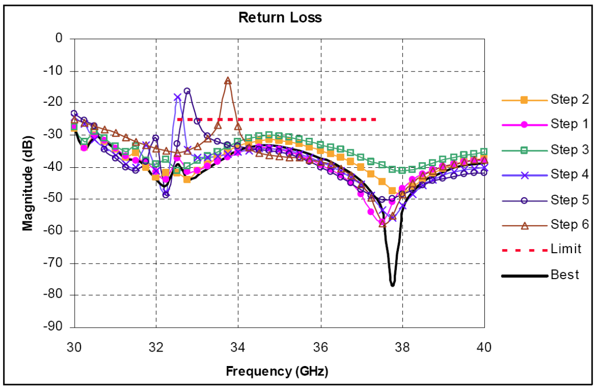

Figure 6.10: Return Loss of the horn with the imposed errors as in Table 6.2.

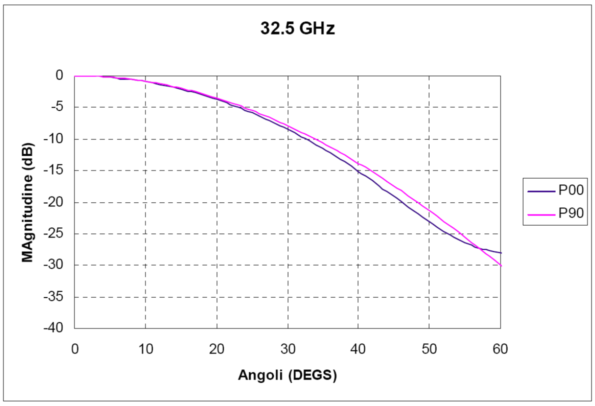

Figure 6.11: Step 6, *FHAPP* calculated radiation patterns at $f = 32.5$ GHz: co-polar component in the two principal planes ($\Phi = 0°$ and $\Phi = 90°$).

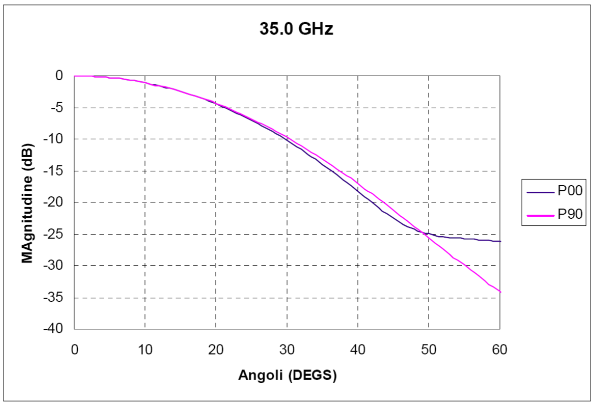

Figure 6.12: Step 6, *FHAPP* calculated radiation patterns at $f = 35.0$ GHz: co-polar component in the two principal planes ($\Phi = 0°$ and $\Phi = 90°$).

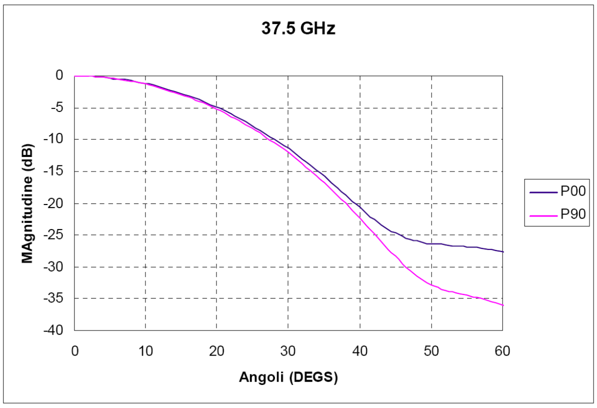

Figure 6.13: Step 6, *FHAPP* calculated radiation patterns at f = 37.5 GHz: co-polar component in the two principal planes ($\Phi = 0°$ and $\Phi = 90°$).

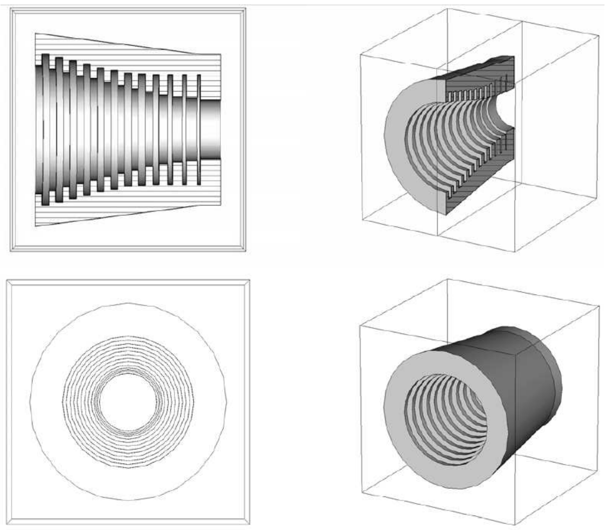

Figure 6.14: Model of the corrugated horn that has been simulated through CST-MWS. The sketches depict different points of view and longitudinal section.

In the following the results of CST-MWS simulations are compared to those previously obtained through FHAPP analysis.

Return Loss

The return loss response of CST-MWS does not coincide with the one obtained thorugh FHAPP analysis, but it is still below −30 dB. The VSWR responses are shown in Figure 6.15. A detailed analysis of the different simulations and measurements will be discuss in Chapter 7

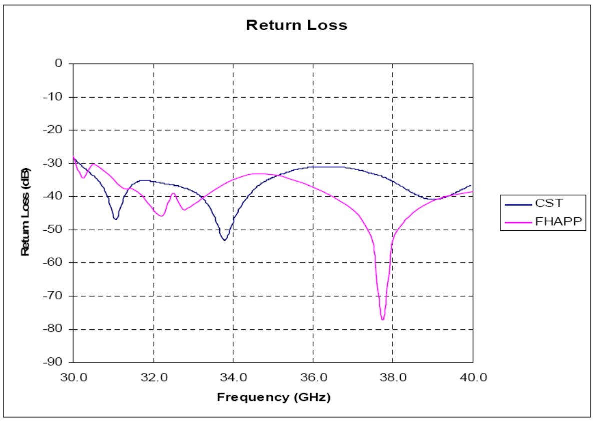

Figure 6.15: Return Loss response: CST-MWS vs FHAPP.

Radiation Patterns

Figures 6.16, 6.17, 6.18 show the accordance between the simulations that has been done with CST and FHAPP softwares. The E and H -Plane curves, at different frequencies, have the same shape before 20 and 40 degrees respectively.

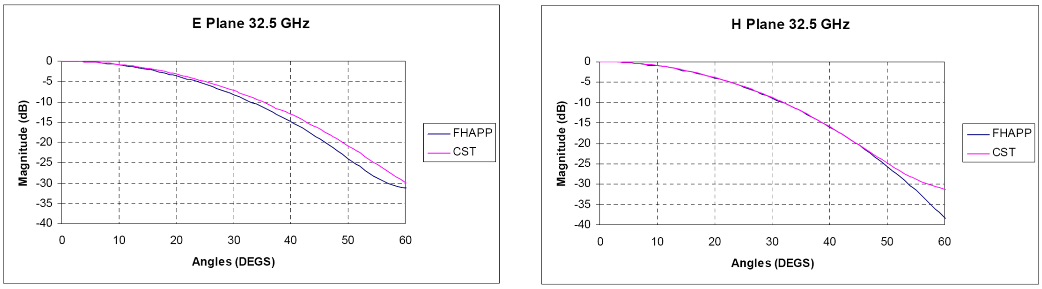

Figure 6.16: E and H -Plane Pattern Simulations at f = 32.5 GHz: CST-MWS vs FHAPP.

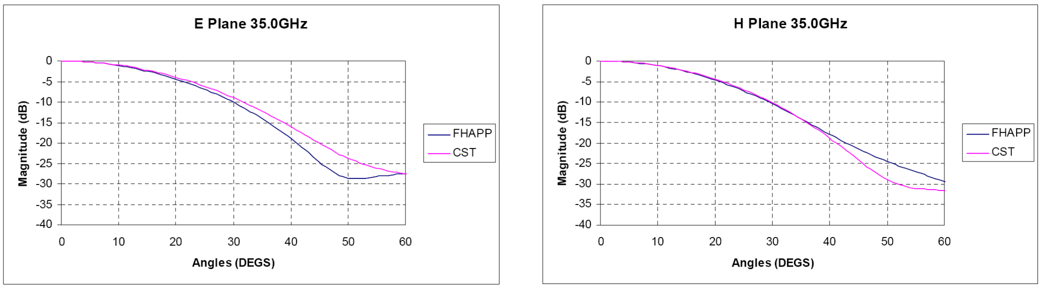

Figure 6.17: E and H -Plane Pattern Simulations at f = 35 GHz: CST-MWS vs FHAPP.

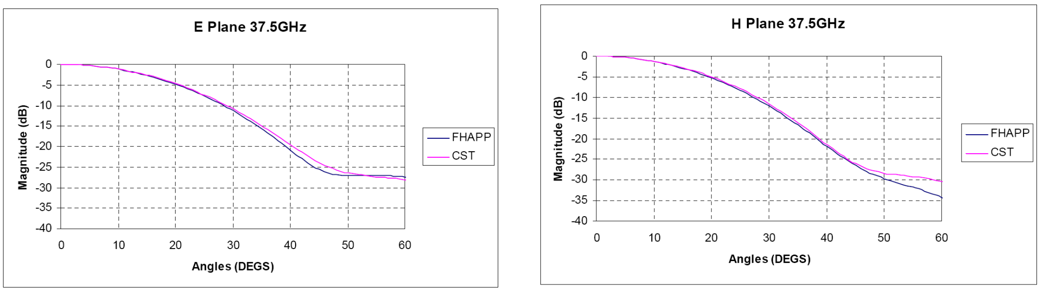

Figure 6.18: E and H -Plane Pattern Simulations at f = 37.5 GHz: CST-MWS vs FHAPP.

6.1.5 Conclusions

The result of the design of a corrugated horn antenna in Ka-band has been presented.

Two sets of theoretical results, in terms of Return Loss and Radiation Patterns, have been provided and compared. The first set has been obtained through a Mode Matching analysis (FHAPP). The second set has been derived from simulations through the commercial software CST-Microwave Studio. Both sets of results, even if not coinciding, satisfy the specifications. A very simple study of the error that may derive from fabrication tolerances has also been presented.

The corrugated horn has been manufactured by Officine Pasquali of Firenze using a electroforming technique (see § 6.1.3).

6.2 The *ViKy's* Reflectarray

The aim of this section is to introduce the theory used for the reflectarray design and to describe in details the manufacturing method used. The criteria followed has been introduced from Pozar [59].

I will describe the antenna specifications (*specs*), the materials and the optic configurations (onset and offset). Later on I will briefly discuss the curves of the reflection phase coefficient versus of the patch dimensions and the incident angle of the electric field.

6.2.1 Antenna description

As explained in §3.2, the shape that has been chosen for the patch of the *ViKy* project is rectangular, whereas the dimensions of the single patches depend on the frequency band where they work, while the dimensions of the whole reflectarray depend on the optical requirements: f/D ratio, total aperture efficiency, etc (see §4.2.4).

Considering the reflectarray dimensions and those of a single cell, the number of patch is 20 in both the azimuth and elevation sides as shown in Figure 6.19.

The main characteristics of the antenna are described in Table 6.3.

Number of patches	32×32
Antenna dimensions (mm)	220×220
Patch's shape	Rectangular
Center frequency (GHz)	35
HPBW (°)	3

Table 6.3: Reflectarray specifications.

Planar Array Description

The distance between the center of two adjacent patches is usually named *cell dimension*. This quantity is uniform in both the longitudinal and transversal dimensions and has been optimized to obtain an Half Power Beam Width (*HPBW*) of 3 degrees and no-grating lobes within 30 degrees. The *cell dimension* that has been chosen in the geometry of the WiKy project will be equal to $d = 0.775 \times \lambda_0 = 6.64\ mm$ where λ_0 is the wavelength corresponding to the frequency of 35 GHz.

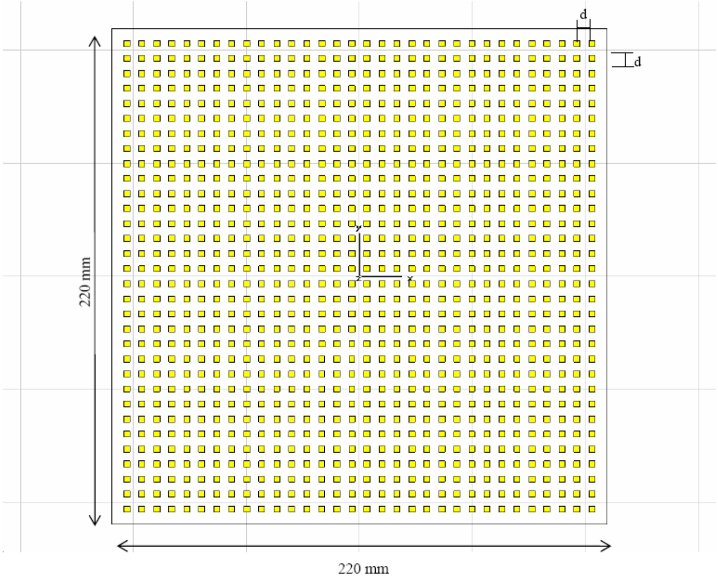

Figure 6.19: Array dimensions.

Single patch description

The choice of the single radiant element falls on two types: Stub Terminated Patch [39] or Variable Size Patch [59]. The first type of a reflectarray has a cross polarized level (see § 5.3.4) larger than the second type and the dependence between the phase of the reflection coefficient and the stub length is not linear. For these reasons the Variable Size Patch technique has been chosen.

First of all it is necessary to dimension a single rectangular patch such that the phase of the reflected field of the perpendicular incident plane wave over the patch surface will be equal to zero degrees. The patch is printed on a single layer substrate as shown in Table 6.4. The single layer structure of the patch is shown in Figure 6.20.

Dielectric substrate	Arlon DiClad 880 (ϵ_r = 2.17)
Dielectric substrate thickness (mm)	0.508
Copper patch thickness (mm)	0.017

Table 6.4: Characteristics of the substrate.

Reflectarray (planar array *plus* feed horn)

Figure 6.21 shows the geometric offset configuration of the *ViKy* antenna system. Both the onset and the offset configurations have been studied and carried out; here, for simplicity, I will explain only the offset configuration.

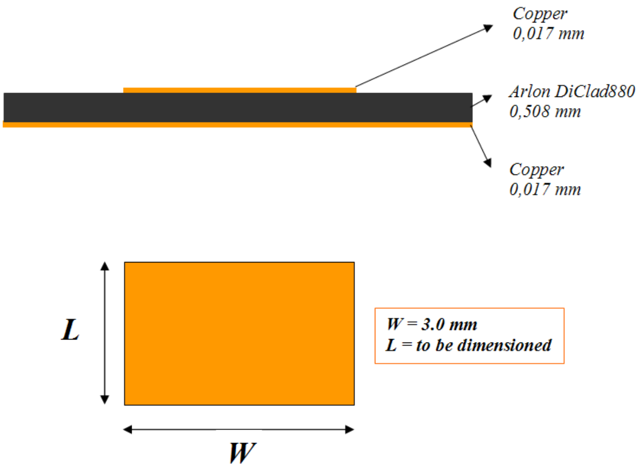

Figure 6.20: Geometry of the single layer microstrip patch.

It's well known that using the offset configuration it is possible to neglect the blockage effects due to the illuminator and to the structure that might decrease the directivity and introduce diffraction effects which generally are difficult to simulate.

For sake of brevity the phase center of the feed horn is aligned with the bottom edge of the reflectarray plane. In such a way the line that ideally connect these two points is parallel to the r_0 vector that is normal to the equiphase plane.

The latter is parallel to the reflectarray surface if the following relation is satisfied for each ray reflected by the corresponding patch [59]:

$$k_0(R_i + r_i \cos(\alpha)) - \Psi_i = 2\pi N \ . \tag{6.1}$$

Here R_i is the incident ray coming from the feed whereas r_i the reflected one.

The Ψ_i contribution is the phase shift that the reflection of the $i-th$ element must introduce to satisfy Equation (6.1).

Phase evaluation of the reflection coefficient

The whole reflectarray can be approximated as a square array of single cells each containing a patch.

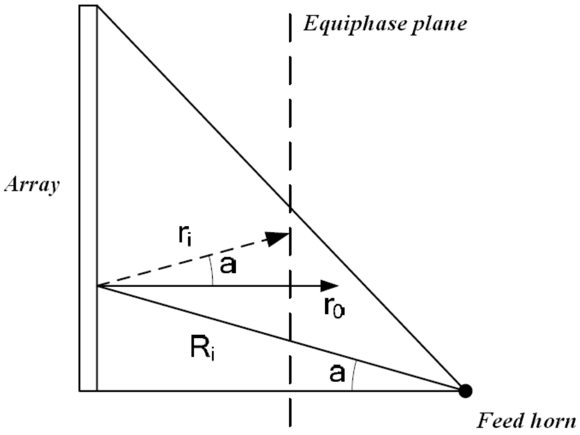

Figure 6.21: Offset configuration of the *ViKy* antenna system.

The total field reflected by the reflectarray is composed by two contributions:

- the specular reflection component due to the ground plane;
- the reradiated component due to the resonant activity of the patch.

Let us consider an incident plane wave:

$$\overline{E^i} = \overline{E_0} e^{jk_0(xu_i + yv_i + z\cos\theta_i)}, \tag{6.2}$$

where $\overline{E_0}$ is the vector of the incident field and

$$u_i = \sin\theta_i \cos\phi_i$$

$$v_i = \sin\theta_i \sin\phi_i \tag{6.3}$$

are the directional cosines of the incident wave; z is the propagation direction and $k_0 = \frac{2\pi}{\lambda_0}$. In the absence of patches the reflected field from the dielectric substrate and from the ground plane could be expressed as:

$$\begin{bmatrix} E^r_\theta \\ E^r_\phi \end{bmatrix} = \begin{bmatrix} R_{\theta\theta} & 0 \\ 0 & R_{\phi\phi} \end{bmatrix} \begin{bmatrix} E_{0\theta} \\ E_{0\phi} \end{bmatrix} e^{jk_0(xu_i + yv_i - z\cos\theta_i)}, \tag{6.4}$$

where $R_{\theta\theta}$ and $R_{\phi\phi}$ are the reflection coefficients. The diffracted field generated from the patch can be expressed by means of the Scattering (S) Matrix [6]:

$$\begin{bmatrix} E^s_\theta \\ E^s_\phi \end{bmatrix} = \begin{bmatrix} S_{\theta\theta} & S_{\theta\phi} \\ S_{\phi\theta} & S_{\phi\phi} \end{bmatrix} \begin{bmatrix} E_{0\theta} \\ E_{0\phi} \end{bmatrix} e^{jk_0(xu_i + yv_i - z\cos\theta_i)}. \tag{6.5}$$

The total field reflected from the reflectarray in the specular direction of the incident field can be expressed as:

$$\overline{E^T} = \overline{E^r} + \overline{E^s} = [\overline{\overline{R}}(\theta_i, \phi_i) + \overline{\overline{S}}(\theta_i, \phi_i)] \cdot \overline{E_0} e^{jk_0(xu_i + yv_i - z\cos\theta_i)} \ . \tag{6.6}$$

The phase defined in Equation (6.1) can be determined by Equation (6.6). The total reflection coefficient can be expressed as:

$$\overline{\overline{R^T}}(\theta_i, \phi_i) = \overline{\overline{R}}(\theta_i, \phi_i) + \overline{\overline{S}}(\theta_i, \phi_i) \ . \tag{6.7}$$

The above pattern calculation uses only a conventional array summation technique without including the effects of mutual coupling or mutual scattering between elements. This is appropriate for a good determination of beam width, beam direction and pattern shape but will not give accurate side lobes and cross-polarization predictions. Since a reflectarray generally consists of a huge number of elements, it would be difficult to have a complete rigorous solution to include all mutual coupling effects, even with the modern-day computer capabilities. In my analysis an approximated method has been used that is quite accurate to calculate the radiation pattern. It first calculates the single element pattern of the reflectarray by assuming an infinite array environment with all surrounding elements identical. This single element pattern is then summed over for all the elements to generate the array far-field pattern.

As explained in §4.2.1, different shape curves have been obtained, using a commercial software (CST Microwave Studio), by varying the patch dimensions and the directions (angles) of the incident waves. The adopted approach is shown in Figure 6.22.

Figure 6.23 shows the different curves of phase obtained varying the angle of incidence $\theta_i = 0° \div 45°$ in the $\phi = 0$ plane. For angles of incidence smaller than $\theta = 20°$ it can be seen that the curves have the same shape. Then it is possible to approximate the radiation coming from the feed horn as it was coming from a far-field source. This is the first important approximation adopted in the *ViKy* project.

The same analysis has been carried out with different commercial softwares (CST-MS, HFSS) to validate the procedure. Moreover, different analysis techniques have been tested with both softwares to study the agreement of them. The results of this comparisons are shown in Figure 6.24.

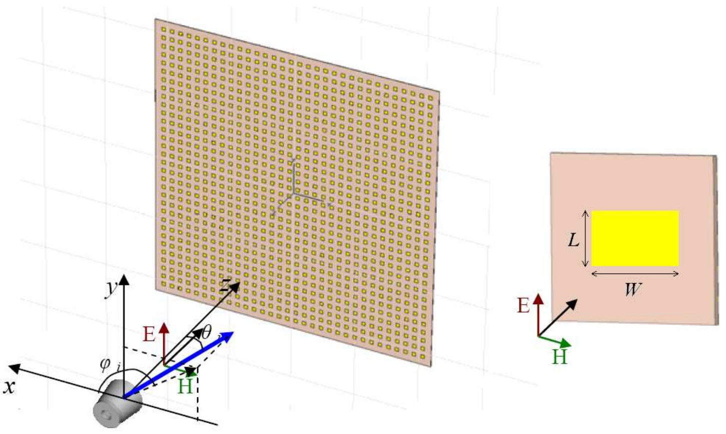

Figure 6.22: Geometry of the simulations.

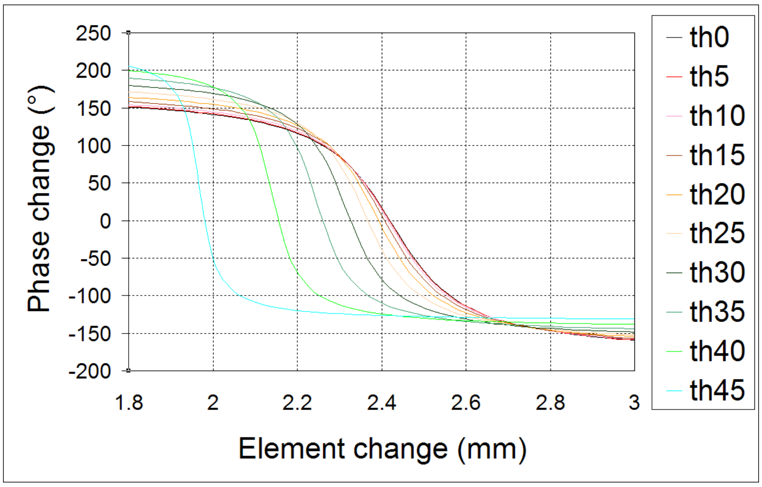

Figure 6.23: Curves of phase obtained with different angles of incidence.

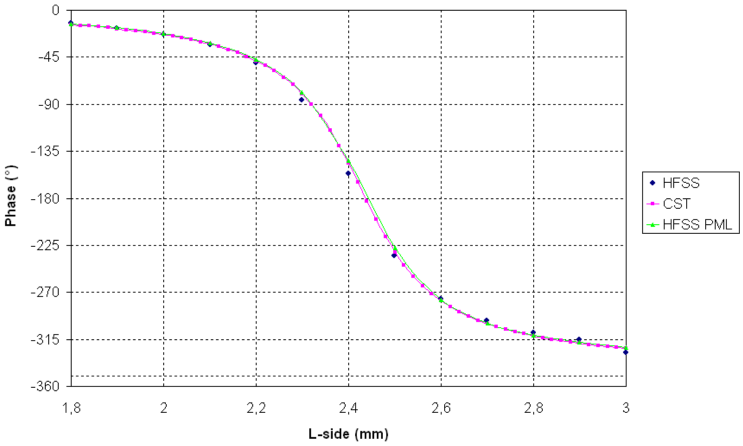

Figure 6.24: Curves of phase obtained with different software (CST-MS, HFSS).

Patch dimensioning

It is possible to consider two different approach to the design of a reflectarray. The first one consists in taking into account only the geometrical configuration, the ray tracing and the optical depth. Naturally this approach does not take into account the phase contribution due to the feed horn but only the distance between the center of phase of the feed and the center of the patch.
The second approach assumes also the just mentioned approximations by mean of a Optical Physic analysis (PO) with the commercial software *GRASP9* [25].

First approach

The position of each patch has been determined in spherical coordinates considering a reference system whose origin is coincident with the horn phase center. In this way the angle of illumination θ_{ij} will be equivalent to the incident angle of the electromagnetic wave in the reflectarray surface.

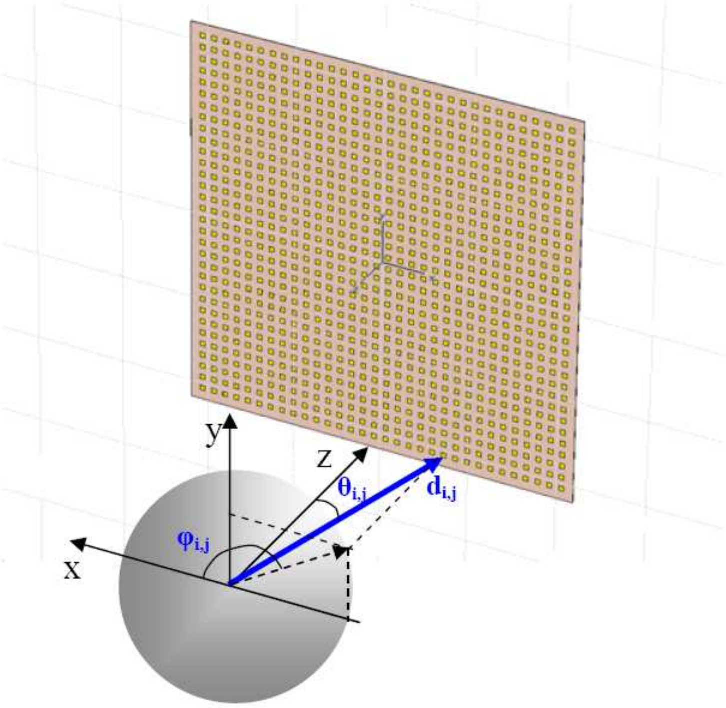

Figure 6.25: Antenna configuration with the feed reference system.

In Figure 6.25 it can be seen the spherical coordinates of the patches referred to the reference system connected to the feed:

$$
\begin{aligned}
d_{i,j} &= \sqrt{x_{i,j}^2 + y_{i,j}^2 + z_{i,j}^2} \\
\phi_{i,j} &= \arctan\left(\frac{y_{i,j}}{x_{i,j}}\right) \\
\theta_{i,j} &= \arcsin\left(\frac{\sqrt{x_{i,j}^2 + y_{i,j}^2}}{d_{i,j}}\right)
\end{aligned}
\tag{6.8}
$$

where $x_{i,j}, y_{i,j}, z_{i,j}$ are the patch coordinates in the Cartesian reference system connected to the phase center of the feed (the z axis is parallel to the one of the reflectarray but with opposite direction); $d_{i,j}$ is the distance between the feed center of phase and the patch center; $\theta_{i,j}$ and $\phi_{i,j}$ are the incident angles of the electromagnetic wave considered locally as it was plane respect to the patch dimensions. The left panel of the Figure 6.26 shows the distribution of the distances between the feed phase center and the center of the patches. The right panel of the same figure shows the distribution of the incidence $\theta_{i,j}$ angle.

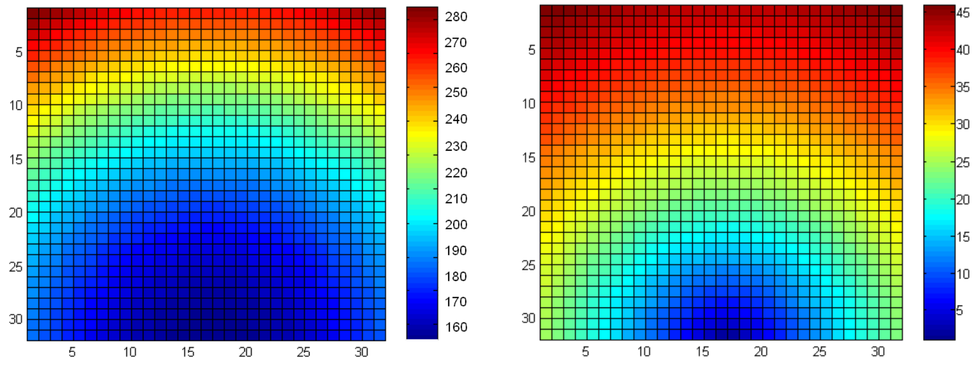

Figure 6.26: Distribution of the distance (mm) and of the $\theta_{i,j}$ angle (°) between the patch and the phase center of the feed.

The phase contribution necessary to obtain a planar wave front parallel to the patch surface is:

$$\Psi_{i,j} = \Lambda_{i,j} \cdot \frac{2\pi}{\lambda} , \tag{6.9}$$

where $\Lambda_{i,j} = d_{ref} - d_{i,j}$ is the difference between the reference distance d_{ref} (distance between the feed phase center and the middle of the reflectarray) and the optical path $d_{i,j}$ between the feed phase center and the center of the patches.

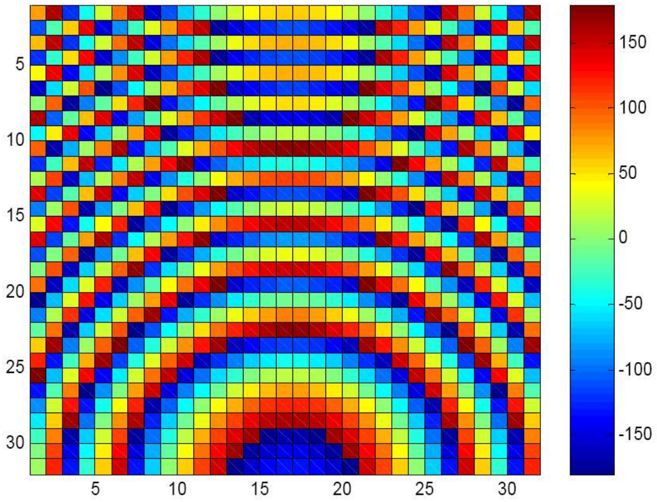

Figure 6.27: Distribution of the $\Psi_{i,j}$ phase contribution (the scale factor is expressed in degree).

In conclusion, the total phase contribution (shown in Figure 6.28) is due to the one related to the feed horn phase summed with the contributions obtained by Equations (6.8) and (6.9).

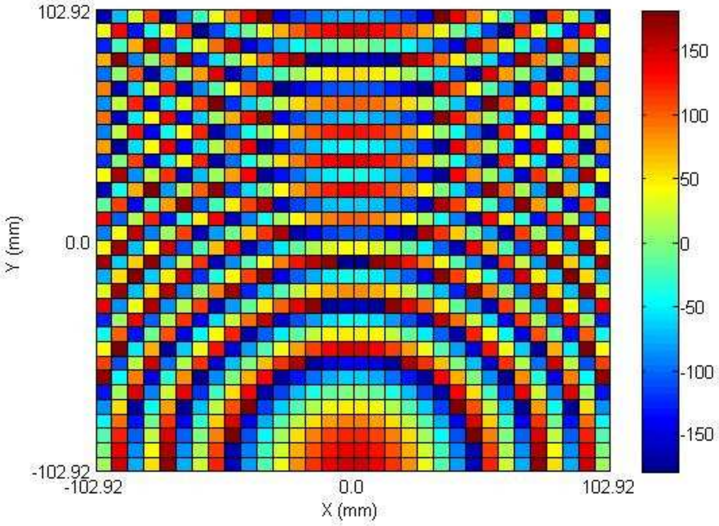

Figure 6.28: Total phase contribution using the Offset configuration.

Second approach

The amplitude and phase distribution in an ideal grid positioned over a planar surface can be calculated by Grasp9 using a routine ad hoc created both for the onset and the offset configurations. This routine allows to consider the phase contribution due to the feed horn simply inserting the position of the center of phase of the feed, its exact position with respect to the reflectarray plane and the feed horn pattern. This last option can be carried out inserting a suitable number of cuts representative of the pattern (72 cuts in this case). The Figures 6.29 and 6.30 show the ray tracing in the Offset and Onset configuration respectively.

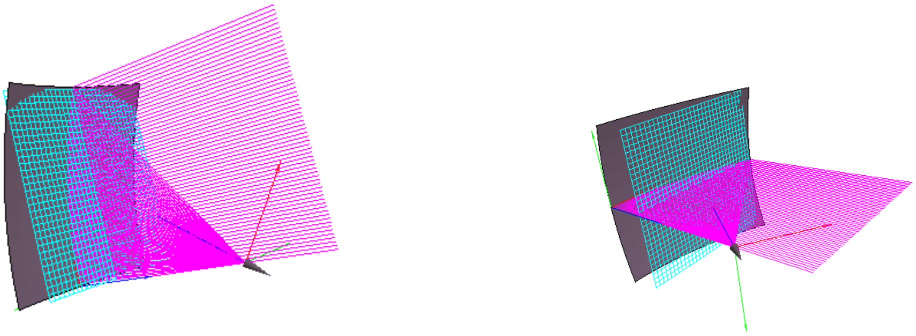

Figure 6.29: Grasp ray tracing for the Offset configuration.

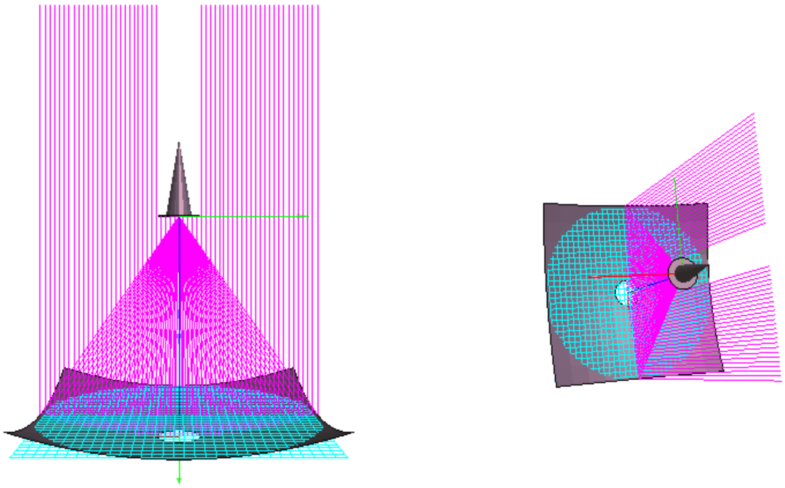

Figure 6.30: Grasp ray tracing for the Onset configuration.

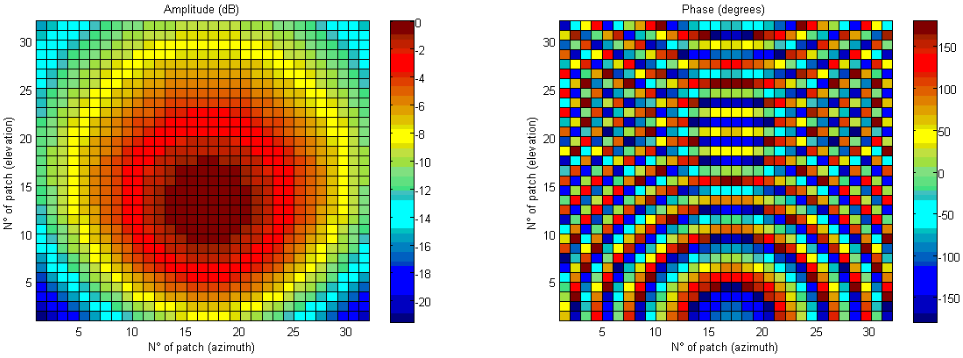

Figure 6.31: Amplitude and phase distribution for the Offset configuration obtained with Grasp9.

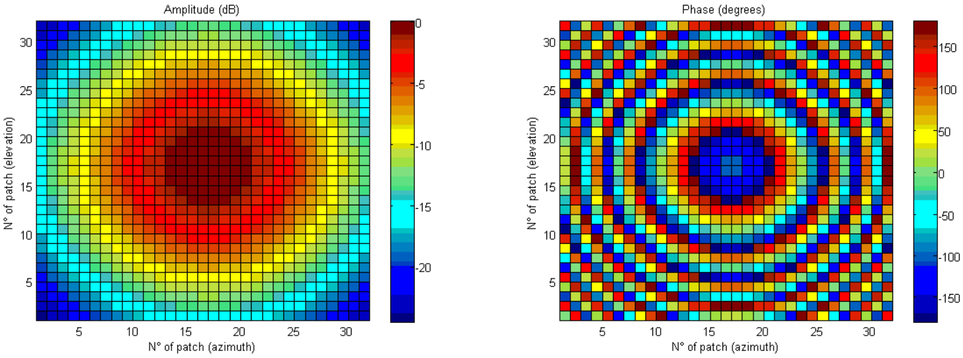

Figure 6.32: Amplitude and phase distribution for the Onset configuration obtained with Grasp9.

Final Patch dimensioning

To dimension the whole reflectarray it is necessary to use the relation between the total phase contribution and the dimensions of the resonant size (L) of the patches as shown in Figure 6.24. The algorithm uses the contribution shown in Figure 6.28 to produce the map of the resonant size dimensions.

Thanks to this analytical approach it is possible to design a new reflectarray very quickly. Figure 6.33 shows both the Offset and Onset configuration distributions of patch dimensions.

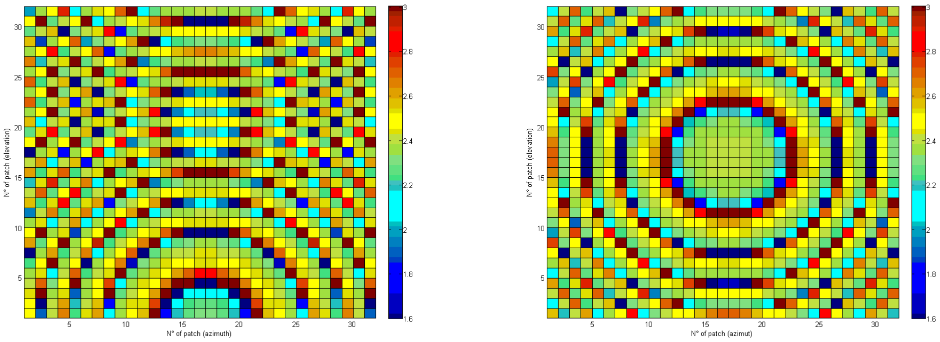

Figure 6.33: Distribution of patch dimensions (Offset and Onset cases).

6.2.2 Analytical results

Possible ideal patterns of the whole antenna system (reflectarray and horn) have been analytically calculated both in the onset and offset configurations.

As described in [75] when a rectangular planar array with M × N patch elements is non-uniformly illuminated by a feed positioned in $\vec{r}_f$, the scattered field in a given direction $\hat{u}$ will be:

$$E(\hat{u}) = \sum_{m=1}^{M}\sum_{n=1}^{N} F(\vec{r}_{mn} \cdot \vec{r}_f) A(\vec{r}_{mn} \cdot \hat{u}_0) A(\hat{u} \cdot \hat{u}_0) \cdot \exp^{\{-jk_0[|\vec{r}_{mn} - \vec{r}_f| + \vec{r}_{mn} \cdot \hat{u}] + j\alpha_{mn}\}} \tag{6.10}$$

where F is the electric field pattern of the feed horn, A is the electric field pattern of the patch, $\vec{r}_{mn}$ is the position vector of the mn-th patch, $\hat{u}_0$ is the direction of the main beam and α_{mn} is the phase-delay of the mn-th patch. If φ_{mn} is the phase of the newly radiated electric field and $b = 0, 1, 2$, the condition to make the total reradiated field cophasal and to concentrate it toward a specific direction is:

$$\varphi_{mn} = -k_0[|\vec{r}_{mn} - \vec{r}_f| + \vec{r}_{mn} \cdot \hat{u}] + j\alpha_{mn} = 2b\pi \,, \tag{6.11}$$

To take into account the blocking effect due to the structure, every element has been approximated as an isotropic element fed by a voltage generator of value:

$$V_{mn} = F(\vec{r}_{mn} \cdot \vec{r}_f)A(\vec{r}_{mn} \cdot \hat{u}_0)\exp^{\{j\varphi_{mn}\}} \ . \tag{6.12}$$

Ideally φ_{mn} should be zero, but errors in manufacturing or in approximation can generate different values. Every new element represents a source that radiates in the space. The effect of the whole structure can be computed using the method of moments Electric Field Integral Equation (EFIE) formulation as described in [28]. The total field will be:

$$E_{\hat{u}} = A(\hat{u} \cdot \hat{u}_0) \cdot \sum_{m=1}^{M} \sum_{n=1}^{N} E_{mn}^{scat}(\vec{r}_{mn} \cdot \hat{u}_0) \ , \tag{6.13}$$

where E_{mn}^{scat} represents the field of mn-th element taking into account the scattering of structure.

6.2.3 Reflectarray manufacturing

Here below I will describe the steps followed during the manufacturing

Engineering

The patch dimension distribution has been transformed from the mask in *excel* format to the mask in *gerber* format.

Plate's Cut

The reflectarray has been cut depending from the final dimensions, in this case 220 mm per side.

Plate's piercing

The reflectarray has been pierced to allow its positioning in the finally mechanical structure.

Micro-etching

The Micro-etching is a chemistry process to activate the copper reflectarray surface creating a micro-wrinkled-surface useful for the next process.

Dry-film lamination

The Dry-film is a thin skin ($50\mu m$) of photo-polymer applied only over the reflectarray surfaces to cover them from the Dry-film exposition.

Dry-film exposition

The reflectarray previously laminated has been exposed to a UV light using a special photographic mask to cover the patches.

Dry-film development

The Dry-film development remove the Dry-film in excess from the surface leaving the pacthes protected from it.

Etching

The free copper, in excess from the reflectarray surface, has been removed thanks to a chemistry process.

Test

The reflectarray that has been manufactured is now ready to be checked and tested using a microscope.

6.3 The *ViKy's* Radiometer

As previously mentioned in § 2.5, the radiometer measures the signal coming from the antenna and the minimum detectable signal is given by Equation (2.1). Figure 6.34 shows the path of the signal coming from the antenna system to the diode detector. The input power is proportional to Boltzmann's constant, the physical temperature and the frequency band:

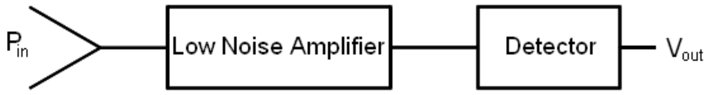

Figure 6.34: Radiometric diagram.

$$P_{in} = k_B T \Delta\nu = 1.38 \cdot 10^{-23} JK^{-1} \times 600K \times 5 \cdot 10^{9} Hz \simeq 10^{-11} W \ , \qquad (6.14)$$

or equivalently it can be expressed in dBm by equation

$$P_{in}|_{dBm} = 10 \cdot \log_{10} P_{in}|_W + 30 = -80\ dBm\ . \qquad (6.15)$$

Experimental measurements show that the minimum detectable signal is of the order of the mW ($1mW = 0dBm$).

$$P_{out}|_{dBm} = P_{in}|_{dBm} + P_{Gain} > 0dBm\ , \qquad (6.16)$$

$$P_{out}|_{dBm} = P_{in}|_{dBm} + P_{Gain} > -30dB\ , \qquad (6.17)$$

The total gain required to allow the signal to be detectable will be *at least*:

$$P_{Gain} = P_{out}|_{dBm} - P_{in}|_{dBm} > +50dB\ . \qquad (6.18)$$

In order to achieve such a gain, a special Low Noise Amplifier (LNA) is needed. Thanks to the millimeter technology knowledge matured with the PLANCK satellite project the *ViKy's* radiometer has been designed and tested. The radiometer is composed of two single stage LNA of about 35 dB of gain each, in order to make possible the insertion of a filter or an attenuator as shown in Picture 6.35.

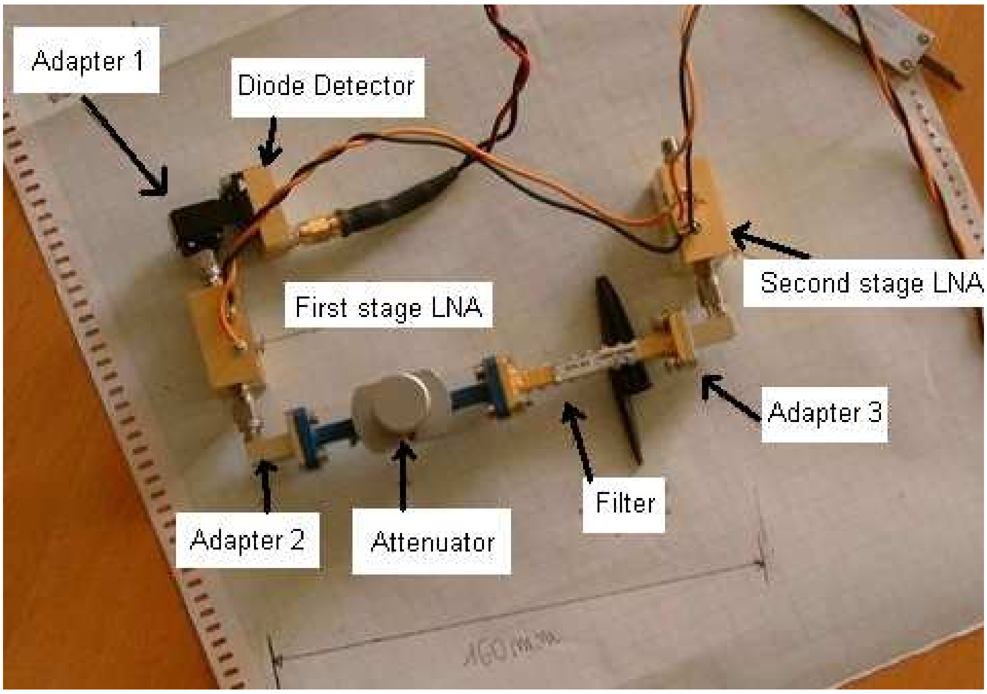

Figure 6.35: Picture of the radiometer assembled during the test campaign.

6.3.1 Noise Figure

In telecommunications, noise figure (*NF*) is a measure of degradation of the signal to noise ratio (*SNR*) caused by the insertion of spurious components in the *RF* signal chain. Noise figure is the ratio between the output noise power of a device and the portion related to thermal noise in the input termination at standard noise temperature T_0 (usually 290 K). Noise figure is thus the ratio of actual output noise to that which would remain if the device itself did not introduce noise. It is a quantity by which the performance of a radio receiver can be specified.

Essentially, noise figure is the difference in decibels (*dB*) between the noise output of the actual receiver to the noise output of an "ideal" receiver with the same overall gain and bandwidth when the receivers are connected to sources at the standard noise temperature T_0 (usually 290 K). The noise power from a simple load is equal to $k_B T \Delta \nu$, where k_B is the Boltzmann's constant, T is the absolute temperature of the load (for example a resistor), and $\Delta \nu$ is the measurement bandwidth.

This makes noise figure a useful figure of merit for terrestrial systems where the antenna effective temperature is usually not far from the standard of 290 K. For example, a receiver with a noise figure say N_x dB better than another will have an output signal to noise ratio that is about N_x dB better than the other. However, in the case of satellite communications systems, where the antenna is pointed out into cold space, the antenna effective temperature is often colder than 290 K. In these cases a N_x dB improvement in receiver noise figure will result in more than a N_x dB improvement in the output signal to noise ratio. For this reason, the related figure of effective noise temperature is often used instead of noise figure for characterizing satellite-communication receivers and LNA. The noise figure is defined as the ratio of the S/N ratio at the input to the S/N ratio at the output:

$$NF = \frac{SNR_{in}}{SNR_{out}} \tag{6.19}$$

where SNR_{in} and SNR_{out} are the input and output signal-to-noise ratios, respectively. Alternatively, noise figure may be defined in terms of dB units

$$NF_{dB} = 10 \log_{10}\left(\frac{SNR_{in}}{SNR_{out}}\right) = SNR_{in,dB} - SNR_{out,dB} \tag{6.20}$$

where $SNR_{in,dB}$ and $SNR_{out,dB}$ are the input and output signal-to-noise ratios in dB. The previous formula is only valid when the input termination is at standard noise temperature T_0.

These definitions are equivalent, differing only in the use of dB units. The first definition is sometimes referred to as **noise factor** F to distinguish it from the dB form.

The noise factor F of a device is related to its noise temperature via:

$$F = 1 + \frac{T_e}{T_0}\,, \tag{6.21}$$

where T_e is the effective (or equivalent) input noise temperature of the device and T_0 denotes a standardized temperature, which in this case is close to room temperature (290 K is an IEEE standard). Devices with no gain (e.g., attenuators) have a noise factor F equal to their attenuation L (absolute value, not in dB) when their physical temperature equals T_0. More generally, for an attenuator at a physical temperature T_{phys}, the noise temperature is $T_e = (L-1)T_{phys}$, thus giving a noise factor of

$$F = 1 + \frac{(L-1)T_{phys}}{T_0} \tag{6.22}$$

If several devices are cascaded, the total noise factor can be found with Friis' Formula [45]:

$$F = F_1 + \frac{F_2 - 1}{G_1} + \frac{F_3 - 1}{G_1 G_2} + \frac{F_4 - 1}{G_1 G_2 G_3} + \cdots + \frac{F_n - 1}{G_1 G_2 G_3 \cdots G_{n-1}} \tag{6.23}$$

where F_n is the noise factor of the $n-th$ device and G_n is the power gain (numerical, not in dB) of the $n-th$ device.

6.3.2 Y_{factor}

Y_{factor} is a ratio of two noise power levels, one measured with the noise source ON and the other with the noise source OFF:

$$Y_{factor} = N^{ON}/N^{OFF}$$

As noise power is proportional to noise temperature, it can be stated:

$$Y_{factor} = T^{ON}/T^{OFF}$$

The instruments used are designed to measure Y_{factor} by repeatedly pulsing the noise source ON and OFF. N_{ON} and N_{OFF} are therefore measured several times, so that an averaged value of Y_{factor} can be computed.

6.3.3 T_{NOISE}

Noise Figure and Temperature of noise can also be expressed by:

$$NF|_{dB} = 10 \cdot \log_{10}[(T_N/295°K) + 1] \tag{6.24}$$

$$T_N = 295 \cdot [10^{(NF|_{dB}/10)} - 1] \tag{6.25}$$

6.3.4 The Detector

Every radiometric measurement uses a detector in some way. This section discusses briefly how they are described and delineates their most important properties with respect to the radiometric measurements.

Detector description

The *ViKy's* radiometer uses a commercial diode detector. The Millitech series Cross Polar Detector (DXP), utilizing MIC technology and Schottky Barrier Beam Lead Diodes, provides a very economical solution for power detection over the 18 to 140 GHz range. Both high sensitivity and full waveguide bandwidths are achieved simultaneously without external Direct Current (DC) bias or adjustments. Positive or negative output voltage polarity is available for use with various scalar analyzers. These detectors have a flat frequency response, as their sensitivity shows minor variations over the entire waveguide band. Series DXP response is linear for power levels below −10 dBm. These units are thermally stable and small; for the applications requiring higher responsivity (mV/mW), like the *ViKy* system, they are really the best compromise.

6.4 The *ViKy's* Motion Control

The motion structure is designed as a modular frame in order to allow several configurations of planar array and horns. The motion is obtained by a step by step motor powered by DC current and controlled via software with a LabView program.

The frame is made of aluminum Anticorodal 100 in order to have a light weight structure and a good machinability. All the parts are protected by a layer of alodine. The shaft used for the motion are supported by two radial ball-bearing and the regulation of the end play is obtained with a light preload of the bearing.

The horizontal shaft has a static balancing only, the barycentre of the assembly planar array and horn is on the axis of rotation, a dynamic balancing is not required due to the very low speed of the shaft (the axis of rotation is not a principal axis of inertia). The vertical shaft does not have a balancing due to the motion law (low speed and little angle covered in each step).

To increase the torque on the shaft and the angular resolution it is used an harmonic drive with a ratio of 1:100, so on each shaft can be applied a torque of about 10 Nm.

The Figures 6.36 and 6.37 show the whole *ViKy's* structure from different point of view.

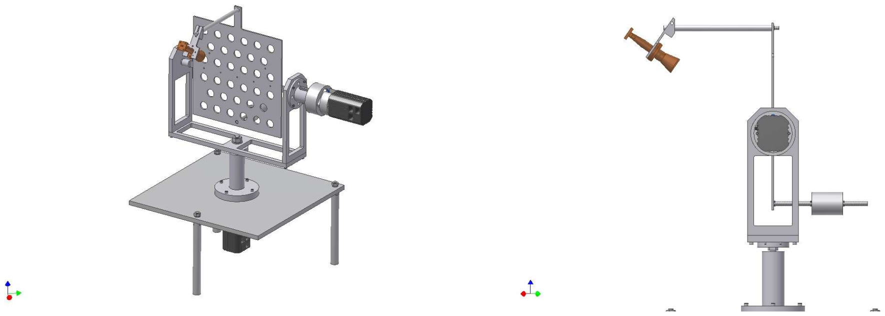

Figure 6.36: *ViKy's* structure (Isometric and lateral view).

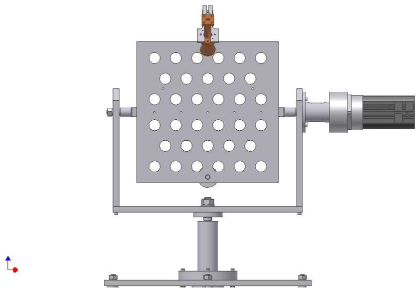

Figure 6.37: *ViKy's* structure (Front view).

6.5 Conclusion

In this chapter the procedure to realize a reflectarray has been described. The variable size technique has been used to realize a reflectarray working at 35 GHz composed of 32×32 elements. The cells dimensions, as well as the distances between the centers of patches have been optimized to have the

Half Power Beam Width of about 3 degrees; the value that has been chosen is of 6.64 mm. The choice of the substrate (Arlon DiClad880) depends on dielectric constant ($\epsilon_r = 2.17$) and manufacturing needed. The antenna configurations (both the onset and the offset) have been designed to achieve the optical specifications maintaining at the same time the whole structure easy to realize and economical.

The reflectarray has been designed such that the incident spherical wave coming from the feed horn changes into a planar wave with an equi-phase front. This has been realized varying the dimensions of the resonant side of the patches. In other words, the dimension variation of the resonant side of the patches corresponds to a change in the characteristic impedance of the reflectarray surface and consequently to the change of the phase of the reflection coefficient.

Using a software based on the Method of Moments (MoM) the reflection coefficient has been calculated varying the dimensions of patches.

Using *Grasp9*, amplitude and phase in a grid of points (corresponding to the center of the patches) placed over the incident surface of the reflectarray have been determined. This software allows to take into account the feed horn phase contribution and that due to the optical path.

The reflectarray electromagnetic measurements will be presented in the next chapter.

Chapter 7

Measurements

In this chapter I will describe the campaign regarding the functionality and qualification tests of the antenna system and of the radiometer. The electromagnetic measurements will be discussed regarding the horn, the reflectarray, the low noise amplifiers, the diode and the whole radiometric chain. The main results will be presented in order to validate the *ViKy* project and then to confirm the requirements described in the previous chapter.

The Low Noise Amplifiers and the Diode Detector have been tested at IASF (Istituto di Astrofisica Spaziale e Fisica cosmica) and IRA (Istituto di Radio Astronomia) laboratories whereas the horn and the reflectarrays have been tested in the anechoic chamber of the IFP (Istituto di Fisica del Plasma del CNR di Milano).

7.1 Electromagnetic horn measurements

The pattern measurements were made in an anechoic chamber mounting the Horn Under Test (HUT) on an xy translation stage mounted on a Millimeter Vector Network Analyzer (MVNA) controlled rotary platform to achieve a fine relative positioning of the axis of the HUT and the rotation axis. The alignment was aimed at getting a phase pattern as symmetric as possible in the central region (thus ensuring that the rotation axis actually crossed the horn symmetry axis) at the central frequency (35 GHz). The phase and amplitude patterns were taken with the rotation axis through the aperture (within ±0.1mm). The distance between generator and receiver was about 2 m. The return loss (RL) was measured with the MVNA in a calibrated single reflectometer configuration with the horn radiating into an Eccosorb^{TM} panel. A circular to rectangular transition was used to connect the horn to the test set-up. The contribution of the rectangular to circular transition has been removed using time domain filtering.

7.1.1 Analysis and results

The analysis shows:

- agreements between measurements and simulations for both the horns;
- agreements between Return Loss measurements and simulations for both the horns obtained with CST-MS and FHAPP;
- agreements between the two horns concerning the study of the manufacturing process and its capability to be reproducible.

Differences between measurements and simulations results for both horns

Figures 7.1 ÷ 7.3 show the E- and H- plane patterns measured and simulated with CST-MS at the three fundamental frequencies.

Figure 7.2 shows that the specification, concerning the taper, required in Table 6.1 has been fulfilled. At 35 GHz the value of the *taper* at 30 degrees is of -10dB with a tolerance of ±1 dB both in the E- and H-plane.

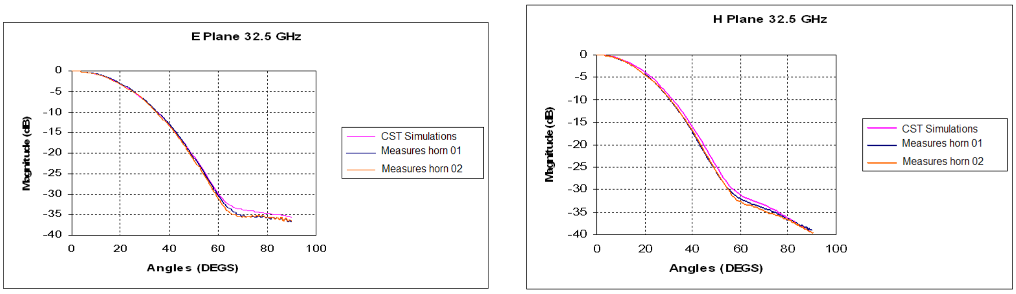

Figure 7.1: E and H -Plane Pattern Measures and Simulations at f=32.5 GHz.

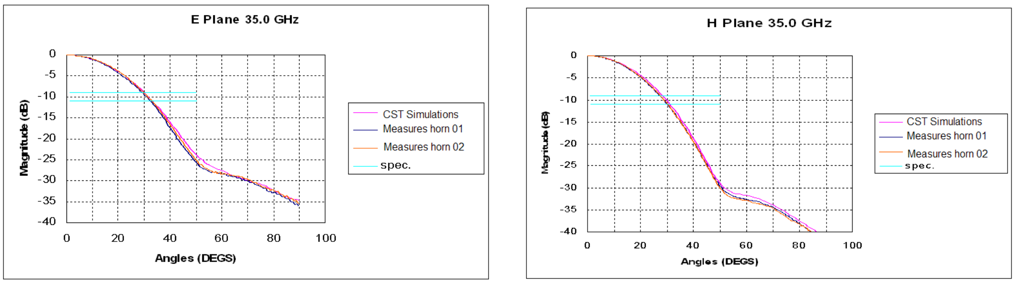

Figure 7.2: E and H -Plane Pattern Measures and Simulations at f=35.0 GHz.

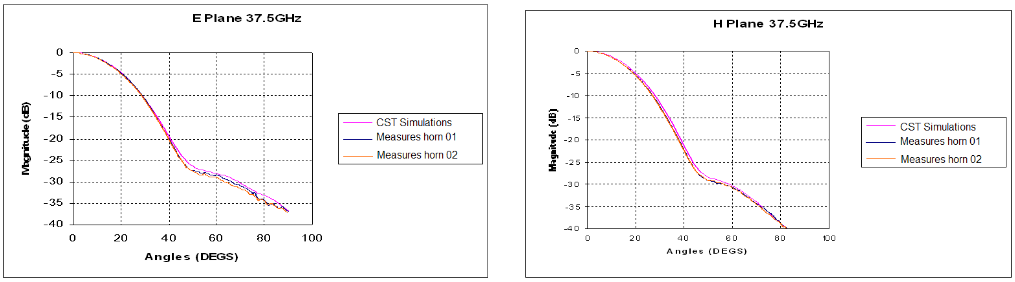

Figure 7.3: E and H -Plane Pattern Measures and Simulations at f=37.5 GHz.

Differences between Return Loss measurements and simulations results for both horns obtained with CST-MS and FHAPP

Figure 7.4 shows the Return Loss measured and simulated with CST-MS and FHAPP softwares for two different horns. The left panel shows that the RL measured is better than the one required in the specifications. The right panel shows that the FHAPP software can simulate correctly the RL.

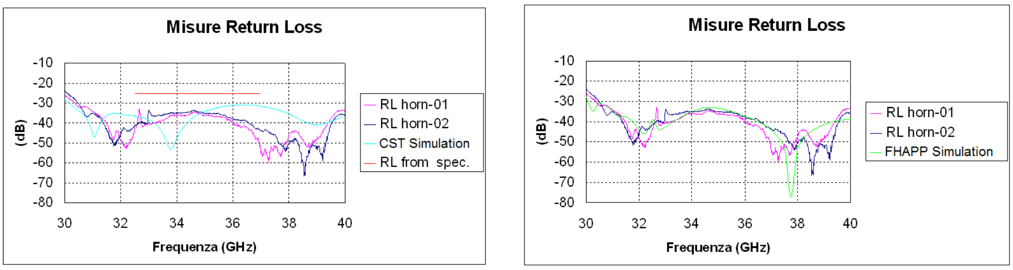

Figure 7.4: Return Loss Measures and Simulations for two different horns.

Analysis of the Measurements results

	E-plane @35GHz	H-plane @35GHz
Average(ABS(horn1-horn2)) (dB)	0.3193	0.2159
Max Value (ABS(horn1-horn2)) (dB)	0.9830	0.6090
min Value (ABS(horn1-horn2)) (dB)	0.0003	0.0006

Table 7.1: Horn analysis

The values of Table 7.1 show the capability of the horn's manufacturing process to be reproducible.

7.2 Electromagnetic reflectarray measurements

The measurements were performed with a Millimetre Vector Network Analyzer (MVNA) in an anechoic chamber. A Standard Gain Horn (SGH) with a conical profile was placed at about 2.5 meters from the aperture of Antenna system (reflectarray plus horn) under test and was used as the fixed receiver as shown in Figure 7.5. With the adopted setup, standing wave effects have been checked to have negligible effects on the pattern measurements. Standing waves are also known as stationary waves, they can arise in a stationary medium as a result of interference between two waves traveling in opposite direction. In resonators the standing waves are the cause of the resonance.

The Antenna System was mounted on a rotation stage connected to the MVNA, that can drive the angular sweeps directly. Two VNA heads measured the transmission between the Antenna System under test and the SGH at fixed frequency. Two translation stages were mounted above the rotation stage. They allowed the SGH to be moved with good precision along the x, y coordinates in the plane perpendicular to the rotation axis. The x movement (perpendicular to the horn axis) was required for alignment, to adjust the position of the horn so that its axis was exactly intersecting the rotation axis. This was necessary to avoid phase front measurements biased by a spurious contribution due to misalignment. The degree of freedom along the axis of the horn (i.e. y) was used to evaluate the position of the phase centre from the measured phase pattern, which was exactly flat when the rotation axis and the phase centre were coincident. Even if the translation stages have 0.01 mm precision, the overall uncertainty is given by the positioning of the horn on the mounts, therefore only ±0.5 mm.

7.2.1 Analytical VS measurements results

Some approximation could affect the analytical results and should be considered when analysing the data.

- First of all, every patch is dimensioned as if the front wave were parallel to the reflectarray surface. In the operational condition of the antenna system the radiation coming from the horn is not seen by the reflectarray as a plane wave. As a first approximation, the phase front is thought as spherical and a correction of the phase contribution of each patch is needed (spherical phase correction).

- Small errors in manufacturing of patches involve non-negligible errors in the computing of phase delay in the steepest zone of Figure 6.24.

- A phase delay of about 330 degrees can be obtained with a single layer reflectarray varying the dimension of the resonant side.

- The phase of the horn has been obtained via software in its own far field (not experimental measured) and the computing of phase center could be less accurate than expected.

- It needs to take into account also some error both in the manufacturing and alignment of the horn.

- The surface of the reflectarray is not completely plane.

- In addition to the reradiated field given by Equation (6.13) there is a certain amount of backscattered field from the patches, the ground plane and ground plane edges. Figures 7.11 and 7.12 show that in the on-set configuration the model implemented to take into account the blocking effects is more accurate than the one implemented for the offset configuration. In the second case the effect of backscattering of the ground plane and edges is likely predominant.
  However in both cases the requested specification regarding the Half Power Beam Width has been fulfilled.

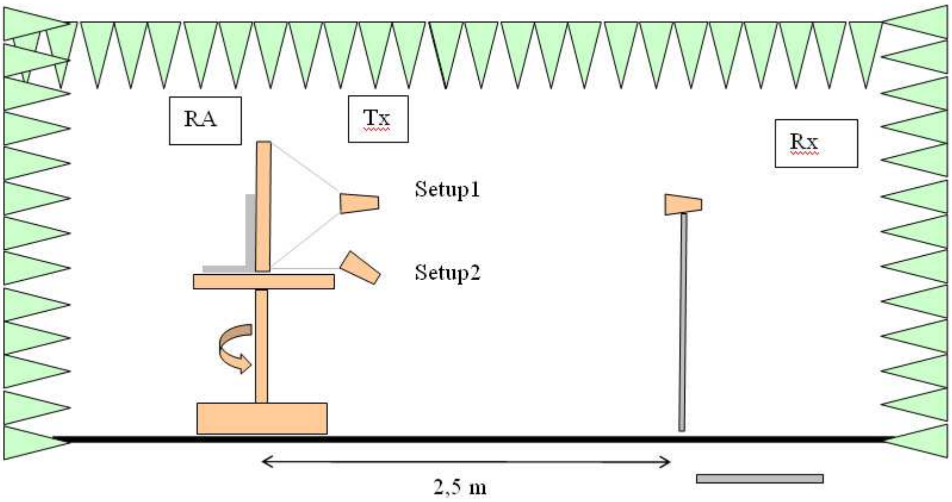

Figure 7.5: Setup for the electromagnetic measures (on- & off-set configuration).

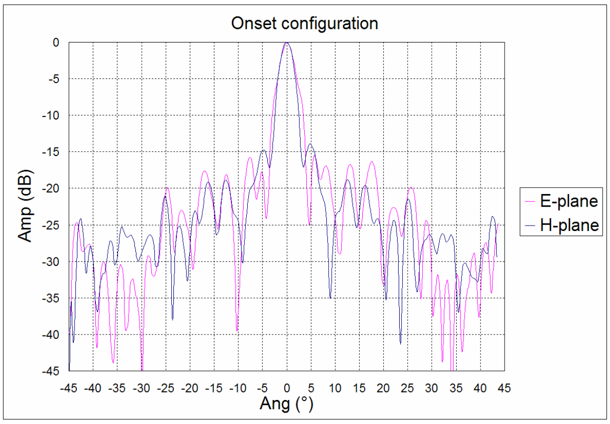

Figure 7.6: E- and H-plane pattern for the on-set configuration.

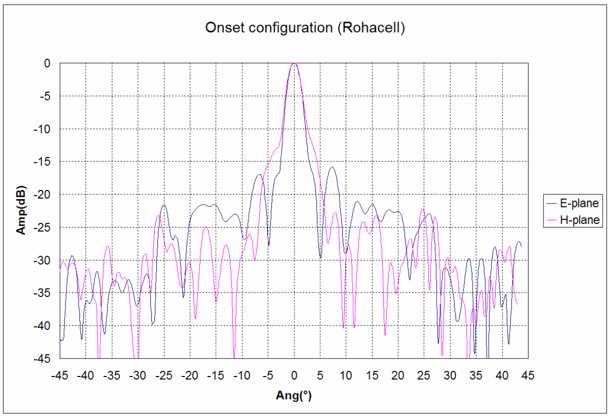

Figure 7.7: E- and H-plane pattern for the on-set configuration (with Rohacell).

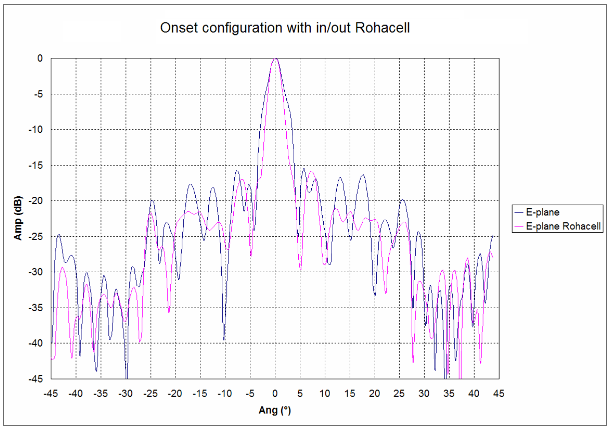

Figure 7.8: E-plane pattern for the on-set configuration (with in/out Rohacell).

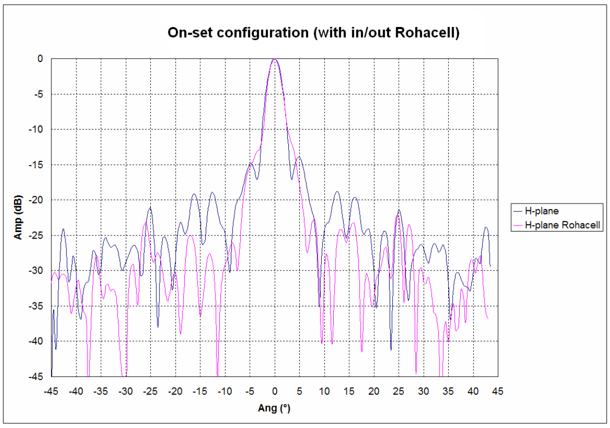

Figure 7.9: H-plane pattern for the on-set configuration (with in/out Rohacell).

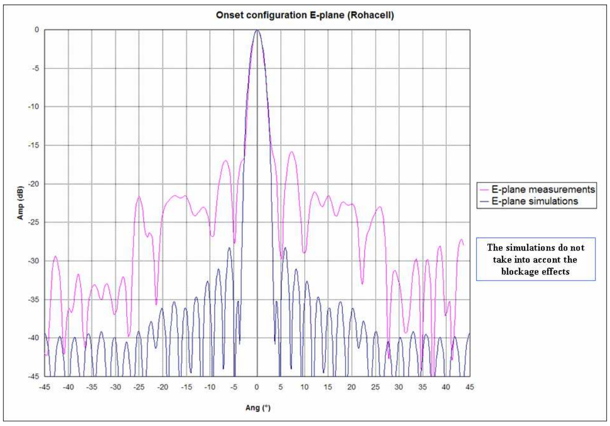

The simulations do not take into accont the blockage effects

Figure 7.10: E-plane pattern for the on-set configuration (measures VS simulations).

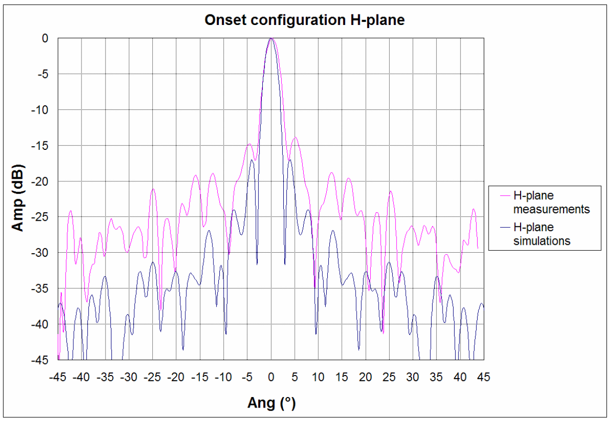

Figure 7.11: H-plane pattern for the on-set configuration (measures VS simulations).

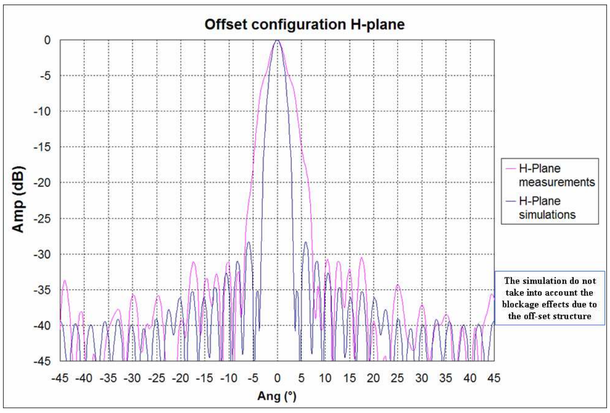

Figure 7.12: H-plane pattern for the off-set configuration (measures VS simulations).

7.3 Low Noise Amplifier measurements

In this section I will describe the measurement test carried out in the RF laboratory of IASF Bologna. A 8757D Scalar Network Analyzer coupled with a 8350B Sweep Oscillator has been used.
The two *ViKy's* amplifiers (DUT) have been characterized singularly and in pair.

7.3.1 Description of the setup measurements

The measurements show the gain curve of the amplifiers versus frequency. The input power has been varied using a power attenuator. The tests require the following procedure:

- Scalar Network calibration;
- storage of the attenuator curve at different frequencies;
- storage of the gain curve of the amplifiers.

The sweeper output power is fixed at a value of 10dBm, the frequency range is from 30 to 40 GHz and the number of calibration points is 401. Figure 7.15 shows the radiometric chain used during the tests; the input signal (IN) is divided in the first directional coupled and the Detector (R) receives about 10 dB of the input signal. R indicates the Reference Detector. The signal comes through the second directional coupled, the attenuator and the amplifier up to the Detector (B). The signal received in B compared to that received in R allows to neglect the power variation of the sweeper. The detector (A)

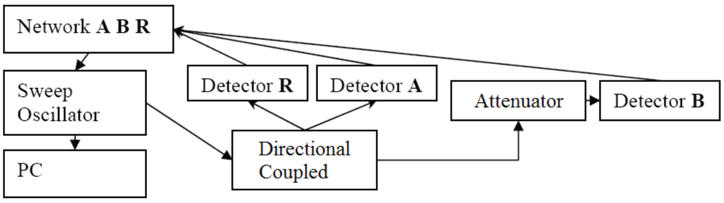

Figure 7.13: Flow-chart of the radiometric chain in the configuration used for its calibration and for the storage of the curve of the attenuator. The arrows indicate the signal path.

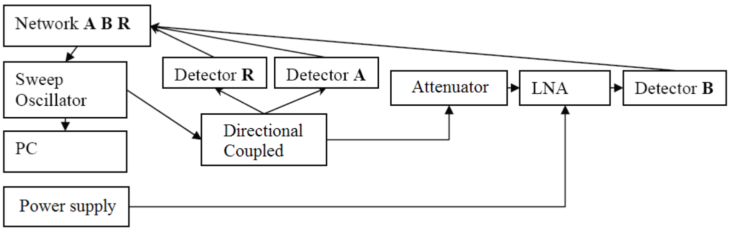

Figure 7.14: Flow-chart of the radiometric chain in the configuration used for the storage of the gain curve of the amplifiers. The arrows indicate the signal path.

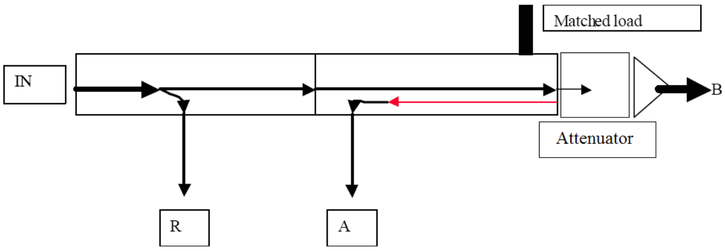

Figure 7.15: Flow-chart of the radiometric chain. The arrows indicate the signal path.

measures the return loss of the DUT, in other words the reflections due to the bad matching between the directional coupled and the DUT. The second directional coupled is a four port whose the fourth port is connected to a matched load. The characteristic curves of the attenuator have been obtained via absolute measures (B (dBm)) and via relative measures to the Reference (B/R (dB)).

7.3.2 Analysis and results

Figures 7.16 ÷ 7.18 show the gain and attenuation curves of the amplifiers when they are used singularly and in pair. For each curve the attenuation value used is -40dB to limit the input power at the first amplifier. Table 7.2

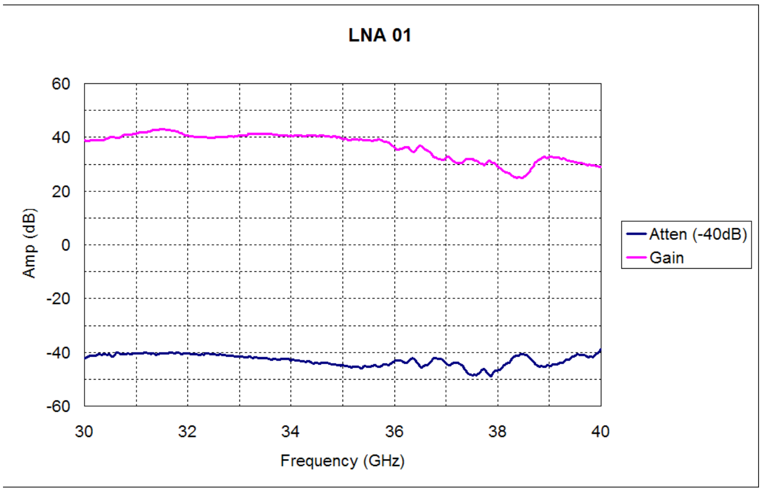

Figure 7.16: Gain and amplitude curves for the first stage LNA.

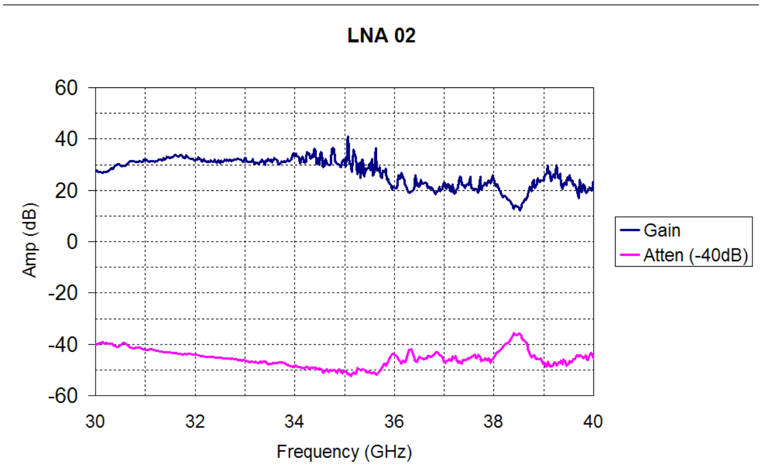

Figure 7.17: Gain and amplitude curves for the second stage LNA.

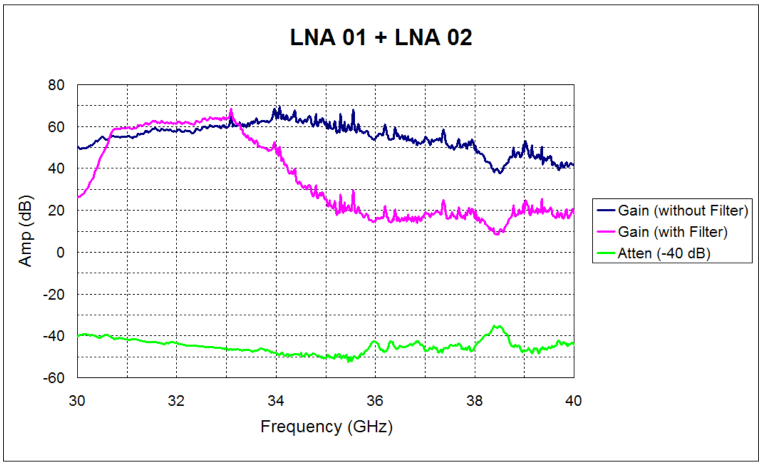

Figure 7.18: Gain and amplitude curves for the LNAs.

shows the Gain values of the *ViKy's* amplifiers.

Amplifier N°	Max Gain (dB)	Min Gain (dB)	Gain average 35±5 GHz (dB)	Gain average 35±2 GHz (dB)	Standard deviation 35±5 GHz (dB)
01	43.0	24.8	36.6	38.7	4.9
02	27.0	28.4	41.0	12.2	5.5
01 + 02 (*)	69.4	37.7	54.8	59.7	19.4
01 + 02 (**)	68.4	8.5	34.6	N.A.	6.7

Table 7.2: LNAs Gain - * With Filter - ** Without Filter.

The B detector has a noise threshold of about -60 dBm. This means that the minimum detectable signal is of the order of -55 dBm to maintain a good precision. By specification the maximum input power for the amplifiers is -45 dBm. In such a situation the attenuation has a dynamic range between $10 \div 15$ dB. For this reasons the attenuation value has been chosen equal to -40 dB. Figure 7.18 shows the gain curve with and without the Filter used to select the functionality range of the amplifiers.

LNA Test Data

All the LNAs properties, as declared from the constructor, are shown in Table 7.3.

The T_{NOISE} at 35 GHz has been calculated observing two different objects at the physical temperature of 300 and 70 degrees respectively. The ratio of voltage signal obtained observing these two different targets is the Y_{FACTOR}. The measured values of Y_{FACTOR} and T_{NOISE} are shown in Table 7.4.

Frequency (GHz)	Gain (dB)	P -1dB (dBm)	Noise Figure (dB)	T_{NOISE}
33.0	74.1	8.5	2.68	251.79
35.0	72.5	9.8	2.75	260.67
37.0	70.3	10.2	3.3	335.69

Table 7.3: LNA properties.

V_{cold}	V_{hot}	T_{cold}	T_{hot}	Y_{FACTOR}	T_{NOISE}
0.893	1.536	70	300	1.720	249.4

Table 7.4: Y_{FACTOR} and T_{NOISE} measurements results.

Comparing the value of T_{NOISE} in Table 7.3 with the same measured value in Table 7.4 it is possible to verify the reliability of the measure and, at the same time, the quality of the LNAs.

7.4 Diode Detector measurements

7.4.1 Detection sensitivity

The sensitive curve of the detector has been determined using an input power of about -20 dBm to be confronted with that declared by the constructor. The values of the sensitivity are known in a frequency range from 26 to 40 GHz with frequency step of 1 GHz. The voltage value have been determined taking the input power constant and varying the frequency. Considering the frequency of 35 GHz, an output power of -20 dBm and a measured voltage of 12.6 mV, the corresponding sensitivity will be:

$$S = V_{(mV)}/P_{out(mW)} = 12.6/0.01 = 1260 mV/mW \, ,$$

where

$$P_{out(mW)} = 10^{P_{out(dBm)}/10} \, .$$

7.4.2 Detection linearity

The detector has been characterized thanks to a variable attenuator and a Power Meter. The output voltage variation has been determined varying the input power. Figure 7.20 shows the output voltage values versus the input power in a bi-logarithmic plot. The blue points of Figure 7.20 represent the measurements results, the red line is the best fit obtained with the first 4

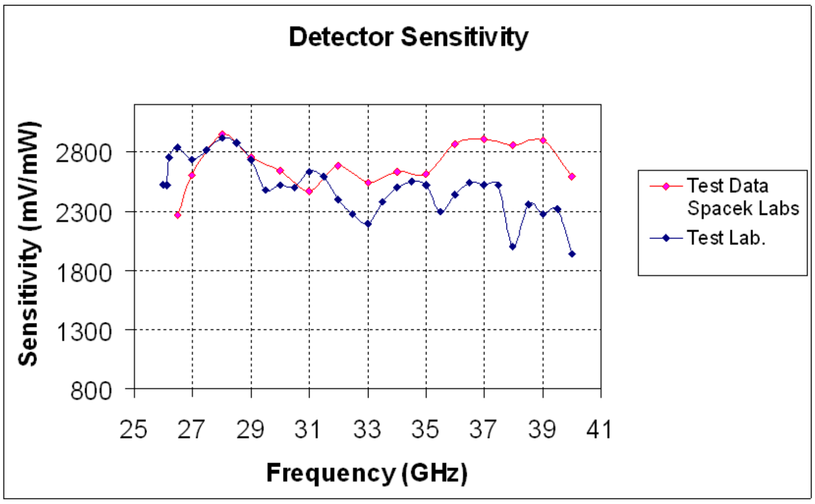

Figure 7.19: Measurements of the curve sensitivity of the diode compared with the Test Data by Spacek Labs.

points (taken starting from bottom-left), the green line is the bisector of the graphic. The diode has a linear behaviour only in the bottom part of the bi-logarithmic graph. If the output voltage were equal to the input power multiplied by a constant (gain) then in logarithmic scale it would be:

$$V_{out} = P_{in} \times G \Longrightarrow \log V = \log P + K \Longrightarrow Y = X + Cost$$

and so the lines Y and X should be parallel. An amplifier maintains a constant gain for low-level input signals. However, at higher input levels, the amplifier goes into saturation and its gain decreases. The 1 dB compression point (P1dB) indicates the power level that causes the gain to drop by 1 dB from its small signal value. The −1 dB point compression has been calculated to be at a voltage of about 10.65 mV corresponding to an attenuation of about −20.8 dBm.

7.5 Radiometric temperature measurements

The aim of the test here mentioned is to document the temperature and voltage profile of the *ViKy* radiometer. The radiometer consists of a first stage of LNA, a filter, a second stage of LNA, an attenuator and a diode detector where the temperatures and voltages are evaluated to study the relation between them. Figure 7.21 shows the inverse proportional relation between the temperature and the voltage measured in the diode detector. If a matched load is *not* temperature controlled then its temperature will achieve

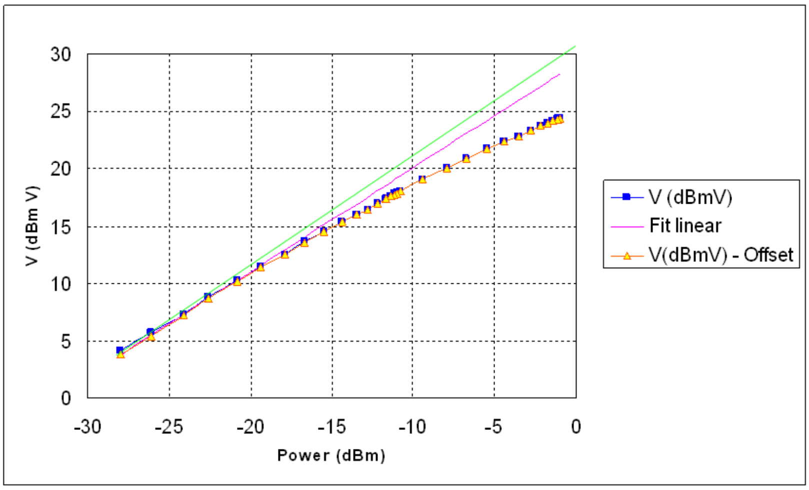

Figure 7.20: Measurements of the linearity shape of the diode.

the stability in a lot of time (around 6 hours). Otherwise, if it *is* temperature controlled its temperature will achieve the stability in a shorter time (around 2 hours). The same conclusions can be taken for the temperature control of the whole radiometer. The ”ciano” and ”orange” shapes show the inverse

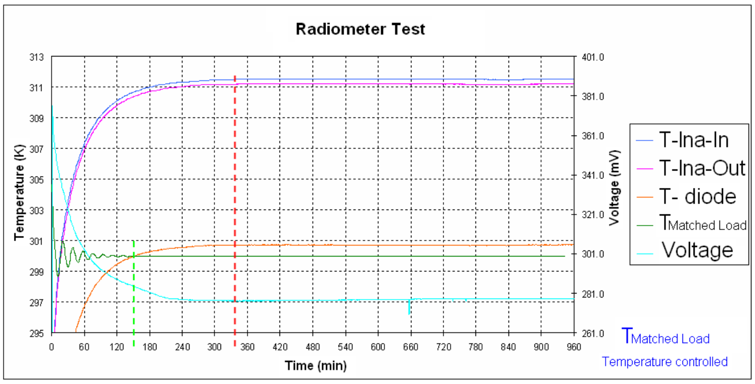

Figure 7.21: Radiometric temperature measurements.

proportionality relation between temperature and voltage. This means that a temperature stability of the radiometer is needed to minimize the errors due to the voltage fluctuations.

7.5.1 Determination of the temperature error

In the hypothesis of observing a matched load at a constant temperature the measure of the voltage will fluctuate by a value ΔV due to the hardware

Attenuation (dB)	$\overline{T}_{Eccosorb}(K) = 299.995 \pm 0.003$		$\overline{T}_{Eccosorb}(K) = 77.606 \pm 0.002$
Observation time (s)	120		120
Diode Temperature (K)	302.462 ± 0.017		299.955 ± 0.011
LNA Temperature (K)			
$\Delta T_{Eccosorb}$ (K)	0.008		0.008
$\overline{V}$ (mV)	267.1 ± 0.1		247.4 ± 0.1
$\Delta V_{Eccosorb}$ (mV)	0.2		0.1
$\Delta T/\Delta V$ (K/mV)		**11.28**	
$\Delta V/\Delta T$ (mV/K)		0.088	

Table 7.5: Radiometer analysis - The temperature is not controlled.

Attenuation (dB)	$\overline{T}_{Eccosorb}(K) = 289.465 \pm 0.005$		$\overline{T}_{Eccosorb}(K) = 79.435 \pm 0.003$
Observation time (s)	120		120
Diode Temperature (K)	304.999 ± 0.003		305.159 ± 0.001
LNA Temperature (K)	307.352 ± 0.004n		307.496 ± 0.005
$\Delta T_{Eccosorb}$ (K)	0.010		0.010
$\overline{V}$ (mV)	421.1 ± 0.0		255.0 ± 0.0
$\Delta V_{Eccosorb}$ (mV)	0.1		0.1
$\Delta T/\Delta V$ (K/mV)		**1.264**	
$\Delta V/\Delta T$ (mV/K)		0.791	

Table 7.6: Radiometer analysis - The temperature is controlled.

instability depending on:

$$\Delta T = \Delta V \cdot \left[Sensibility \left(\frac{\Delta T}{\Delta V} \right) \right] \tag{7.1}$$

	$T_{Eccosorb}$	$\Delta V(mV)$	$\Delta T/\Delta V(K/mV)$	$\Delta T(K)$
Not termo controlled	300.00±0.01	0.40	11.28	**4.52**
Termo controlled	289.6±0.12	1.40	1.26	**1.76**

Table 7.7: Determination of the temperature error at $T \simeq 300K$.

	$T_{Eccosorb}$	$\Delta V(mV)$	$\Delta T/\Delta V(K/mV)$	$\Delta T(K)$
Not termo controlled	81.44±4.66	1.0	11.28	**11.28**
Termo controlled	79.39±0.70	3.70	1.26	**4.66**

Table 7.8: Determination of the temperature error at $T \simeq T_{Nitrogen}$.

Table 7.7 and Table 7.8 show that, controlling the temperature of the radiometric chain, a smaller temperature error is obtainable.

7.6 Conclusions

In this chapter the functionality and qualifying tests have been discussed. The Antenna system has been studied separately in its two principal components: feed hord and reflectarray antenna. The radiometer system has been tested and the properties of low noise amplifier and diode detector have been studied also separately. The necessary time to thermalize the radiometer is about 2 hours using an auto PID (Proportional Integrative Derivative) method.
The signal fluctuations are not a problem because they have a period larger than the observational time.
Y_{FACTOR}, T_{NOISE} (as mentioned in § 6.3.2 and in § 6.3.3) and thermal sensitivity (ΔT) are in agreement with the specifications.

In the next chapter I will summarize the whole PhD thesis showing the image that *ViKy* system is capable to perform.

Chapter 8

Conclusions

The main target of the presented project has been to study the millimeter technology transfer of the ESA Planck Satellite and the presented results represents three years of research performed by myself. The planning of the whole *ViKy* system has been performed by the IASF team led by Prof. Nazzareno Mandolesi. My personal and original contribution concerned:

- the definition of the specific of the entire *ViKy* system,
- the design of the reflectarray antenna as well as the radiometer by using a commercial softwares,
- the electromagnetic measurements (functionality and calibration tests),
- the project of the software interface for the signal digitalization.

A pre-patent investigation, performed by the Spinner consortium within the *WIC* project, highlighted the originality and newness of our project since to date no other passive system, coupled with a reflectarray antenna, has never been proposed. This demonstrates the full potential of the *ViKy* system in term of feasibility and commercial applications.

This chapter describes the main goals that have been achieved during the last three years and new and original way to design a reflectarray antenna. The chapter summarizes the results of the electromagnetic measurements and presentes some picture regarding the different phases of the project.

During my Degree Thesis period I studied one of the components of the LFI Instrument on-board the ESA Planck Satellite that will be lanched next April 2009. One of the possible spin-off based on the technology developed in such an Instrument is to produce a mm-wave imaging camera operating at 35 GHz named *ViKy* - Video camera for Imaging in Ka-band. The choice of this frequency has been made as a trade off among low atmospheric attenuation, antenna dimensions, available technologies, and costs. A new and original way to develop such a system is the use of a reflectarray coupled with a radiometer receiver. The reflectarray antenna is an array of micro planar antennas illuminated by a horn. The advantage of using this kind of systems is given by the possibility to scan the scene electronically, without using complex motion controllers. To demonstrate the capability of the radiometer, used to receive the radiometric signal coming from the target, and to validate the analytical and the software approaches, used to design the reflectarray subsystem, the *ViKy prototype* will use a mechanical beam scanning system.

8.1 The *ViKy* project

As discussed in chapters 2 and 6 the atmospheric absorption changes dramatically from visible wavelengths to microwaves. In addition, weather conditions may affects the attenuation coefficient, depending on wavelength. The main interest in using microwave antennas is to obtain a very good compromise between electrical performance, due to the atmospheric attenuation conditions, and mechanical dimensions of the antenna. The angular resolution (i.e. the HPBW) is proportional to the effective area of the adopted antenna. Thus a very big antenna is needed to have useful angular resolution at low frequency range where the atmospheric attenuation is negligible.

In the Figure 1.1 the atmospheric attenuation from 10 GHz to 1000 GHz is shown. There are two minimum of atmospheric attenuation at 35 and 94 GHz which provide good observational conditions for *ViKy*. At these frequency bands, electromagnetic waves may provide high contrast images in unfavourable weather conditions and may penetrate opaque solids. Millimeter wave detectors, like *ViKy*, can detect metal objects, since they reflect the diffuse radiation from the sky, which is colder than the background emission.

Advantages and potentialities of mm-wave passive imaging are well known. The aim of *ViKy* prototype is to demonstrate the feasibility and the technology of the reflectarray antennas at these frequencies and to assess a low-cost technical solution for passive imaging at millimeter wavelengths.

At frequencies from 20 to 100 GHz there are two different deeps in the attenuation curve. The best frequency channel is centered in the W-band (94*GHz*) due to the best achievable resolution. However, the *ViKy* collaboration decided to build a prototype imaging camera working at 35 GHz for the following reasons:

- the Ka band is a well known frequency band extensively used in satellite applications and in many other commercial applications; active components, as amplifiers or diodes, can be found at lower cost;
- the chosen antenna solution will use technologies already employed with well known mechanical tolerances.

At system level the prototype can be separate in five units:

- the antenna system able to receive the signal coming from the scene;
- the mechanical system that allows the raster scanning of the image;
- the radiometer that amplifies and detects the electromagnetic signal coming from the antenna;
- the data acquisition electronics;
- the software for the image processing and the customer interface.

8.1.1 Antenna System

The *ViKy* antenna system consists of a reflectarray antenna coupled with a feed horn antenna. A detailed antenna design analysis has been discussed in § 2.4 and in chapters 4 and 6; in this section I would like to highlight the work that has been done to achieve a new and original way to design the reflectarray antenna using commercial softwares.

The reflectarray antenna consists in a flat or slightly curved reflecting surface and an illuminating feed, as shown in Picture 8.1. On the reflecting surface, there are many isolated elements named *patches*. The feed horn illuminates these patches which are designed to reflect the incident field and to form a planar wave front in the far-field distance. This operation is similar in concept to the use of a parabolic reflector that reflects the incident field and forms a planar wave front when the horn is placed at its focal point.

To achieve the best optical configuration both the on set and the off set configurations have been studied. As mentioned in § 6.2, the first step consists of the determination of the phase distribution in a hypothetical rectangular grid placed in the planar reflectarray surface, necessary to form

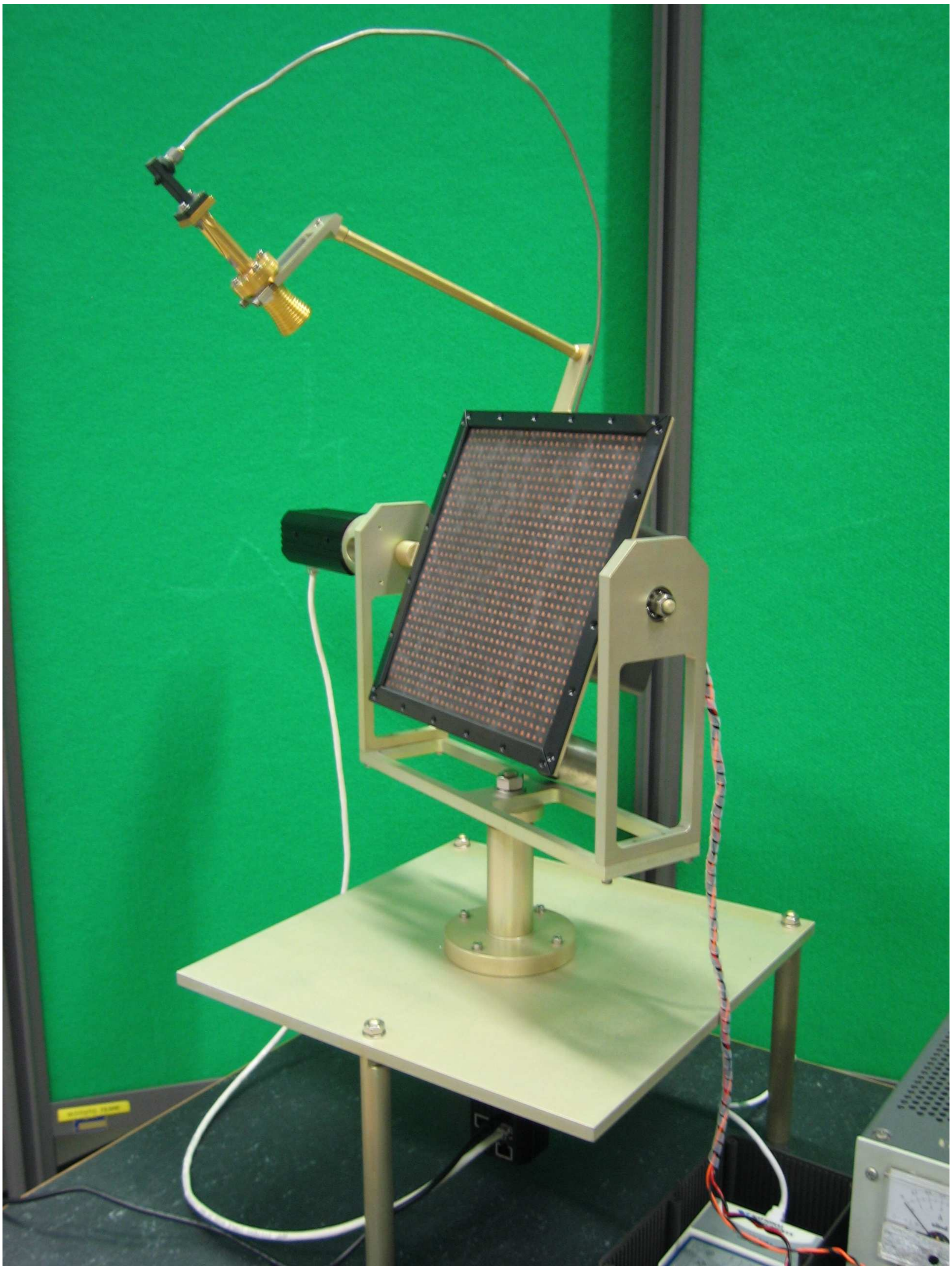

Figure 8.1: *ViKy* antenna system in off set configuration.

a planar wave front. The second step consists of the determination of the characteristic curve that shows the phase contribution as a function of the dimensions of the resonant side of the patches. The phase distribution has been calculated with Grasp9 using a routine that I have implemented (see 6.2.1) whereas the “S” shape curve has been determined by CST-MW using a unit cells approach (see § 3.2.3). Figure 8.2 shows a schematic diagram of the procedure used to dimension each single patch of the whole reflectarray. The picture placed in the left panel shows the phase distribution, over the reflectarray surface, that occurs to re-radiate a planar wave front; the picture in the central panel shows the “S” shape relation between the phase contributions and the dimensions of the resonant side of the patches; the picture in the right panel shows the distribution of the wave incident angle, in a reference system placed in the feed horn position, over the patch. Finally, the picture in the bottom panel shows the distribution of the dimensions of each patch to form the whole reflectarray. In conclusion, before to design a new reflectarray, it is necessary to define:

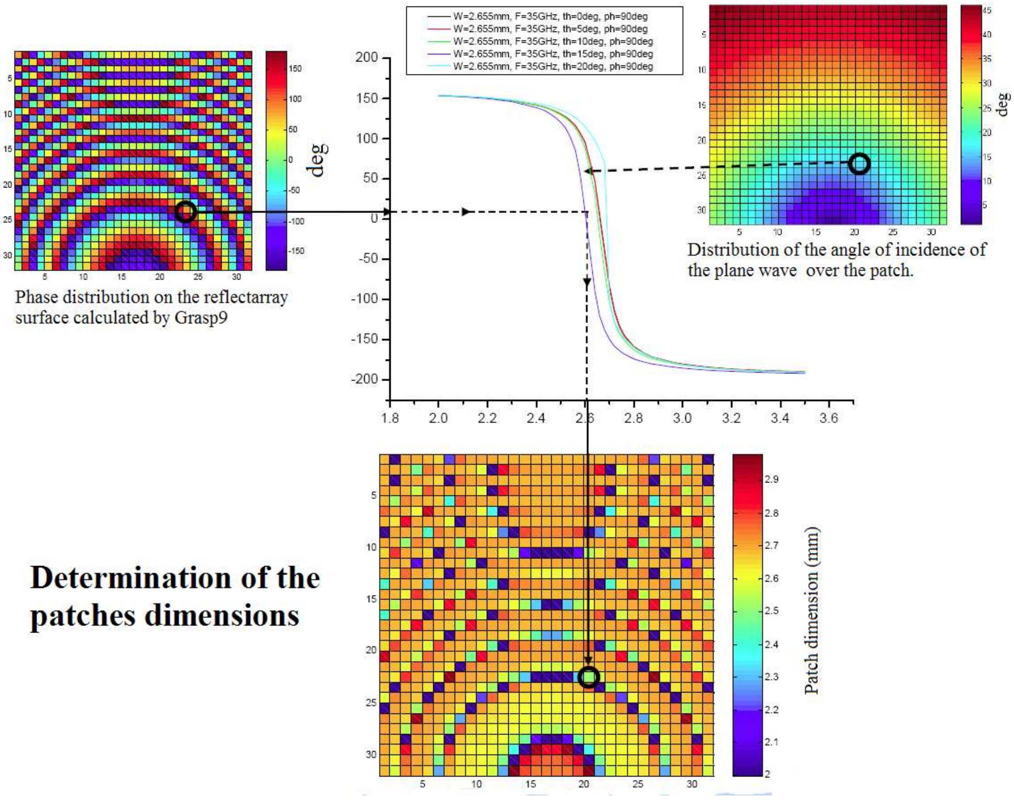

Figure 8.2: Schematic diagram of the patch’s dimensions determination.

- the optical reflectarray properties (HPBW, pattern shape, side lobes level, edge taper, etc.);

- the optical geometry of the antenna system (on set or off set configuration);
- the electrical and geometrical properties of the used materials (ϵ_r, cells dimensions);
- the pattern of the feed horn antenna (HPBW, pattern shape, side lobes level).

8.1.2 Radiometer System

As mentioned in § 6.3 the *ViKy* radiometer has been designed to receive, amplify and detect the signal coming from the antenna system. The radiometer consists of two low noise amplifiers, separated by a filter, and a detector, as shown in Picture 8.3.

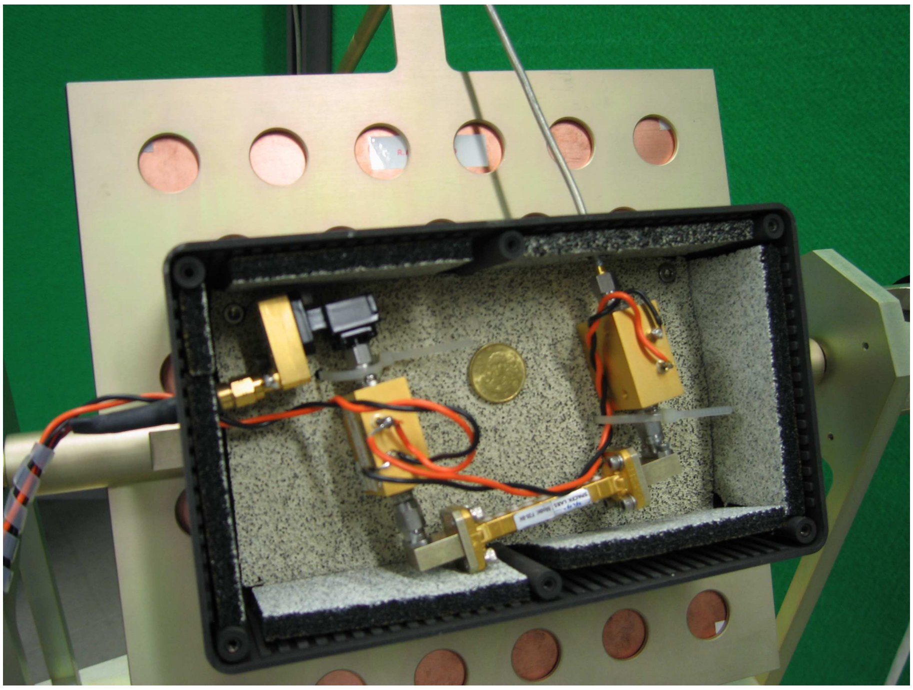

Figure 8.3: *ViKy's* radiometer.

The Low Noise Amplifiers amplify the signal with more than 50 dB of gain in a frequency band from 30 to 38 GHz; the filter reduces this frequency band from 32 to 37 GHz that correspond to the required frequency band (see 2.2).

The detector transforms the power into a voltage and a National Instruments device (see Figure 8.4) allows to analyze the voltage signal in a work station.

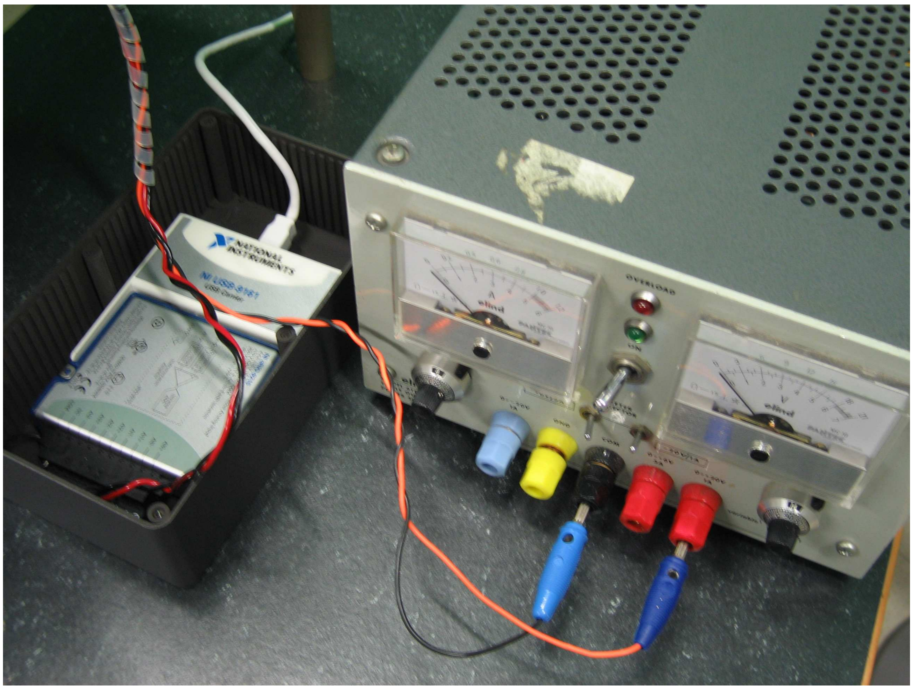

Figure 8.4: National Instrument electronic data acquisition and power supply devices.

8.1.3 Image Post Processing

The image of the scene observed by the *ViKy* system is obtained thanks to an appropriate imaging post processing. For this reason, change detection algorithms are used; they are principally based on *Temporal Frame Difference* or *Background Subtraction*. The first method is used when it is possible to compute the subtraction between two different frames that have been captured in two different instants; the second method is used when a previous background image of the scene has been captured and the camera remains in a static position.

Finally, a specific software, for the customer interface, will make it possible to re-create the observed scene and to distinguish different materials. Figure 8.5 shows, for instance, a customer interface software used in the concealed weapons detection.

Camera Name: Demo
System Status: On
Current Date: 06-02-2006
Current Time: 9:36:37
Case Temperature: 33.34 C
Drift since zero: 0.03 C
Speed: 4 FPS

Alarm Threshold 50.00
Warning Threshold 45.00

Figure 8.5: Example of a customer interface software.

8.2 Applications

The *ViKy* system can be used for real time passive imaging in unfavourable weather conditions (as for instance fog, rain, smoke conditions) and for the detection of concealed weapons. Moreover, mm-waves images can provide an indirect knowledge of physical or chemical properties of the objects that are observed such as composition, water content, temperature and phase change. Mm-waves technologies constitute a very sensitive mean to follow the time variations of such previous features (before), during, (or after) a medical treatment or an industrial process. Mm-waves imaging cameras are passive systems, thus they are safer than X-rays because they are non-ionizing.

Appendix A

Technology transfer projects - 2004 ÷ 2009

In 2004 the SPINNER consortium (see §) was funded with the aim to finance some technology transfer projects. The WIC (W-band Imaging Camera) project was one of them.

A.1 SPINNER-The WIC Project

W-band Imaging Camera was the first project that I have written in 2004. The aim of the project was:

- to design a W-band Imaging Camera;
- to write a Business Plan for a Spin-off activity operating in WIC project;
- to do fund-raising for the Spin-off activity;
- to carry out a market survey;
- to file a patent.

A.2 UIT-Innovation Technology Office

Many other projects have been financed by the Innovation Technology Office (UIT) of the Italian National Institute for Astrophysics. The UIT started its activities in February 2005 as an Office directly under the President of INAF, with the objective of:

- valuing and protecting research results and promoting initiatives for research spin-off;

- promoting innovation and technology transfer activity towards the industry;
- promoting collaborations between research structures and enterprises;
- developing post-doc training also by strong interaction with Universities and Enterprises.

These guidelines have been translated into the following activities:

- enterprise creation: support and advising to spin-off enterprises;
- IPR Management: protection and valuation activities of the research results;
- Communication and Training: creating communication and technology transfer instruments to transfer competences and technologies to the enterprises.

A.2.1 UIT Funded Projects for the IASF team

2005÷2006

UIT Budget for 2005 and that for 2006 have been invested mostly in the financing of technology transfer projects, developed with co-financing enterprises.

UIT call for proposals for 2005 has financed altogether 9 Projects for a total of 190.000,00 Euros. In particular, 6 Projects have concerned the realization of hardware system prototypes and 3 Projects have concerned the feasibility study of spin-off enterprises.

The funded projects for the IASF team are the following:

- engineering development of a video camera in the Ka-band (*ViKy*), activity co-financed by COSPAL;
- feasibility study of a spin-off enterprise to market the *ViKy* project video camera for images in the Ka-band.

These Projects have been concluded successfully in the month of November 2006.

2006÷2007

11 Projects for a total of 220.000,00 Euros have been financed by UIT call for proposals for 2006. The funded Project for the IASF team is the following:

- development of a new planar array concept for satellite applications, co-financed by ”OFFICINE PASQUALI”

2007÷2008

Another project that was financed in collaboration with *Raptech* Spin-off company was:

- Automatic management of public libraries based on RFID technology.

2008÷2009

3 Projects for a total of 101.500,00 Euros have financed by UIT call for proposals for 2008. The funded project for the IASF team is the following:

- GREEN Wireless Sensors Network.

The Project GREEN WSN is based on the ZigBee protocol that uses the 802.15.4 standard as a baseline and adds additional routing and networking functionality. The ZigBee protocol was developed by the ZigBee Alliance. The ZigBee Alliance is a group of companies that worked in cooperation to develop a network protocol that can be used in a variety of commercial and industrial low data rate applications. ZigBee is designed to add mesh networking to the underlying 802.15.4 radio. Mesh networking is used in applications where the range between two points may be beyond the range of the two radios located at those points, but intermediate radios are in place that could forward on any message to and from the desired radios.

A.3 PRISMA

TUIT has been the coordinator of the PRISMA Project (Projects for southern Italy enterprises innovation and development) financed by the Ministry for Economic Development and by INAF. The total funds, including the co-financing from INAF and the private companies participating to the projects, has been approximately 1.700.00,00 Euros which have been invested in 5 different technological transfer Projects to southern Italian enterprises. The five projects have different market area targets, some are very specialized while others are of wider interest, but they have in common technological transfer in strategic fields. These fields are the trade area, the medical area, and atmospheric monitoring for protection. The prototypes produced from the synergies between the structures of INAF and the enterprises of southern Italy have formed the basis for the development of pre-market products entirely realized by the enterprises themselves.

A.3.1 PRISMA Funded Projects for the IASF team

2007÷2008

The PRISMA Project was concluded in March 2007 with the attainment of hardware results of great interest in the following field:

- development of antenna for RFID (Radio Frequency Identifier) systems, in collaboration with *Raptech* Spin-off company.

Radio Frequency IDentification is a data collection technology that uses electronic tags for storing data. The tag, also known as an ″electronic label,″ ″transponder″ or ″code plate,″ is made up of an RFID chip attached to an antenna. Transmitting in the kilohertz, megahertz and gigahertz ranges, tags may be battery-powered or derive their power from the RF waves coming from the reader. Like bar codes, RFID tags identify items. However, unlike bar codes, which must be in close proximity and line of sight to the scanner for reading, RFID tags do not require line of sight and can be embedded within packages. Depending on the type of tag and application, they can be read at a varying range of distances. In addition, RFID antenna can be printed with magnetic ink to reduce cost as compare to that of a bar-code.

A.4 ASTRO SFERA

The future of the PRISMA Project has been the ASTRO-SFERA Proposal including 13 project.

A.4.1 ASTRO SFERA Funded Projects for the IASF team

IASF team project was the following:

ASTRO SFERA 2007

- development of a compact and high performance millimeter wave imaging camera.

A.5 ASI

With the Italian Space Agency (ASI) call for proposals 2007 some projects concerning the Technology Development will be financed. The IASF team participated with the project ViKy realizing two documents concerning both the manager and the economical proposal (see [52, 53].

Bibliography

[1] R. Appleby, R.N. Anderton, S. Price, N.A. Salmon, G.N. Sinclair, J.R. Borrill, P.R. Coward, P. Papakosta, A.H. Lettington, and D.A. Robertson, Compact real-time (video rate) passive millimetre-wave imager, *Proc. SPIE Conf. on Passive Millimeter-Wave Imaging Technology III*, 1999, vol. 3703, pp. 13-19.

[2] I. J. Bahl and P. Bhartia, Microstrip Antennas, Artech House, Dedham, MA, 1980.

[3] M. C. Bailey and M. D. Deshpande, Integral Equation Formulation of Microstrip Antennas, *IEEE Trans. Anten. Propag.*, Vol. AP-30, No. 4, pp. 651656, July 1982.

[4] C. A. Balanis, *Advanced Engineering Electromagnetics*, John Wiley & Sons, New York, 1989.

[5] L. P. Bayvel and A. R. Jones, Electromagnetic Scattering and Its Applications, Applied Science Publishers, London, 1981.

[6] A.O. Barut, Theory of the Scattering Matrix, Macmillan Co., 1967

[7] D. G. Berry, R. G. Malech, and W. A. Kennedy, The reflectarray antenna, *IEEE Trans. Anten. Propag.* AP-11:645651 (Nov. 1963).

[8] P. Bhartia and I.J. Bahl, *Millimeter Wave Engineering and Applications.* New York: Wiley, 1984, pp. 660-671.

[9] M. Bialkowski, A. W. Robinson, and H. J. Song, Design, development, and testing of X-band amplifying reflectarrays, *IEEE Trans. Anten. Propag.* 50:10651076 (Aug. 2002).

[10] L. Boccia et al. Experimental Investigation of a varactor Loaded Reflectarray Antenna, *IEEE MTT-Digest*, 2002

[11] G. Brussaard and P. A. Watson, Atmospheric Modelling and Millimetre Wave Propagation, Chapman & Hall, London, 1995.

[12] K. R. Carver and J. W. Mink, ”Microstrip Antenna Technology,” *IEEE Trans. Antennas Propagat.*, Vol. AP-29, No. 1, pp. 224, January 1981.

[13] D. C. Chang and M. C. Huang, Multiple polarization microstrip reflectarray antenna with high efficiency and low crosspolarization, *IEEE Trans. Anten. Propag.* 43:829834 (Aug. 1995).

[14] M.R. Chaharmir et al. Reflectarray with Variable Slot on Ground Plane, *IEEE Proc.-microw. Antennas propag.*,Vol 150, 2003

[15] R. E. Collin, Foundations for Microwave Engineering, Chapter 6, McGraw-Hill Book Co., New York, 1992.

[16] J. M. Colin, Phased array radars in France: present and future, *Proc. IEEE Symp. Phased Array System and Technology*, Boston, Oct. 1996, pp. 458462.

[17] CST-STUDIO SUITE 2008 - www.cst.com

[18] A. G. Derneryd, A Theoretical Investigation of the Rectangular Microstrip Antenna Element, *IEEE Trans. Antennas Propagat.*, Vol. AP-26, No. 4, pp. 532535, July 1978.

[19] G. A. Deschamps, ”Microstrip Microwave Antennas”, Presented at the Third USAF Symposium on Antennas, 1953.

[20] G.S. Dow, D.C.W. Lo, Y. Guo, E.W. Lin, T.T. Chung, M.D. Biedenbender, O. Miromontes, A. Marashi, L. Yujiri, P.S.C. Lee, M.M. Shoucri, and B.R. Allen, Large scale W-band focal plane array for passive radiometric imaging, in *1996 IEEE MTT-S Int. Symp.* Dig., vol. 1, pp. 369-372.

[21] J. A. Encinar, Design of two-layer printed reflectarray using patches of variable size, *IEEE Trans. Anten. Propag.* 49:14031410 (Oct. 2001).

[22] G. Floquet, *Sur les quations diffrentielles linaires coefficients priodiques*, Ann. cole Norm. Sup. 12, 47-88 (1883).

[23] Y. T. Gao and S. K. Barton, Phase correcting zonal reflector incorporating rings, *IEEE Trans. Anten. Propag.* 43:350355 (April 1995).

[24] E. Girard, R. Moulinet, R. Gillard, and H. Legay, An FDTD optimization of a circularly polarized reflectarray unit cell, *Proc. IEEE AP-S/URSI Symp.*, San Antonio, TX, June 2002, pp. III-136III-139.

[25] www.ticra.com*GRASP9*

[26] E. O. Hammerstad, Equations for Microstrip Circuit Design, *Proc. Fifth European Microwave Conf.*, pp. 268272, September 1975.

[27] C. Han, B. Strassner, K. Chang, and J. Huang, A dual-frequency 7/32 GHz reflectarray antenna, *Progress in Electromagnetics Research Symp.* (PIERS), Honolulu, Oct. 2003 (in press).

[28] R. F. Harrington, *Field Computation by the Moment Methods*. New York: IEEE Press, 1993.

[29] R. F. Harrington, Time-Harmonic Electromagnetic Fields, McGraw-Hill Book Co., p. 183, 1961.

[30] B.I. Hauss, P.J. Moffa, W.G. Steele, H. Agravante, R. Davidheiser, T. Samec, and S.K. Young, Advanced radiometric and interferometric millimeter-wave scene simulations, in *Proc. NATO Workshop on Military Applications of Millimeter Wave Imaging*, Hanscom Air Force Base, MA, 1992.

[31] J. Huang and A. Feria, A 1-m X-band inflatable reflectarray antenna, Microwave Opt. Technol. Lett. 20:9799 (Jan. 1999).

[32] J. Huang, *Analysis of a Microstrip Reflectarray Antenna for Microspacecraft Applications*, JPL TDA Progress Report 42- 120, Feb. 15, 1995.

[33] J. Huang, V. A. Feria, and H. Fang, Improvement of the threemeter Ka-band inflatable reflectarray antenna, *Proc. IEEE AP-S/URSI Symp.*, Boston, July 2001, pp. 122125.

[34] J. Huang, Bandwidth study of microstrip reflectarray and a novel phased reflectarray concept, *Proc. IEEE AP-S/URSI Symp.*, Newport Beach, CA, June 1995, pp. 582585.

[35] J. Huang, Capabilities of printed reflectarray antennas, *Proc. IEEE Symp. Phased Array System and Technology*, Boston, Oct. 1996, pp.131134.

[36] J. Huang and R. J. Pogorzelski, A Ka-band microstrip reflectarray with elements having variable rotation angles, *IEEE Trans. Anten. Propag.* 46:650656 (May 1998).

[37] HFSS11 - www.ansoft.com

[38] J. R. James and P. S. Hall, *Handbook of Microstrip Antennas*, Vols. 1 and 2, Peter Peregrinus, London, UK, 1989.

[39] R. D. Javor et al. Design and Performance of Microstrip reflectarray Antenna, *IEEE Trans. Antennas Propagat.* Vol 43, 1995

[40] F. S. Johansson, A new planar grating-reflector antenna, *IEEE Trans. Anten. Propag.* 38:14911495 (Sept. 1990).

[41] P. B. Katehi and N. G. Alexopoulos, ”On the Modeling of Electromagnetically Coupled Microstrip Antennas-The Printed Strip Dipole,” *IEEE Trans. Antennas Propagat.*, Vol. AP- 32, No. 11, pp. 11791186, November 1984.

[42] A. Kelkar, FLAPS: Conformal phased reflecting surfaces, *Proc. IEEE Natl. Radar Conf.*, Los Angeles, March 1991, pp. 5862.

[43] B. Khayatian and Y. Rahmat-Samii, Characterizing reflectarray antenna radiation performance, *Proc. IEEE AP-S/ URSI Symp.*, Columbus, OH, June 2003 (in press).

[44] D.D. King, *Passive detection* in Radar Handbook, M.I. Skolnik, Ed. New York: McGraw-Hill, 1970, ch. 39, pp. 39-1 to 39-36.

[45] J.D.Kraus, *Radio Astronomy*, McGraw-Hill, 1966.

[46] R.T. Kuroda, G.S. Dow, D. Moriarty, R. Johnson, A. Quil, S.D. Tran, V. Pajo, S. Fornaca, and L. Yujiri, Large scale W-band focal plane array developments for passive millimeter wave imaging, in *Proc. SPIE Conf. on Passive Millimeter-Wave Imaging Technology II*, Orlando, FL, 1998, vol. 3378, pp. 57-62.

[47] Y. T. Lo, D. Solomon, and W. F. Richards, Theory and Experiment on Microstrip Antennas, *IEEE Trans. Antennas Propagat.*, Vol. AP-27, No. 2, pp. 137145, March 1979.

[48] A.C. Ludwig The Definition of Cross Polarization, *IEEE Trans. Antennas and Propagat.*, January 1973.

[49] C. S. Malagisi. Microstrip disc element reflectarray, *Electron. Aerospace Syst.* Conv, 1978

[50] W. Menzel, D. Pilz, and M. Al-Tikriti, Millimeter-wave folded reflector antennas with high gain, low-loss, and low profile, (feature article), *IEEE Anten. Propag. Mag.* 44(3):2429 (June 2002).

[51] R. E. Munson and H. Haddad, *Microstrip Reflectarray for Satellite Communication and RCS Enhancement and Reduction*, US Patent 4,684,952 (Aug. 1987).

[52] N. Mandolesi, L.Stringhetti, J.Zuccarelli, M.Genghini, J.Monari, M.Devetti, *Progetto ViKy - Proposta Tecnico Gestionale*. Risposta al bando ASI "Progetti di sviluppo tecnologico 2007"

[53] N. Mandolesi, L.Stringhetti, J.Zuccarelli, M.Genghini, J.Monari, M.Devetti, *Progetto ViKy - Proposta Economica*. Risposta al bando ASI "Progetti di sviluppo tecnologico 2007"

[54] H. R. Phelan, Spiralphase reflectarray for multitarget radar, *Microwave J.* 20:6773 (July 1977).

[55] D.M. Pozar, Analysis of an infinite phased array of aperture coupled microstrip patches with idealized probe feeds, *IEE Trans. On Antennas Propagation*, Vol. 32, pp.1101-1107, Oct. 1984.

[56] D. M. Pozar and B. Kaufman, "Increasing the Bandwidth of a Microstrip Antenna by Proximity Coupling," Electronic Letters, Vol. 23, pp. 368369, April 1987.

[57] D. M. Pozar and T. A. Metzler, Analysis of a reflectarray antenna using microstrip patches of variable size, *Electron. Lett.* 657658 (April 1993).

[58] D. M. Pozar, S. D. Targonski, and R. Pokuls, A shaped-beam microstrip patch reflectarray, *IEEE Trans. Anten. Propag.* 47:11671173 (July 1999).

[59] D. Pozar, S. D. Targonski, and H. D. Syrigos, Design of millimeter wave microstrip reflectarrays, *IEEE Trans. Anten. Propag.* 45:287296 (Feb. 1997).

[60] D. M. Pozar, "Microstrip Antennas", Proc. IEEE, Vol. 80, No. 1, pp. 7981, January 1992.

[61] Preissner, The influence of the atmosphere on passive radiometric measurements, *Symp. Millimeter Submillimeter Wave Propag. Circuits:* AGARD Conf. Proc., no. 245, pp. 48/1-48/13.

[62] I. E. Rana and N. G. Alexopoulos, Current Distribution and Input Impedance of Printed Dipoles, *IEEE Trans. Antennas and Prop.*, Vol. AP-29, No. 1, pp. 99105, January 1981.

[63] G. M. Rebeiz et al. RF MEMS Phase Shifter : Design and Applications, *IEEE Microwave Magazine*, 2002

[64] W. F. Richards, Microstrip Antennas, Chapter 10 in Antenna Handbook: Theory, Applications and Design (Y. T. Lo and S. W. Lee, eds.), Van Nostrand Reinhold Co., New York, 1988.

[65] W. F. Richards, Y. T. Lo, and D. D. Harrison, An Improved Theory of Microstrip Antennas with Applications, *IEEE Trans. Antennas Propagat.*, Vol. AP-29, No. 1, pp. 3846, January 1981.

[66] C. E. Shannon, "Communication in the presence of noise", Proc. Institute of Radio Engineers, vol. 37, no.1, pp. 10-21, Jan. 1949.

[67] D. H. Schaubert, D. M. Pozar, and A. Adrian, Effect of Microstrip Antenna Substrate Thickness and Permittivity: Comparison of Theories and Experiment, *IEEE Trans. Antennas and Prop.*, Vol. AP-37, No. 6, pp. 677682, June 1989.

[68] D.F. Sievenpiper et. Al., Two dimensional Beam Steering using an electrically tuneable impedance surface, *IEEE Trans. Antennas and Prop.*, Vol. 51, 2003

[69] N. Skou, *Microwave Radiometer Systems: Design and Analysis.* Norwood, MA: Artech House, 1989, pp. 7-19.

[70] W. L. Stutzman and G. A. Thiele, Antenna Theory and Design, Wiley, New York, 1998.

[71] T.N. Ton, B. Allen, H. Wang, G.S. Dow, E. Barnachea, and J. Berenz, AW-band, high gain, low-noise amplifier using PHEMT MMIC, *IEEE Microwave Guided Wave Lett.*, vol. 2, pp. 63-64, Feb. 1992.

[72] A. A. Tolkachev, V. V. Denisenko, A. V. Shishlov, and A. G. Shubov, High-gain antenna system for millimeter-wave radars with combined

electrical and mechanical beam steering, *Proc. IEEE Symp. Phased Array System and Technology*, Boston, Oct. 1996, pp. 266271.

[73] F.T. Ulaby and K.R. Carver, *Passive microwave radiometry,* in Manual of Remote Sensing, R.N. Colwell, Ed. Falls Church, VA: American Society of Photogrammetry, 1983, ch. 11, pp. 475-516.

[74] F. T. Ulaby, R. K. Moore, and A. K. Fung, *Microwave Remote SensingFundamentals and Radiometry*, Addison-Wesley, Reading, MA, 1981.

[75] Volakis, *Antenna Engineering Handbook* Fourth Edition, Chapter 35. McGraw-Hill Educational Europe

[76] L. Yujiri, H. Agravante, M. Biedenbender, G.S. Dow, M. Flannery, S. Fornaca, B. Hauss, R. Johnson, R. Kuroda, K. Jordan, P. Lee, D. Lo, B. Quon, A. Rowe, T. Samec, M. Shoucri, K. Yokoyama, and J. Yun, Passive millimeter-wave camera, in *Proc. SPIE Conf. on Passive Millimeter-Wave Imaging Technology*, Orlando, FL, 1997, 3064, pp. 15-22.

[77] L. Yujiri, M. Shoucri, P. Moffa *Passive Millimeter-Wave Imaging* IEEE Microwave magazine, September 2003, pp.39-50.

[78] L. Yujiri, H. Agravante, S. Fornaca, B. Hauss, R. Johnson, R. Kuroda, B. Quon, A. Rowe, T. Samec, M. Shoucri, K. Yokoyama, Passive millimeter wave video camera, in *Proc. SPIE Conf. on Passive Millimeter-Wave Imaging Technology II*, 1998, vol. 3378, pp. 14-19.

[79] M. Zawadzki and J. Huang, A dual-band reflectarray for Xand Ka-bands, *PIERS Symp.*, Honolulu, Oct. 2003 (in press).

[80] R. E. Zich, M. Mussetta, M. Tovaglieri, P. Pirinoli, and M. Orefice, Genetic optimization of microstrip reflectarrays, *Proc. IEEE AP-S/URSI Symp.*, San Antonio, TX, June 2002, pp. III-128III-131.

Acknowledgements

I would like to start by thanking my supervisor Prof. Nazzareno Mandolesi for giving me the opportunity to work within the Planck and IASF technology transfer teams.

My sincere gratitude goes to Dr. Carlo Burigana, Eng. Enrico Pagana, Dr. Luca Stringhetti, Dr. Luca Valenziano, and Dr. Fabrizio Villa for their unremitting help and guidance concerning the theoretical and technological aspects.

I am very thankful to Dr. Ocleto D'Arcangelo, Eng. Adriano De Rosa, and Eng. Valerio Martorelli for their essential collaboration.

Big thanks to my office-mates Ale, Fabbio, Martino, Pietra, Pietro, Veeto; I really appreciated their sarcasm in front of the coffee machine!

A big thanks also goes to all the IASF team people, in particular to Dr. Francesca Sortino for her collaboration regarding the UIT office questions and to Eng. Enrico Franceschi for his precious assistance whenever I needed an "informatic hand".

Finally, thanks from the deepest of my heart to my wife Serena, my parents and my grandparents, to whom I dedicate this modest work.